DYNAMICS OF ERYTHROCYTES, VESICLES AND CAPSULES IN SHEAR FLOW: THE ROLE OF MEMBRANE BENDING STIFFNESS AND MEMBRANE VISCOSITY

by

ALIREZA ZARIF KHALILI YAZDANI

A dissertation submitted to the

Graduate School—New Brunswick

Rutgers, The State University of New Jersey

In partial fulfillment of the requirements

For the degree of

Doctor of Philosophy

Graduate Program in Mechanical and Aerospace Engineering

Written under the direction of

Professor Prosenjit Bagchi

And approved by

_____

_____

_____

_____

New Brunswick, New Jersey

OCTOBER, 2012

ABSTRACT OF THE DISSERTATION

Dynamics of erythrocytes, vesicles and capsules in shear flow: The role of membrane bending stiffness and membrane viscosity

By

ALIREZA ZARIF KHALILI YAZDANI

Dissertation Director:

Professor Prosenjit Bagchi

Three-dimensional numerical simulations using immersed boundary/front-tracking method are considered to study the dynamics and deformation of microscopic deformable cells with elastic and viscoelastic membranes suspended in linear shear flow. The objective in this thesis is to understand the complex fluid/structure interaction problem for membrane-bound soft matter in dilute suspensions. The numerical model includes all essential properties of the cell membrane, namely, the resistance against shear deformation, area dilatation, and bending, as well as the viscosity difference between the cell interior and suspending fluids. In addition, the Kelvin–Voigt viscoelastic model is incorporated to account for the effect of membrane viscosity. Our

numerical technique is able to simulate complex dynamics of vesicles, capsules, and red blood cells in the tank-treading, breathing, trembling, and tumbling modes.

A detailed comparison of the numerical results for vesicles is made with various theoretical models and experiments. It is found that the applicability of the theoretical models is limited to quasi-spherical vesicles. We show that near the transition between the tank-treading and tumbling dynamics, both the vacillating-breathing-like motion characterized by a smooth ellipsoidal shape, and the trembling-like motion characterized by a highly deformed shape are possible. We also present phase diagrams of the single red blood cell dynamics in linear shear flow. We find that the cell dynamics is often more complex than the well-known tank-treading, tumbling, and swinging motion and is characterized by an extreme variation of the cell shape. Identifying such complex shape dynamics termed here as *breathing* dynamics, is the focus of this study. Further, we find a very good agreement between our numerical and the theoretical and experimental results on the tank-treading frequency of red blood cells, which is often measured in experiments and used to extract the mechanical properties of the cell. A comprehensive analysis of the influence of the membrane viscosity on buckling, deformation and dynamics is given for initially spherical or oblate capsules. The major finding here is that the membrane viscosity leads to buckling in the range of shear rates in which no buckling is observed for capsules with purely elastic membrane.

Acknowledgements

I would like to thank my adviser, Prof. Prosenjit Bagchi for his invaluable guidance, support and encouragement throughout my doctoral study. He has been an excellent mentor, and I significantly benefited from his academic experience and knowledge in this field. I also would like to thank my committee members, Dr. Knight, Dr. Shojaei-Zadeh, and Dr. Young for providing me with valuable suggestions to improve my dissertation.

My sincere thanks and gratitude go to my family for their support at every stage of my life. Without them, my accomplishments would not be possible. To my parents whose thoughts and prayers are always with me, and for the sacrifices they made for me. To my sister who has always wished for me to reach my goals.

Lastly, I would like to thank all my friends and colleagues at Rutgers University, in particular, Murthy, Mona, Tushar, Kellie, Dan, Koohyar and Mengye. Further, I would like to thank Giorgiana, Sohrob and Sankha for keeping me company in room D115A. Our enjoyable group lunch sessions and coffee breaks are memorable. I also would like to specifically thank my dearest friend, Giorgiana who has always been there for me in my hardships, and motivated me to keep on working hard.

This research is funded by NSF Grant No. CBET-0846293. Computational support from the NSF-funded Teragrid resources at TACC and NCSA is acknowledged. I also thank Dr. Fischer for providing his experimental data from his study.

Dedication

To my parents, whose support and sacrifices lie behind my accomplishments.

Table of Contents

List of Tables

List of Figures

Chapter 1

Introduction

1.1 Introduction

Blood is a multiphase fluid comprising of particulate components like erythrocytes (red blood cells), leukocytes (white blood cells), and thrombocytes (platelets) suspended in a liquid called plasma. Red blood cells (RBCs) constitute the major particulate component of blood, which is $40 - 45\%$ by volume *in vivo*. Interactions between different cells and between cells and vessel walls can significantly affect the local hydrodynamics and overall blood rheology in microvessels.

Red blood cells do not contain a nucleus; they are filled with a liquid called hemoglobin, which facilitates the transportation of oxygen to the tissues. Both plasma and hemoglobin solution are considered as incompressible Newtonian fluids. Freely suspended RBCs take the form of a biconcave disk, about 8 μm in diameter and 2 μm in thickness. Their membrane consists of a lipid bilayer supported from the inside by the cytoskeleton, which is primarily composed of a two-dimensional network of spectrin dimers and actin filaments [1,2,4,97] (see Fig. 1.1). Cytoskeleton is essential to the structural integrity of the RBC, and its resistance against shear deformation. Another important property of the membrane is that it strongly resists changes in surface area owing to the presence of lipid bilayer. The lipid molecules in the lipid bilayer can slide past each other, but strongly resist being pulled apart. Thus, the

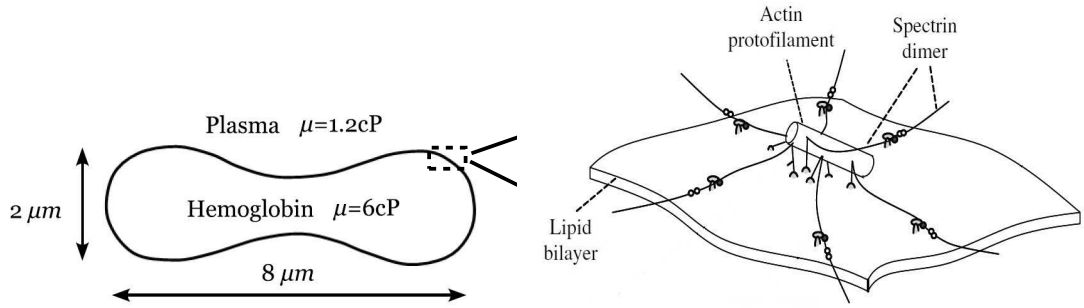

Figure 1.1: Schematic of biconcave resting shape of a red blood cell. The basic molecular structure of the membrane is also depicted [97].

membrane behaves like a two-dimensional incompressible fluid. The cell membrane also exhibits a flexural stiffness, i.e., bending resistance due to the lipid bilayer [4,13]. In addition, the membrane is known to be viscoelastic, and shows viscous resistance to transient in-plain shear deformations [89, 90, 92]. Physically, the viscous effect arises from the fluid-like behavior of the lipid bilayer, whereas the elastic part arises from the stretching of the cytoskeleton. This structure gives the cell extreme flexibility, and ability to easily deform and squeeze through capillaries with diameters less than 8 μm. The cell deformation often plays the primary role in the dynamics and rheology of blood flow in small vessels [4]. As discussed above, on the molecular level, the red blood cell structure is very complex. On the continuum level, however, the detailed molecular structure is neglected and the erythrocyte is modeled as a capsule or vesicle defined as a viscous drop enclosed by a viscoelastic membrane. Unlike a capsule, a vesicle lacks shear resistance; rather it exhibits resistance to bending, and area dilatation.

Blood flow in microvessels at normal volume fraction of red blood cells is rather

complex due to cell-cell interactions, nonuniform shear fields and wall effects. Therefore, to bypass these complexities, a large number of experimental and theoretical studies have been conducted to address dilute suspensions of the cells in an unbounded simple shear flow. In the following, we present a summary of different dynamics and motions of a single red blood cell, capsule and vesicle in simple shear flow.

1.2 Dynamics of Erythrocytes in Simple Shear Flow, and the Theory of Shape-preserving Cells

Studies spanning over several decades have demonstrated that single erythrocytes freely suspended in a linear shear flow undergo primarily two types of motions [5, 9, 10, 12]: (i) a tank-treading (TT) motion characterized by a continuous rotation of the membrane and the interior fluid while the cell maintains a nearly constant angular inclination with the flow direction, and (ii) a tumbling (TU) or flipping motion resembling a rigid body-like behavior. The tank-treading motion is typically observed at high shear rates and low internal to external fluid viscosity ratio, and the tumbling motion is observed otherwise. Similar dynamics has been observed for other soft-matter particulates, e.g., capsules [14, 41, 42] and vesicles [6, 16, 17, 20, 22, 28, 50], which are membrane-bound liquid drops, and structurally similar to erythrocytes.

In addition to the TT and TU motions, a swinging motion of the erythrocytes has been discovered recently [12]. The swinging motion is characterized by an angular oscillation of the cell major axis about a mean orientation, and a simultaneous membrane tank-tread.

The TT-TU transition in dilute suspension was theoretically predicted by Keller & Skalak [7] (hereafter referred to as the KS theory) for *non-deformable* ellipsoids

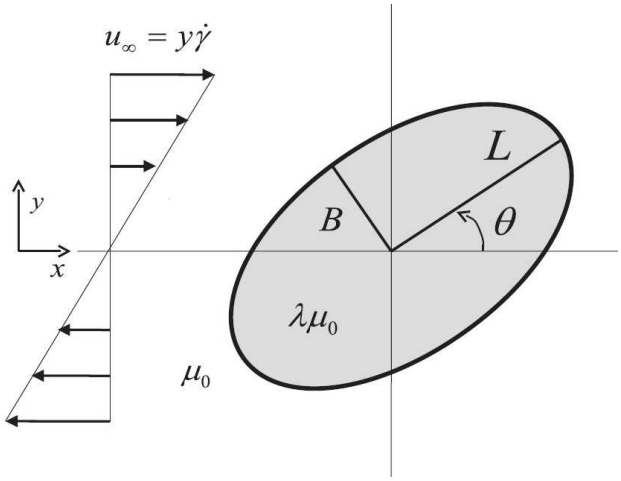

Figure 1.2: Schematic of an ellipsoidal cell in linear shear flow.

of a viscous fluid enclosed by an area-preserving membrane. Figure 1.2 presents the schematic of an ellipsoidal cell with semi-major and -minor axes lengths L and B, respectively, suspended in a linear shear flow $\mathbf{u} = \{\dot{\gamma}y, 0, 0\}$, where $\dot{\gamma}$ is the shear rate. The fluids interior and exterior to the cell are assumed to be incompressible Newtonian liquids with viscosities $\lambda\mu_o$ and μ_o, respectively.

Under equilibrium conditions, the net hydrodynamic moment acting on the cell must be zero. Hence, the analysis showed that the inclination angle θ is governed by the following differential equation

$$\frac{d\theta}{dt} = -\left[\frac{1}{2}\dot{\gamma} + \frac{2LB}{L^2+B^2}\nu\right] + \frac{1}{2}\dot{\gamma}\frac{L^2-B^2}{L^2+B^2}\cos 2\theta\,, \tag{1.1}$$

where ν is the instantaneous membrane tank-treading frequency. Assuming that the membrane shear viscosity μ_s is zero, and thus, the work done by the imposed flow is entirely dissipated inside the cell, the tank-treading frequency was obtained as

$$\nu = -\frac{\dot{\gamma}f_3}{f_2 - \lambda f_1}\cos 2\theta, \tag{1.2}$$

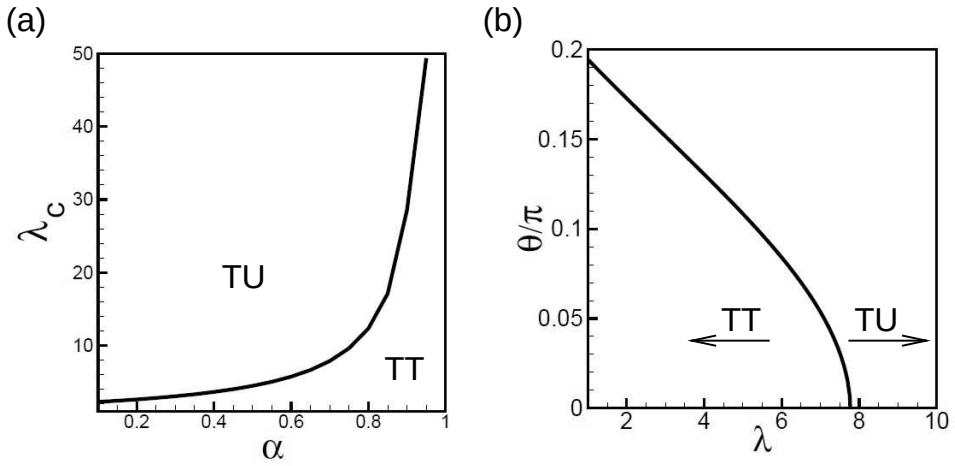

Figure 1.3: Results from the Keller & Skalak [7] model for a nondeformable ellipsoidal cell in simple shear flow are plotted. (a) The critical viscosity ratio λ_c against the aspect ratio α, and (b) the inclination angle θ against λ for a tank-treading ellipsoid with aspect ratio $\alpha = 0.7$.

where f_1, f_2 and f_3 are dimensionless functions of the three major axes of the ellipsoid.

For a prescribed shape of the ellipsoids (usually defined by the aspect ratio $\alpha = L/B$), a steady solution of the system representing a stationary tank-treading motion (i.e. θ = constant) is obtained when the ratio λ is less than a critical value λ_c, and the tumbling motion is predicted for $\lambda > \lambda_c$ as shown in Fig. 1.3(a). Note that λ_c is obtained from the intercept of the curve with $\theta = 0$ in Fig. 1.3(b).

As mentioned before, experiments by Abkarian *et al.* [12] conducted on a red blood cell revealed swinging dynamics accompanied by membrane tank-treading motion. They showed that for high to intermediate shear values, the RBC's inclination oscillated about a mean angle. In other words no steady-state tank-treading motion was observed. With further decrease in the shear rate, the RBC begins to tumble. This observation is a departure from the KS theory. The swinging dynamics and the shear rate-dependent transition were addressed theoretically by [11] within the framework of the KS theory by introducing an *ad hoc* model of the membrane

elasticity.

Despite their apparent success, the above theories neglect the large deformation of the RBC. It is well known that red blood cells can undergo large deformation and attain complex shapes under flowing conditions [4, 5]. Despite a wealth of study on RBC dynamics, the role of the complex shape deformation on the TT-TU transition remains poorly understood. Furthermore, there are significant uncertainties in the measurements of the material properties of the RBC membrane. Their values can significantly change under disease conditions such as sickle cell anemia, diabetes mellitus, and malignant malaria as well as cell aging, and ways of cell handling *in vitro*. Thus, we find it useful to conduct simulations over a wider range of parameters so as to present a complete study of RBC dynamics in shear flow, and a comprehensive phase diagram.

1.3 Dynamics of Vesicles

Vesicles which are viscous liquid drops enclosed by membranes of lipid bi-layers, are often considered as the model particles for the human red blood cells. The bi-layer membrane has two unique characteristics: it behaves as a two dimensional incompressible fluid, and exhibits a bending resistance. Because of the interior fluid, and the liquid nature of the membrane, vesicles are highly deformable. Vesicles are also present in other eukaryotic cells where they form by membrane budding and pinching and act as the intracellular transport vehicles. Synthetic vesicles (liposomes) can be used as drug carriers for targeted delivery. Because of their biological and engineering applications, the dynamics of vesicles in flow has received a significant attention in recent years.

If deformation is neglected, following the KS theory, the vesicle dynamics is controlled by two parameters: the vesicle shape represented by the excess area $\Delta = A/a_o^2 - 4\pi$, and the viscosity ratio λ, where A is the vesicle surface area, and a_o is the radius of a sphere having the same volume as the vesicle. When deformation is considered, a third controlling parameter, namely, the capillary number, or the dimensionless shear rate, $\chi = \mu_o \dot{\gamma} a_o^3 / E_b$, also arises, where E_b is the membrane bending modulus.

Vesicle deformation can occur in TU as well as TT motion. The role of deformation, however, becomes most important in trembling [6, 28, 50], vacillating-breathing [21, 22, 48], and swinging [46] motions, which are new types of unsteady motion that have been observed recently. In such motions, the inclination angle oscillates about the flow direction while the vesicle may undergo a periodic shape deformation as shown by the experimental observations of Zabusky *et al.* [28] in Fig. 1.4. While differences exist between the trembling, vacillating-breathing and swinging modes, particularly because they were observed or predicted by different tools, experimental, numerical or analytical, one common feature is that they occur in the vicinity of the transition between the TT and TU modes. Hereafter, we refer to these new modes as the transition (TR) mode. Phase diagrams in χ–λ plane, which depend on Δ, can be used to describe the transition from one mode to the other. For small values of χ, the transition occurs directly from TT to TU with increasing λ. For $\chi \gtrsim 1$, the transition occurs as TT to TR to TU with increasing λ. Complex and highly convoluted shapes of trembling vesicles, in the form of membrane budding and pinching, have been observed in experiments [6, 16, 17].

Because of the role of deformation, a fully resolved numerical approach is deemed

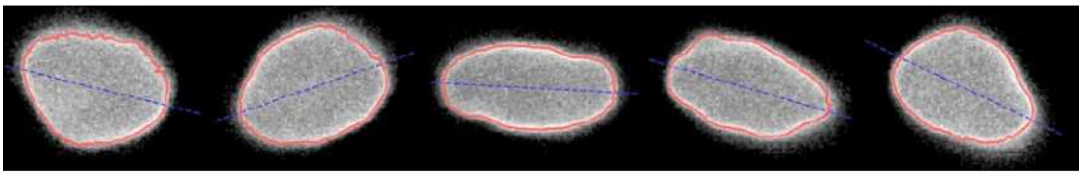

Figure 1.4: Snapshots of a vesicle executing trembling dynamics [28]. Dashed line is the major axis of the elliptical fit to the contour. Note the significant shape variations as the cell inclination oscillates.

necessary in the analysis of vesicle dynamics. Several numerical methods have been developed till date: the boundary integral methods of Kraus *et al.* [43] and Biben, Farutin & Misbah [24], the phase field approach of Biben, Kassner & Misbah [51], 2D simulations of Ghigliotti, Biben & Misbah [71], simulations using multi-particle collision dynamics by Noguchi & Gompper [45,46], and Meßlinger *et al.* [30], spectral boundary integral simulations of Zhao & Shaqfeh [29], boundary integral method of Veerapaneni *et al.* [31,32], to name a few.

1.4 Dynamics of Capsules and Membrane Buckling

Synthetic capsules are used widely in many applications such as cosmetics, drug delivery and cell encapsulation. One of the most prominent examples of biological capsules is the red blood cells, which account for nearly 44-45% of the human blood by volume. As a result, dynamics and deformation of capsules in a flow has been a subject of intense research. Early experimental study by Chang & Olbricht [54] observed the tank-treading dynamics of synthetic capsules in simple shear flow. Walter *et al.* [72,73] studied the shear induced deformation of artificial capsules, and extracted their mechanical properties from rheoscopic measurements. Theoretical studies on capsule dynamics have been carried out by modeling the membrane as a two-dimensional

interface. Asymptotic theories in the limit of small deformation were developed for initially spherical capsules by Barthès-Biesel [53] and Barthès-Biesel & Rallison [18]. More recently, Vlahovska *et al.* [74] performed an asymptotic analysis of initially nonspherical capsules with area-incompressible elastic membrane, and studied the effect of capsule deformability on the tank-treading to tumbling transition.

A great number of numerical analyses has been conducted in recent years to study large deformation of capsules; for example, the boundary integral simulations of Pozrikidis [55], Ramanujan & Pozrikidis [40], Pozrikidis [56], Lac *et al.* [59], Walter *et al.* [75] and Foessel *et al.* [81]; immersed-boundary/front-tracking simulations of Eggleton & Popel [60], Li & Sarkar [80], Sui *et al.* [41] and Le [79], accelerated boundary integral simulation of Pranay *et al.* [78], spectral boundary integral simulations by Kessler *et al.* [42], Zhao *et al.* [77], and Wang & Dimitrakopoulos [76], to name a few. Of particular interest is the work by Lac *et al.* [59] who observed that the capsule buckled at low shear rates with wrinkles forming near the equator similar to the experimental observation of Walter *et al.* [73] as shown in Fig. 1.5. The membrane instabilities and short-wavelength wrinkles were also predicted in the asymptotic work by Finken & Seifert [82]. Li & Sarkar [80] and Sui *et al.* [47] also observed capsule buckling in their front-tracking simulation. Recently, Foessel *et al.* [81] studied the influence of the internal to external fluid viscosity ratio on buckling. Evidence of buckling was also reported by Walter *et al.* [75] for ellipsoidal capsules in simple shear flow.

Bagchi & Kalluri [14] have addressed the capsules large deformation and dynamics using three-dimensional front-tracking simulations. Simulations over a broad range of viscosity contrast λ, dimensionless shear rate or capillary number Ca, and aspect

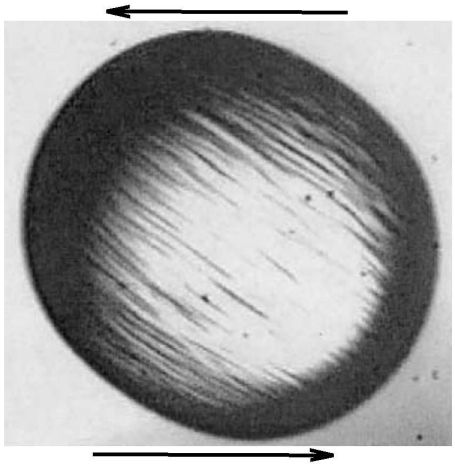

Figure 1.5: Buckling of an initially spherical capsule with a polysiloxane membrane in simple shear flow (Walter *et al.* [73]).

ratio α have identified three distinct modes of capsule dynamics: (i) swinging or oscillatory mode at low viscosity contrast (ii) transitional mode from swinging to tumbling motion at moderate viscosity contrast, where θ periodically becomes positive and negative, but a full tumbling does not occur. Here the capsule attains spherical shape momentarily as it enters the compressive quadrant. and (iii) pure tumbling mode at higher viscosity contrast. Similar modes of dynamics were also observed by the numerical studies of Kessler *et al.* [42] and Walter *et al.* [75]. Note that for capsules and RBCs, the capillary number is defined as $Ca = \mu_o \dot{\gamma} a_o / E_s$, where E_s is the membrane modulus of elasticity.

1.5 Effect of Membrane Viscosity

The aforementioned theoretical and numerical studies assumed that the capsule membrane is elastic, and hence, did not consider the viscosity of the membrane. Evidence of the membrane viscosity in red blood cells has been illustrated in numerous experimental studies, e.g., Puig-de-Morales-Marinkovic *et al.* [92], Tran-Son-Tay *et al.* [8],

and Evans & Hochmuth [88]. It was argued that the viscous dissipation in the membrane could be in the same order of magnitude of the dissipation in the internal fluid [8, 91]. The membrane viscosity effect on artificial capsules was also studied experimentally by Chang & Olbricht [54] and Walter *et al.* [72]. Barthès-Biesel & Sgaier [52] developed the small-deformation theory for capsules with a viscoelastic membrane that followed the Kelvin–Voigt model, and found that the membrane viscosity set an upper bound for deformation. Further, they predicted an undamped oscillatory motion of the capsule in the limit of large membrane viscosity. Numerical analysis of large deformation of capsules with a viscoelastic membrane is relatively scarce. The only known work is the one by Diaz *et al.* [58] who used the boundary integral simulation to study the transient response of a capsule with the Kelvin–Voigt viscoelastic membrane in an elongational flow. Also notable is the particle-based method used by Noguchi & Gompper [44, 45] for vesicles, who observed that the membrane viscosity had a significant effect on the dynamics, shape transition and orientation of vesicles.

1.6 Scope of the Thesis

Based on the discussion in the previous sections, understanding the dynamics and shape deformations of erythrocytes in flow is fundamental to understanding the complex dynamics and rheology of blood *in vivo* and *in vitro*. The objective of this thesis is to study the dynamics of red blood cells and vesicles as the membrane-bound soft matters. Further, a comprehensive analysis on the influence of membrane viscosity on capsule dynamics in a shear flow is lacking, and is the objective of the present study. The specific topics that have been addressed during the course of this thesis

are described below:

1. **Numerical methodology (Chapter 2):** We have developed an accurate three-dimensional model for the red blood cell membrane within the framework of immersed boundary front-tracking method. The finite-element numerical methodology for treating the membrane as well as the inclusion of membrane bending resistance in the model, which is crucial to address the true physics of vesicle and RBC dynamics, will be discussed in detail. Furthermore, we present a numerical method for capsules with a viscoelastic membrane that follows the Kelvin–Voigt model. In addition to the membrane shear viscosity and elastic modulus, the model includes the membrane bending resistance, surface area dilatation, and internal to external fluid viscosity contrast.

2. **Analysis of vesicle shape and dynamics in linear shear flow (Chapter 3):** Dynamics of a single vesicle in simple shear flow has been studied significantly both experimentally and theoretically. These studies have posed new and interesting questions to be addressed. Apart from the considerable progress in theoretical analysis, the limitations in the applicability of the models to non-quasi spherical vesicles make the numerical approaches deem necessary. Therefore, three-dimensional numerical simulations are carried out for individual vesicles suspended in shear flow over a wide range of controlling parameters. The focus here is to elucidate the parametric dependence and the self-similarity of the vesicle dynamics, quantification of vesicle deformation, and the analysis of shape dynamics. A detailed comparison of the numerical results is also made with various theoretical models and experiments.

3. **Red blood cell dynamics in linear shear flow and analysis of TT frequency (Chapter 4):** While the vacillating-breathing and trembling dynamics of

the vesicles has been a subject of intense research in recent days, similar dynamics of the erythrocytes has not been reported. These studies motivate us to investigate whether similar complex dynamics may exist for the red blood cells despite some differences in the membrane structure and properties between an RBC and a vesicle. We present phase diagrams of the single red blood cell dynamics in dilute suspension using three-dimensional numerical simulations. The computational geometry replicates an in vitro linear shear flow apparatus. By considering a wide range of shear rates and interior-to-exterior fluid viscosity ratio, it is shown that the cell dynamics is often more complex than the well-known tank-treading, tumbling and swinging motion, and is characterized by an extreme variation of the cell shape. Identifying such complex shape dynamics termed here as *breathing* dynamics, is the focus of this study.

4. **Effect of membrane viscosity on capsule dynamics in linear shear flow (Chapter 5):** We address a sequence of problems related to capsule deformation, dynamics, and buckling. We observe that the membrane viscosity leads to buckling in the range of shear rates in which no buckling is observed for purely elastic membrane. In order to obtain stable shapes, it is necessary to introduce the bending stiffness. Using the stable shapes, we analyze the influence of the membrane viscosity on deformation, inclination, and tank-treading frequency of initially spherical capsules. We then consider the influence of membrane viscosity on the unsteady dynamics of an initially oblate capsule, and show that the dynamics changes from swinging to tumbling with increasing membrane viscosity.

Chapter 2

Numerical Methodology

2.1 Problem Description and the Numerical Method

2.1.1 Problem setup

We consider a three-dimensional computational domain bounded by two infinite flat plates placed parallel to the x-axis in a Cartesian coordinate system. Here, x is the direction of the flow, y is the direction of velocity gradient and z is the direction of vorticity of the undisturbed flow. The channel is assumed to be infinitely long in the x and z directions. We use periodic boundary conditions in these directions to reduce the size of the computational domain to a cube of side H as shown in Fig. 2.1. This also allows us to use Fourier transforms to accelerate the computation. Further, the no-slip boundary condition is imposed on the walls. In the absence of any cells, we have linear shear flow at zero pressure-gradient driven by the two walls of the channel as

$$\mathbf{u}^{\infty} = \{\dot{\gamma} y,\, 0,\, 0\}\ , \tag{2.1}$$

where $\dot{\gamma}$ is the shear rate.

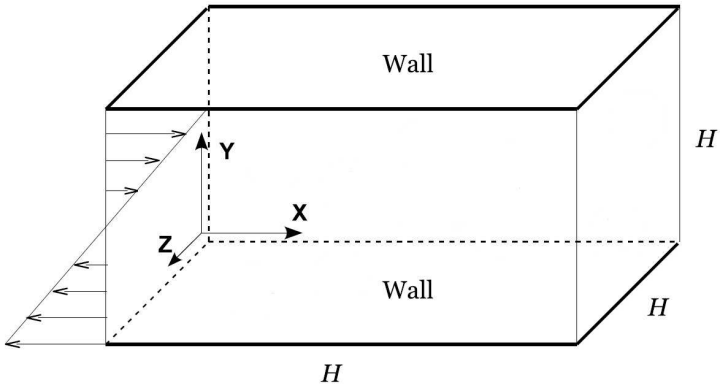

Figure 2.1: Schematic of the computational domain.

2.1.2 Fluid-structure interaction

The numerical method considered here is the front-tracking/immersed boundary method [65–67] to study the deformation of suspended cells enclosing a liquid, which may have different properties from the suspending liquid. The main idea of the front-tracking method is to use a single set of equations for both the fluids, inside and outside a cell. The fluid equations are solved on a fixed Eulerian grid, and the interface is tracked in a Lagrangian manner by a set of marker points. The fluids inside and outside the cell are considered to be incompressible. Therefore, the fluid motion is governed by the continuity and Navier-Stokes equations as

$$\nabla \cdot \mathbf{u} = 0\,, \tag{2.2}$$

$$\rho\left[\frac{\partial \mathbf{u}}{\partial t} + \mathbf{u}\cdot\nabla\mathbf{u}\right] = -\nabla p + \nabla\cdot\mu(\nabla\mathbf{u} + (\nabla\mathbf{u})^T)\,, \tag{2.3}$$

where $\mathbf{u}\,(\mathbf{x},t)$ is the fluid velocity, ρ is the density, p is the pressure, and μ is the fluid viscosity. Here, $\mu\,(\mathbf{x},t)$ is a single variable used to denote the viscosity of the

entire fluid. Therefore, $\mu = \mu_i$ inside the cell and $\mu = \mu_o$ outside. Mathematically, we define μ using an indicator function $I(\mathbf{x})$, which is unity inside the cell and zero outside. Thus, μ is given by a single expression for every point in the fluid as

$$\mu(\mathbf{x}) = \mu_o + (\mu_i - \mu_o) I(\mathbf{x}) \,. \tag{2.4}$$

As the cell moves and deforms, μ needs to be updated. This is done by solving a Poisson equation for the indicator function $I(\mathbf{x}, t)$ as

$$\nabla^2 I = \nabla \cdot \mathbf{G} \,, \tag{2.5}$$

$$\mathbf{G} = \int_S \delta(\mathbf{x} - \mathbf{x}') \mathbf{n} d\mathbf{x} \,, \tag{2.6}$$

where δ is the three-dimensional Dirac-Delta function, $\mathbf{x}'$ is a location on the cell surface, $\mathbf{x}$ is a location in the flow, and $\mathbf{n}$ is the unit vector that is normal to the cell surface and directing outward.

The membrane force density $\mathbf{f}$ arises due to membrane deformation, and is evaluated using a finite-element method. The finite-element treatment of the cell interface will be discussed in detail in Section (2.2). Having $\mathbf{f}$ evaluated, the membrane and the fluid are coupled in a two-way manner by adding a source term $\mathbf{B}$ to the r.h.s of (2.3). The source term $\mathbf{B}$ is related to $\mathbf{f}$ as

$$\mathbf{B}(\mathbf{x}, t) = \int_S \mathbf{f}(\mathbf{x}', t) \delta(\mathbf{x} - \mathbf{x}') d\mathbf{x}' \,. \tag{2.7}$$

Further, the δ-function is constructed by multiplying three 1D δ-functions as

$$\delta(\mathbf{x}-\mathbf{x}') = \delta(x-x')\delta(y-y')\delta(z-z')\,. \tag{2.8}$$

For numerical implementation, however, a smooth representation of δ-function is used as

$$\begin{aligned} D(\mathbf{x}-\mathbf{x}') &= \frac{1}{64\,h^3}\prod_{i=1}^{3}\Big(1+\cos\frac{\pi}{2h}(x_i-x_i')\Big) \quad \text{for} \quad |x_i-x_i'|\le 2h\,, \quad i=1,2,3\,, \\ D(\mathbf{x}-\mathbf{x}') &= 0 \qquad \text{otherwise}\,, \end{aligned} \tag{2.9}$$

where h is the Eulerian grid size (Unverdi & Tryggvason [66]). As a result, the membrane force varies smoothly over four Eulerian grid points surrounding the interface. In discrete form, the integral in (2.7) can be written as

$$\mathbf{B}(\mathbf{x}_j) = \sum_i D(\mathbf{x}_j-\mathbf{x}_i')\mathbf{f}(\mathbf{x}_i')\,, \tag{2.10}$$

where i and j represent Lagrangian and Eulerian points, respectively.

2.1.3 Flow solver

The domain is discretized using a fixed (Eulerian) rectangular and uniform grid. A combined second-order finite-difference scheme and Fourier transform is used for the spatial discretization, and a second-order time-split scheme is used for the temporal discretization of Navier-Stokes equations. In this method, the momentum equation is split into an advection–diffusion equation and a Poisson equation for the pressure.

The body-force term is retained in the advection–diffusion equation. The nonlinear terms are treated explicitly using a second-order Adams-Bashforth scheme, and the viscous terms are treated semi-implicitly using the second-order Crank-Nicholson scheme. The resulting linear equations are inverted using an ADI (alternating direction implicit) scheme to yield a predicted velocity field. The Poisson equation is then solved to obtain pressure at the next time level. Using the new pressure, the velocity field is corrected so that it satisfies the divergence-free condition. Details of the method can be found in [61, 62, 70].

2.1.4 Interface tracking

The cell interface is tracked in a Lagrangian manner. After solving Navier-Stokes equations for the pressure and velocity fields, the no-slip condition on the cell surface is imposed by extracting the surface velocity from the surrounding fluid at each time step as

$$\mathbf{u}_S(\mathbf{x}', t) = \int_S \mathbf{u}(\mathbf{x}, t)\delta(\mathbf{x} - \mathbf{x}')d\mathbf{x}\,. \tag{2.11}$$

Though the summation is over all the Eulerian grid points, only the local points contribute to the membrane velocity. The discrete form of the delta function used here is the same given by (2.9). The Lagrangian points on the membrane are then advected as

$$\frac{d\mathbf{x}'}{dt} = \mathbf{u}_S(\mathbf{x}', t)\,. \tag{2.12}$$

Numerically, the above equation is treated explicitly using the second-order Adams-Bashforth scheme.

2.2 Finite-element Treatment of an Elastic Membrane

Membrane deformation is treated using a finite element model developed by Charrier *et al.* [68]; Shrivastava & Tang [69], and later implemented by Eggleton & Popel [60] within the framework of immersed boundary method to consider cells large deformation. First, the membrane is discretized using flat triangular elements. The main idea is that a general 3D deformation of the membrane can be reduced to a 2D problem by assuming that each triangular element on the membrane remains flat even after deformation. Then, the forces acting on the three vertices of that element are obtained by computing the displacements of the vertices of the deformed element with respect to the undeformed element. We first describe the model for a purely elastic membrane followed by a detailed discussion on the modeling of a viscoelastic membrane.

2.2.1 Red blood cell model

The biconcave shape of a red blood cell is prescribed as

$$x = R\eta\,; \qquad y = \frac{R}{2}\sqrt{1-r^2}(C_0 + C_2 r^2 + C_4 r^4)\,; \qquad z = R\zeta\,, \tag{2.13}$$

where $\eta^2 + \zeta^2 = r^2$, and R is adjusted to control the cell volume [3]. The surface area and the volume of the red blood cell are taken to be $134.1\mu\text{m}^2$ and $94.1\mu\text{m}^3$, respectively [3]. The initial shape is stress-free. The coefficients C_0, C_2, and C_4 depend on the osmolarity, and are taken to be 0.207, 2.003, and -1.123, respectively [3].

As discussed before, a complete elastic model for red blood cells must include all essential properties of the cell membrane, namely, the resistance against shear deformation, area dilatation, and bending. The first two types of deformation are

modeled using the strain energy function developed by Skalak *et al.* [64] for a red blood cell membrane as

$$W_e = \frac{E_s}{4}\left[\left(\frac{1}{2}I_1^2 + I_1 - I_2\right) + \frac{C}{2}I_2^2\right], \tag{2.14}$$

with I_1 and I_2 defined as

$$I_1 = \epsilon_1^2 + \epsilon_2^2 - 2\,; \quad I_2 = \epsilon_1^2\epsilon_2^2 - 1\,, \tag{2.15}$$

where ϵ_1 and ϵ_2 are the principal stretch ratios, E_s is the surface Young's modulus, and CE_s is the modulus associated with the surface area dilatation. The Skalak law behaves linearly in the small-deformation domain, with $E_s = 2G_s(2 + C)/(1 + C)$, where G_s is the surface shear modulus [59]. The area dilatation may be restricted by a large value of C as in case of a red blood cell for which the surface is nearly area-incompressible. Further, I_1 and I_2 are the strain invariants of the Green strain tensor, which is written as

$$\mathbf{E} = \frac{1}{2}\left(\mathbf{F}^T \cdot \mathbf{F} - \mathbf{I}\right), \tag{2.16}$$

where $\mathbf{F} = \partial\mathbf{x}/\partial\mathbf{X}$ is the deformation gradient of the current configuration $\mathbf{x}$ relative to the original configuration $\mathbf{X}$, and $\mathbf{I}$ is the identity tensor. Note that the squared of principal stretch ratios ϵ_1^2 and ϵ_2^2 are the eigenvalues of the left Cauchy-Green deformation tensor defined as $\mathbf{D} = \mathbf{F} \cdot \mathbf{F}^T$. Hence, we can write

$$\epsilon_i^2 = \frac{1}{2}\left[D_{11} + D_{22} \pm \sqrt{\left\{(D_{11} - D_{22})^2 + 4D_{12}^2\right\}}\right], \quad i = 1, 2\,. \tag{2.17}$$

The corresponding in-plane elastic force in each element is obtained by applying the principle of virtual work as $\mathbf{f}_e^m = -\partial W_e/\partial \mathbf{v}$, where $\mathbf{v}$ is the displacement of a Lagrangian point on the cell surface (see [69, 70] for details). Then, the force $\mathbf{f}_e$ at each vertex is found as the resultant of $\mathbf{f}_e^m$ on the triangles surrounding the vertex.

The bending resistance is modeled following Helfrich's [33] formulation for bending energy

$$W_b = \frac{E_b}{2} \int_S (2\kappa - c_o)^2 \, \mathrm{d}S + E_g \int_S \kappa_g \mathrm{d}S \,, \tag{2.18}$$

where E_b is the bending modulus associated with the mean curvature κ, E_g is the bending modulus associated with the Gaussian curvature κ_g, and c_o is the spontaneous curvature. According to the Gauss–Bonnet theorem of differential geometry the second integral in (2.18) remains invariant for topologically equivalent shapes, and hence, can be dropped from the equation. It should be mentioned that the resistance against area dilatation also gives rise to a local in-plane tension σ, and an associated energy $\int_S \sigma \mathrm{d}S$. Thus, the total energy of the membrane minus the elastic energy becomes

$$\frac{E_b}{2} \int_S (2\kappa - c_o)^2 \, \mathrm{d}S + \int_S \sigma \mathrm{d}S \,. \tag{2.19}$$

The surface force density can be derived by calculating the first variation of (2.19). Then, the expression will involve both κ and κ_g, but not E_g, and becomes

$$\mathbf{f}_n = E_b \left[(2\kappa + c_o) \left(2\kappa^2 - 2\kappa_g - c_o \kappa \right) + 2 \, \Delta_{LB} \, \kappa \right] \mathbf{n} - 2\sigma\kappa \, \mathbf{n} \,, \tag{2.20}$$

$$\mathbf{f}_t = \nabla_s \sigma \,, \tag{2.21}$$

where $\nabla_s = \mathbf{I}_s \cdot \nabla$ is the surface gradient operator, $\Delta_{LB} = \nabla_s \cdot \nabla_s$ is the Laplace–Beltrami operator, and $\mathbf{I}_s = \mathbf{I} - \mathbf{n} \otimes \mathbf{n}$ is the surface projection matrix [34]. Here $\mathbf{f}_n$ is the normal force, and $\mathbf{f}_t$ is the in-plane force arising due to the constraint of area dilatation. It should also be mentioned that based on our conventions a sphere will have a positive mean curvature. We note that the two different expressions for energy associated to the area dilatation, i.e., $\int_S \sigma \mathrm{d}S$ and the second term in (2.14) $CE_sI_2^2/8$, are not specifically related to each other. The latter was derived by Skalak *et al.* for red blood cell membrane, which behaves as a nearly incompressible surface. In the present study, the in-plane force $\mathbf{f}_t$ due to the constraint of area dilatation is evaluated as a part of the elastic force $\mathbf{f}_e$ obtained using the strain energy function (2.14). This is more convenient to be implemented in the context of the front-tracking method as the Lagrange multiplier σ is not needed. Finally, the body force $\mathbf{B}$ acting on the fluid can be evaluated as

$$\mathbf{B} = \int_S (\mathbf{f}_n + \mathbf{f}_e)\ \delta(\mathbf{x} - \mathbf{x}')\mathrm{d}\mathbf{x}' \,. \tag{2.22}$$

We now describe the numerical technique to compute the normal force $\mathbf{f}_n$. The cell surface is discretized using small flat triangular elements as shown in Fig. 2.2(a) for a sample prolate vesicle. Each vertex is surrounded by five or six elements. The curvatures κ and κ_g on the triangulated surface is calculated by a quadratic surface fitting,

$$z' = ax'^2 + bx'y' + cy'^2 + dx' + ey' \,, \tag{2.23}$$

where (x', y', z') is a local coordinate system with origin at a Lagrangian point of interest, and the coordinate z' is aligned with the estimated normal vector. The technique of computing the curvatures and their derivatives is described in detail by Garimella & Swartz [35] and Petitjean [36]. One-ring neighbor points are used to find the coefficients using a least-square method, and iterations are performed to obtain an accurate fitting until a satisfactory convergence for the estimated normal vector is reached. The curvatures, κ and κ_g, are expressed in terms of the fitted coefficients as

$$\kappa = -\frac{a + c + ae^2 + cd^2 - bde}{\left(1 + d^2 + e^2\right)^{3/2}}\,, \tag{2.24}$$

and,

$$\kappa_g = \frac{4ac - b^2}{\left(1 + d^2 + e^2\right)^2}\,. \tag{2.25}$$

To discretize the Laplace–Beltrami operator, we work in the framework of computational image reconstruction [37, 38]. For a Lagrangian node $\mathbf{x}'_i$, the Laplace–Beltrami operator is written as

$$\Delta_{LB}\,\kappa_i = \frac{1}{2\mathcal{A}} \sum_{j \in N_1(i)} \tilde{\mathbf{n}}_j \cdot \left(\nabla_s \kappa_j + \nabla_s \kappa_{j+}\right) \left\|\mathbf{x}'_j - \mathbf{x}'_{j+}\right\|\,, \tag{2.26}$$

where $N_1(i)$ represents the set of vertices in the first ring neighborhood of i (see Fig. 2.2(b)), $\tilde{\mathbf{n}}_j$ is the unit outward normal to the edge $[j, j+]$, and $\mathcal{A}$ is the area of all triangles sharing the node i. Further, the gradient $\nabla_s \kappa_i$ at a node i is approximated

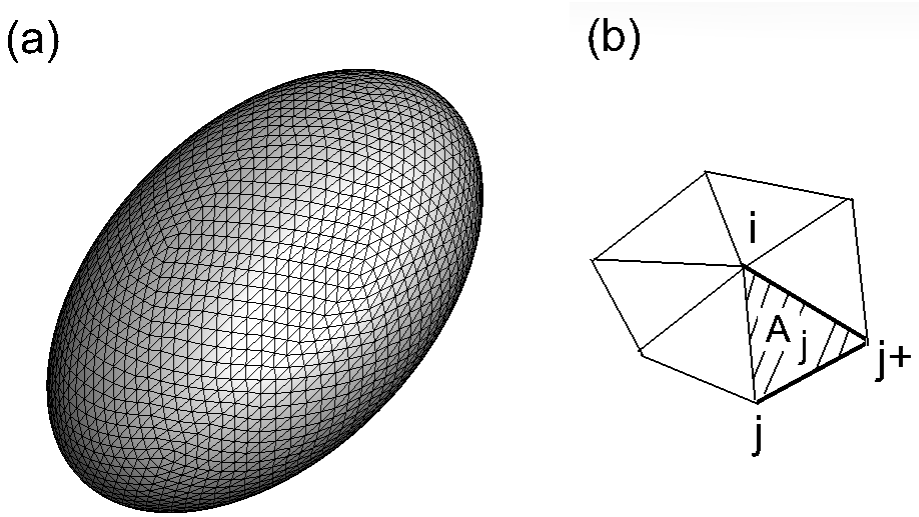

Figure 2.2: (a) Discretization of the vesicle surface; (b) schematic for the first-ring neighbors of the vertex i.

by a weighted average of the gradients on the adjacent triangles as

$$\nabla_s \kappa_i = \frac{1}{\mathcal{A}} \sum_{j \in N_1(i)} A_j \nabla_{T_j} \kappa \,, \tag{2.27}$$

where $\nabla_{T_j}\kappa$ is the surface gradient approximation of the mean curvature on each adjacent triangle $T_j = [i, j, j+]$, and A_j is the area of T_j. Assuming that κ varies linearly in each triangle, $\nabla_{T_j}\kappa$ can be written as

$$\begin{aligned} \nabla_{T_j}\kappa \;=\; & \frac{1}{4A_j^2}\Big\{ \kappa_i \left[(\mathbf{x}'_i - \mathbf{x}'_j)\cdot(\mathbf{x}'_j - \mathbf{x}'_{j+})(\mathbf{x}'_{j+} - \mathbf{x}'_i) + (\mathbf{x}'_i - \mathbf{x}'_{j+})\cdot(\mathbf{x}'_{j+} - \mathbf{x}'_j)(\mathbf{x}'_j - \mathbf{x}'_i) \right] \\ & + \text{similar terms with } i \text{ and } j \text{ interchanged} \\ & + \text{similar terms with } i \text{ and } j_+ \text{ interchanged} \Big\} . \end{aligned} \tag{2.28}$$

2.2.2 Vesicle model

The vesicle initial shape is taken to be a prolate spheroid with the axis of symmetry in the shear plane. The vesicle is represented as a liquid drop surrounded by a zero-thickness membrane. The membrane is assumed to possess the resistance against bending and area dilatation only. Similar to the model for red blood cell membrane, the normal force $\mathbf{f}_n$ is evaluated using (2.20), whereas the in-plane force due to area dilatation $\mathbf{f}_t$ is computed from the second term of Skalak strain energy function in (2.14) by applying the principle of virtual work as

$$W_a = \frac{CE_s}{8}\left(\epsilon_1^2\epsilon_2^2 - 1\right)^2 , \tag{2.29}$$

$$\mathbf{f}_t = -\frac{\partial W_a}{\partial \mathbf{v}} . \tag{2.30}$$

The body force $\mathbf{B}$ acting on the fluid will then be evaluated as

$$\mathbf{B} = \int_S (\mathbf{f}_n + \mathbf{f}_t)\ \delta(\mathbf{x} - \mathbf{x}')\mathrm{d}\mathbf{x}' . \tag{2.31}$$

Volume preservation

Due to the area constraint, a nearly spherical vesicle may deform by losing its volume. Such volume loss is observed in our simulations for lower values of excess area Δ only, typically < 0.5. In such cases, we find that the tank-treading inclination angle is rather sensitive to a small change in volume. The volume loss is prevented by adding

a uniform force to (2.31)

$$\mathbf{f}_v = -K_v \frac{\Delta V}{V_0} \mathbf{n}\,, \tag{2.32}$$

where V_0 is the initial volume, $\Delta V = (V - V_0)$ is the change, and K_v is a sufficiently large positive number [36].

2.3 Finite-strain Viscoelastic Model

The numerical modeling of the membrane shear resistance, area dilatation, and bending resistance has been described in detail in the previous section. In the following, we focus on the numerical implementation of membrane viscosity.

In order to model the viscoelastic effect of the membrane we use the Kelvin–Voigt stress-strain relation in which the membrane stress is the sum of the elastic and viscous contributions [52, 58]. The elastic contribution is modeled by using the Skalak strain energy function in (2.14). The principal elastic stresses (or tensions) for large deformation of an infinitesimal membrane patch can be derived by the following equations

$$\tau_1^e \equiv \frac{1}{\epsilon_2}\frac{\partial W_e}{\partial \epsilon_1}\,; \quad \tau_2^e \equiv \frac{1}{\epsilon_1}\frac{\partial W_e}{\partial \epsilon_2}\,. \tag{2.33}$$

For an isotropic membrane, the principal stresses are along the same direction as the principal stretches. Hence, the stress tensor can be written in terms of the principal stresses and directions as

$$\boldsymbol{\tau}^e = \tau_1^e\, \mathbf{e_1} \otimes \mathbf{e_1} + \tau_2^e\, \mathbf{e_2} \otimes \mathbf{e_2}\,, \tag{2.34}$$

where $\mathbf{e_1}$ and $\mathbf{e_2}$ are the unit eigenvectors of the left Cauchy-Green deformation tensor $\mathbf{D} = \mathbf{F} \cdot \mathbf{F}^T$. Using (2.15) & (2.33), the stress tensor (2.34) can be equivalently written as [4]

$$\boldsymbol{\tau}^e = \frac{2}{\epsilon_1 \epsilon_2} \frac{\partial W_e}{\partial I_1} \mathbf{F} \cdot \mathbf{F}^T + 2\epsilon_1 \epsilon_2 \frac{\partial W_e}{\partial I_2} \left(\mathbf{e_1} \otimes \mathbf{e_1} + \mathbf{e_2} \otimes \mathbf{e_2} \right) . \tag{2.35}$$

It should be mentioned that the first term in the above equation contributes to the deviatoric part of the stress tensor, whereas the second term is called the volumetric stress tensor.

The membrane viscous effects can be modeled by considering a viscous constitutive equation, which involves the rate of strains and describes the material behavior as a *Newtonian* liquid:

$$\tau_1^v \equiv 2\mu_s \frac{1}{\epsilon_1} \frac{D\epsilon_1}{Dt} ; \quad \tau_2^v \equiv 2\mu_s \frac{1}{\epsilon_2} \frac{D\epsilon_2}{Dt} , \tag{2.36}$$

where μ_s is the membrane shear viscosity (N.s/m), and D/Dt is the material derivative w.r.t time. The elastic behavior is modeled by a spring with the stiffness E_s, whereas the viscous effect is modeled by a dashpot with the coefficient μ_s. Therefore, the Kelvin–Voigt model assumes that the spring and dashpot are in parallel, and the total stress is simply the sum of the elastic and viscous stresses. From (2.33) & (2.36), the total stress along the principal directions can be found as

$$\tau_i = \tau_i^e + \tau_i^v \qquad (i = 1, 2) . \tag{2.37}$$

Note that in (2.36), the deviatoric part of the strain rate tensor is only contributing

to the viscous stresses. It means that the viscous dissipation due to the rate of area dilatation is neglected in our study. This term can be included in our model by introducing a coefficient of membrane dilatational viscosity. While the importance of this term is not quite known for capsules, it was shown that its contribution to the dissipation is essentially negligible for the membranes with vanishing area dilatation [8]. In addition, the membrane response is likely to be more complicated than the linear Kelvin–Voigt model. The membrane viscosity is reported to behave as that of a non-Newtonian fluid (specifically, a power-law fluid as suggested by Puig-de-Morales-Marinkovic *et al.* [92]). The Kelvin–Voigt model, however, has the advantage of being simple and introducing a single constant parameter μ_s.

Through our numerical analysis, we observed that a direct numerical implementation of (2.37) leads to numerical instability due to the time-derivatives of strains. Therefore, to avoid this problem, we incorporate a more conventional approach of finite element analysis for viscoelastic materials, where a time-convolution integral is used to relate the viscous stresses to the strain history. Here, we consider another elastic term with the stiffness E_1 in series with the viscous term to form a *Maxwell* element. This Maxwell element is then used in parallel with the membrane elastic modulus E_s. The mechanical analog of this model is presented in Fig. 2.3. In small-strain viscoelasticity, the stress is evaluated in terms of the strain history by introducing a time-dependent shear relaxation modulus $G(t)$, which in turn, can be expressed in terms of a Prony series as follows:

$$G(t) = G_\infty + \sum_{i=1}^{N} G_i \exp(-t/\alpha_i)\,, \tag{2.38}$$

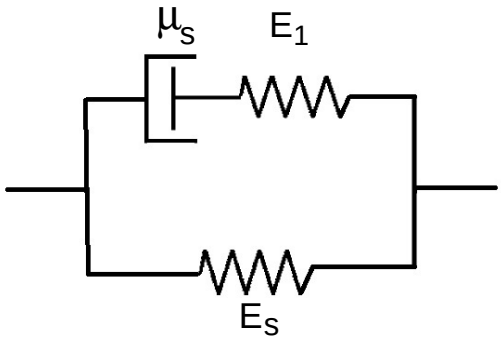

Figure 2.3: Schematic of the mechanical system considered in the present numerical analysis to model the membrane viscoelasticity.

where N is the number of Maxwell elements, G_∞ is the long-term relaxation modulus, and $\alpha_i = \mu_i/E_i$ are the relaxation time constants corresponding to each Maxwell element. As a generalization to the finite-strain viscoelasticity, which is the case here, we can write a Prony series expansion for the mechanical system in Fig. 2.3 by considering $N = 1$, $G_\infty \equiv E_s$, and $G_1 \equiv E_1$. Note that as $E_1 \to \infty$, $G(t)$ becomes equal to E_s, and the mechanical system in Fig. 2.3 essentially represents the Kelvin–Voigt model. Thus, taking a large value for E_1 will guarantee the correct implementation of the Kelvin–Voigt model. More details on the values of E_1 will be presented in the subsequent section. Below is a brief discussion on the integral formulation of the viscoelastic stress. More information on the derivation and numerical implementation of finite-strain viscoelasticity can be found in Holzapfel [84] and Abaqus/Standard Theory Manual [85].

We define the instantaneous shear modulus $G_0 \equiv G(t = 0) = E_s + E_1$ using the Prony series introduced in (2.38). The instantaneous viscoelastic response of the material can be decomposed into the deviatoric and volumetric instantaneous stresses

such that $\boldsymbol{\tau}_0(t) = \boldsymbol{\tau}_0^{dev}(t) + \boldsymbol{\tau}_0^{vol}(t)$, with $\boldsymbol{\tau}_0^{dev}(t)$ defined as

$$\boldsymbol{\tau}_0^{dev}(t) = \frac{2}{\epsilon_1 \epsilon_2} \frac{\partial W_e}{\partial I_1} \mathbf{F} \cdot \mathbf{F}^T \,, \tag{2.39}$$

where the membrane elastic modulus E_s in W_e is replaced by the instantaneous shear modulus G_0. The volumetric stress is assumed to be purely elastic as the viscous dissipation due to rate of area dilatation is neglected. Therefore, we have

$$\boldsymbol{\tau}_0^{vol}(t) \equiv \boldsymbol{\tau}^{vol}(t) = 2\epsilon_1 \epsilon_2 \frac{\partial W_e}{\partial I_2} \left(\mathbf{e_1} \otimes \mathbf{e_1} + \mathbf{e_2} \otimes \mathbf{e_2} \right) \,, \tag{2.40}$$

where the membrane area dilatation modulus CE_s remains unchanged in the energy function W_e. The basic integral formulation of the stress for linear isotropic viscoelasticity is written as [83]

$$\boldsymbol{\sigma}(t) = \boldsymbol{\sigma}_0(t) + \int_0^t \frac{\dot{G}(s)}{G_0} \boldsymbol{\sigma}_0(t-s) \mathrm{d}s \,, \tag{2.41}$$

where $\boldsymbol{\sigma}$ is the total small-strain viscoelastic stress. Therefore, the total finite-strain viscoelastic stress $\boldsymbol{\tau}$ can be written as a generalization of the above equation as [85]

$$\boldsymbol{\tau}(t) = \boldsymbol{\tau}_0^{dev}(t) + \text{ SYM} \left[\int_0^t \frac{\dot{G}(s)}{G_0} \mathbf{F}_t^{-1}(t-s) \cdot \boldsymbol{\tau}_0^{dev}(t-s) \cdot \mathbf{F}_t(t-s) \, \mathrm{d}s \right] + \boldsymbol{\tau}^{vol}(t) \,, \tag{2.42}$$

where $\mathbf{F}_t(t-s) = \partial \mathbf{x}(t-s) / \partial \mathbf{x}(t)$ is the deformation gradient of the configuration at time $(t-s)$ relative to the configuration at time t. A transformation is performed on the stress relating the state at time $(t-s)$ to the state at time t, and SYM[.] ensures the symmetry of the transformed stress tensor.

The cell surface is discretized using flat triangular elements. The deformation gradient tensor $\mathbf{F}$, stretch ratios ϵ_1 and ϵ_2, and hence, the stress tensor $\boldsymbol{\tau}$ are then evaluated for each triangular element with linear shape functions [69, 70]. The stress is stored at each element and is integrated forward in time. We assume that the stress is known at time $t - \Delta t$, and we need to evaluate the convolution integral in (2.42) for the stress at time t, where Δt is the numerical integration time step. Having the stress tensor in (2.42) evaluated, we use the principle of virtual work to estimate the corresponding viscoelastic force in the membrane for each element as

$$\mathbf{f}_{ve} = \sum_m \int_{S_m} \frac{\partial \mathbf{N}}{\partial \mathbf{X}} \cdot \mathbf{P} \, \mathrm{d}S_0 \,, \tag{2.43}$$

where $\mathbf{f}_{ve}$ is the global nodal vector of external force acting on the fluid, $\mathbf{N}$ is the vector of linear shape functions commonly used for a triangular element [83], $\mathbf{P}$ is the first Piola–Kirchhoff stress tensor, and $\mathrm{d}S_0$ is the element surface area in the unstressed original configuration. Note that the integration is performed over the area S_m of the original configuration $\mathbf{X}$ for an arbitrary element m. Hence, the stress tensor $\boldsymbol{\tau}$ that is the Cauchy stress in the deformed configuration needs to be transformed to the stress $\mathbf{P}$ in the original configuration by the following equation

$$\mathbf{P}^T = \epsilon_1 \epsilon_2 \, \mathbf{F}^{-1} \cdot \boldsymbol{\tau} \,. \tag{2.44}$$

2.4 Dimensionless Parameters

There are a number of relevant time scales involved in the dynamics of a viscoelastic capsule suspended in linear shear flow. The shear flow time scale causing deformation

is $\tau_f \sim \lambda\dot{\gamma}^{-1}$, the relaxation time scale due to the elastic modulus is $\tau_e \sim \lambda\mu_o a_o/E_s$, and the time scale for the viscoelastic membrane is $\tau_v \sim \mu_s/E_s$, where $\lambda = \mu_i/\mu_o$ is the viscosity contrast between interior and exterior fluids, and a_o is the equivalent radius considered as the length scale. The capsule response is governed by the largest of these time scales. The ratio τ_e/τ_f is the capillary number $Ca = \dot{\gamma}\mu_o a_o/E_s$, whereas the ratio $\lambda\tau_v/\tau_e$ is the dimensionless membrane viscosity defined as $\eta^* = \mu_s/\mu_o a_o$. In addition, the time scale associated with the bending modulus is $\tau_b \sim \lambda\mu_o a_o^3/E_b$, and the ratio τ_e/τ_b is the dimensionless bending stiffness $E_b^* = E_b/a_o^2 E_s$. The dimensionless time is denoted by t^*, and defined as $t\dot{\gamma}$. Our focus is in the range $\tau_f \sim \tau_e \sim \tau_v$. Thus, the three main dimensionless parameters are Ca, η^* and λ. Moreover, in the limit of a large membrane viscosity and a large elastic modulus, $\tau_v \gg \tau_e$. Then the ratio $\lambda\tau_v/\tau_f \equiv \beta$ can be considered as the relevant parameter [52].

Experimental measurements of the membrane viscosity of capsules are relatively scarce. Chang & Olbricht [54] estimated μ_s from their experiments using artificial capsules, which in dimensionless form yielded $\eta^* \approx 6$. In case of red blood cells, there is more information available on the membrane viscosity, although the range of the reported values is rather wide. For example, Tran-Soy-Tay *et al.* [8] estimated $\mu_s \approx 10^{-7}$ (N.s/m) from the analysis of cell tank-treading frequencies, whereas Evans & Hochmuth [88] found $\mu_s \approx 10^{-6}$ (N.s/m) based on their micropipette aspiration and cell relaxation technique. Thus, η^* in the range ~ 10 appears to be most relevant. For the sake of a comprehensive analysis, here we consider a range of η^* from 0 to 100. The capillary number is varied from 0.05 to 1, and the viscosity ratio λ from 0.2 to 5.

Similarly, for RBC with purely elastic membrane, the relevant dimensionless parameters are (i) the capillary number Ca; (ii) the viscosity ratio λ and (iii) the dimensionless bending rigidity, E_b^*. Further, the nondimensional spontaneous curvature is set to $c_o a_o = -2.09$ [94]. For a normal cell, $E_s \approx 2 - 6 \times 10^{-6}$ N/m, and $E_b \approx 1 - 5 \times 10^{-19}$ N-m [2, 3, 13]. The area dilatation parameter C is varied from 50 to 400 to ensure that the global and local area dilatation is less than 0.5%. Note that for a real cell the parameter $C \sim 10^5$; however, using such a high value results in numerical instability. It appears that numerical instability occurs at progressively lower values of C as Ca decreases. The range of C used here is found using a series of numerical tests so that the area can be conserved as far as possible without creating numerical instability. Hence, the RBC surface is nearly, not entirely, area-incompressible in our model.

In case of vesicles, three relevant dimensionless parameters are the excess area Δ, the viscosity ratio λ, and the capillary number $\chi = \mu_o \dot{\gamma} a_o^3 / E_b$ defined as the ratio τ_b / τ_f. In our simulations, Δ is varied from 0.12 to 2.17. The corresponding range of the reduced volume $V^* = (1 + \Delta/4\pi)^{-3/2}$ is 0.99 to 0.79. The viscosity ratio λ and the capillary number χ are varied from 1 to 14, and 0.2 to 50, respectively. The nondimensional spontaneous curvature is set to $c_o a_o = 0.0$ for all prolate vesicles. In addition, a series of tests are performed to set an appropriate value of the prefactor C in (2.29). It is found that for the values of $O(10^3)$, the vesicle surface area is conserved within 0.4% globally and locally.

The non-linear terms in the Navier-Stokes equations are retained in the computation; however, the Reynolds number $Re = \rho\, a_o^2\, \dot{\gamma} / \mu_o \approx 10^{-2}$, and hence, the effect of inertia is negligible.

2.5 Grid Resolution Test and Domain-size Effect

The code we use in this study was initially used to model the dynamics and deformation of capsules with elastic membrane. This code has been previously validated against the theories, experiments and several other boundary integral and front-tracking numerical results. A detailed validation of the methodology and test of numerical convergence was given in [61, 63] for initially spherical capsules with no bending rigidity. Here we present several numerical tests for different Eulerian and Lagrangian grid resolutions, and domain-size effects on the deformation and orientation of a vesicle in linear shear flow.

The computational domain is a cubic box of length $2\pi a_o$, and contains one vesicle of equivalent radius a_o. The domain is discretized using a fixed (Eulerian) rectangular and uniform grid of 120^3 points. For this resolution, there are about 38 Eulerian points across the diameter of the equivalent sphere. Thus the flow field inside the vesicle is well resolved.

Figure 2.4(a) and (b) present the convergence tests for the Eulerian and Lagrangian resolutions, respectively. Fig. 2.4(a) shows the two-dimensional contours of the steady-state shape of a tank-treading vesicle in the shear plane for three different Eulerian grids: 80^3, 120^3, and 160^3, while the Lagrangian resolution is kept constant at 5120 triangles. No significant difference is observed between the three cases, and thus, 120^3 resolution is used in this study. Fig. 2.4(b) shows the result for three different Lagrangian resolutions: 1280, 5120, and 20480 triangles, while the Eulerian resolution is fixed at 120^3. The result for 1280 elements is slightly different from the other two, whereas 5120 and 20480 resolutions give almost the same shapes. Tables 2.1 and 2.2 present the Taylor deformation parameter $D = (L-B)/(L+B)$, where L

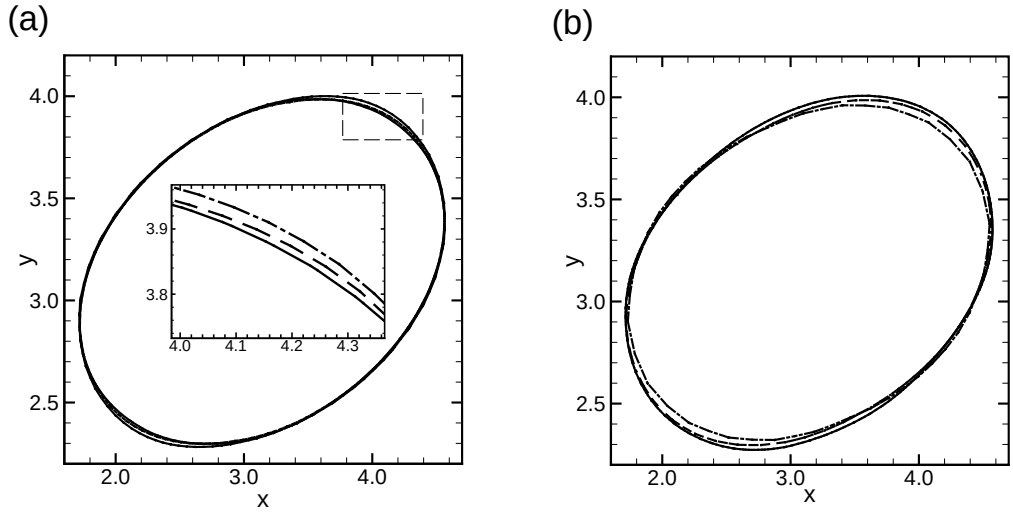

Figure 2.4: (a) Convergence test of Eulerian resolution: —— 80^3, - - - 120^3, -·-·- 160^3; The inset shows the magnified view of a part of the contours. (b) Convergence test of Lagrangian resolution: -·-·- 1280; - - - 5120; —— 20480 triangles.

Table 2.1: Convergence of deformation parameter D, and tank-treading inclination angle θ/π for different Eulerian resolutions. The Lagrangian grid is fixed at 5120 elements. Here $\Delta = 0.63$, $\lambda = 5$, $\chi = 50$.

No. of points	D	θ/π
40^3	0.265	0.094
80^3	0.298	0.080
120^3	0.299	0.077
160^3	0.299	0.077

and B are the capsule semi-major and -minor axes in the shear plane, respectively [see Fig. 1.2], and inclination angle θ for different Eulerian and Lagrangian resolutions, which confirm that convergence is attained for 120^3 mesh.

In order to verify the accuracy of the surface fitting method used to obtain the curvatures, and their discrete gradients, we compare the numerically obtained values with the exact (analytical) values for a fixed oblate spheroid with an excess area $\Delta = 1.62$. The normalized $\mathcal{L}_2$ error is defined as $\mathcal{L}_2 = \left\|\mathbf{V} - \hat{\mathbf{V}}\right\|_2 / \|\mathbf{V}\|_2$, where $\mathbf{V}$ and $\hat{\mathbf{V}}$ represent the exact and numerical solutions, respectively. Table 2.3 presents the

Table 2.2: Convergence of deformation parameter D, and tank-treading inclination angle θ/π for different Lagrangian resolutions. The Eulerian grid is fixed at 120^3. Here $\Delta = 0.63$, $\lambda = 5$, $\chi = 50$.

No. of elements	D	θ/π
1280	0.298	0.071
5120	0.299	0.077
20480	0.293	0.081

$\mathcal{L}_2$ error for κ, κ_g, and $\Delta_{LB}\,\kappa$. The $\mathcal{L}_\infty$ error which is the maximum relative error between the numerical and exact values is also given in Table 2.4. Values in Table 2.3 show that the $\mathcal{L}_2$ error can be significantly improved by increasing the number of elements from 1280 to 5120, while only a marginal improvement occurs when the number of elements is further increased to 20480. The same trend can be noticed for $\mathcal{L}_\infty$ error of κ and κ_g. One exception is the $\mathcal{L}_\infty$ error in $\Delta_{LB}\,\kappa$ which first decreases as the number of elements increases from 1280 to 5120, but increases thereafter. It is mentioned in [38] that the convergence of the Laplace–Beltrami operator depends on the mesh structure, and hence, a uniform reduction in $\mathcal{L}_\infty$ error can be achieved for some specific triangulations only. It was noted in Fig. 2.4(b) that the vesicle shape does not show a significant change when the Lagrangian resolution is increased from 5120 to 20480. Hence, the mesh with 5120 elements was used in the simulations of tank-treading and tumbling vesicles for which the shape is found to be smooth. For vesicles near the transition boundary, which show highly complex shapes, it was necessary to use the higher Lagrangian resolution. Our numerical scheme for the calculation of curvatures and their discrete gradients is robust for any smooth surfaces regardless of the shape.

Moreover, we have verified that there is no significant effect on the vesicle dynamics due to confinement by increasing the wall-to-wall distance from $2\pi a_0$ to $3\pi a_0$ and $4\pi a_0$.

Table 2.3: Normalized $\mathcal{L}_2$ error for different Lagrangian resolutions. The shape is an oblate spheroid with $\Delta = 1.62$.

No. of elements	κ	κ_g	$\Delta_{LB}\,\kappa$
1280	0.010	0.017	0.303
5120	0.003	0.005	0.108
20480	0.001	0.002	0.059

Table 2.4: Normalized $\mathcal{L}_\infty$ error for different Lagrangian resolutions. The shape is an oblate spheroid with $\Delta = 1.62$.

No. of elements	κ	κ_g	$\Delta_{LB}\,\kappa$
1280	0.019	0.030	0.360
5120	0.008	0.012	0.166
20480	0.005	0.009	0.321

The tank-treading angles decrease by at most 5%, and the deformation parameter D increases by less than 1% upon increasing the size to $3\pi a_0$; no further changes in θ and D occur upon further increase to $4\pi a_0$. We have also verified that the tumbling and swinging motions, and the transition borders are not affected by increasing the wall-to-wall distance.

While the volume preservation technique presented in Section 2.2.2 has been applied for red blood cells in vacuum [39], we find it to be convenient and consistent within the framework of the immersed-boundary method for fluid-filled vesicles as well, and it also assures that the no-slip condition on the vesicle surface is automatically satisfied as the surface velocity is obtained by interpolating the local fluid velocity. It may be noted that volume preservation could be alternatively performed by using a surface normal velocity. We have performed multiple simulations using this alternate method and found that both methods gave similar results; e.g., for $\chi = 10, \lambda = 1, \Delta = 0.44$, the force method gave $D = 0.257, \theta/\pi = 0.176$, and the velocity method gave $D = 0.256, \theta/\pi = 0.178$. Table 2.5 presents the volume change

and the tank-treading angle θ for a sample case at a high capillary number over a range of the dimensionless values of K_v. We see that from $K_v = 2.5 \times 10^4$ to 4×10^4, there is no significant improvement in volume and θ. After careful tests, we find that $K_v = 2.5 \times 10^4$ is satisfactory for which the volume loss is about 0.12%. It should be emphasized that the volume loss is observed for the nearly spherical vesicles ($\Delta < 0.5$), and not for higher values of Δ. Note that for higher values of Δ, the surface area is higher, and hence, the distance between the Lagrangian nodes are also higher. However, this increased Lagrangian-to-Eulerian mesh size ratio did not cause any increased volume loss. We also observed that increasing the Lagrangian mesh from 1280 to 5120 and 20480 never improved the volume loss for a fixed Eulerian grid spacing of 120^3. This suggests that the volume loss in our simulations is not due to higher Lagrangian-to-Eulerian mesh size ratio. For vesicles near the transition boundary, which show highly complex shapes (Figs. 3.10 and 3.11), we use 20480 Lagrangian resolution for improved curvature estimation. Also, we do not observe local coarsening or entanglement of surface mesh over the length of the simulations; thus, no remeshing is done. Figure 2.2(a) shows the surface mesh on a deformed vesicle; no mesh skewness is seen here. For all reported runs, we have made similar checks that the mesh skewness does not appear. It should be mentioned that no significant volume loss was found in our study on the dynamics of red blood cells, which have highly oblate resting shape ($\Delta \sim 5$), and nearly constant surface area using the same numerical technique.

As discussed earlier in Section 2.3, the viscoelastic model presented in Fig. 2.3 approaches the Kelvin–Voigt model for very large E_1. This means that the capsule dynamics and deformation will be independent of E_1 for large values of E_1. This

Table 2.5: Volume loss and cell inclination angle for different dimensionless values of K_v. Here, $\Delta = 0.44, \lambda = 5$, and $\chi = 50$. The tabulated values are taken at $t^* = 20$.

$\mathbf{K_v}$	θ/π	$\frac{\Delta V}{V_0}$ (%)
5×10^3	0.14	-0.43
2.5×10^4	0.148	-0.12
4×10^4	0.149	-0.07

can be verified in Fig. 2.5, where the deformation parameter D and the major axis inclination angle θ are plotted for different values of non-dimensional E_1^* obtained from our simulation. Note that E_1 is scaled by the elastic modulus E_s; hence, $E_1^* \equiv E_1/E_s$. As E_1^* increases, D increases and θ decreases approaching limiting values. Further increase in E_1^* does not affect D and θ as there are no significant differences between the results for $E_1^* = 50$ and 100. Note that setting a very high value of E_1^* is not numerically feasible as the system becomes stiff and the integration time step should be reduced significantly. Therefore, $E_1^* = 50$ is considered throughout this study.

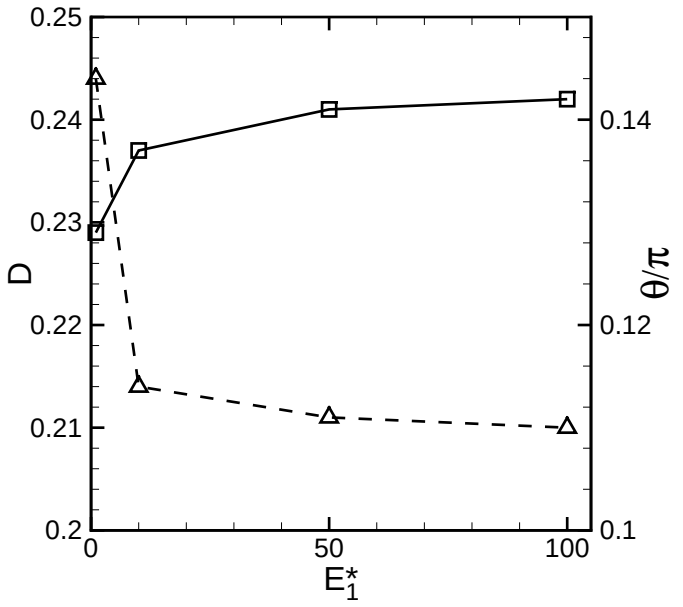

Figure 2.5: Effect of elastic modulus E_1^* on deformation parameter D (left axis, solid line), and inclination angle θ (right axis, dashed line). The model approaches the Kelvin–Voigt model upon increasing E_1^*, and D and θ become independent of E_1^*. Here $Ca = 0.1, \lambda = 1, \eta^* = 10$ and the capsule is initially spherical.

Chapter 3

Dynamics of a Vesicle in Linear Shear Flow

3.1 Introduction

As discussed in Chapter 1, dynamics and deformation of vesicles have been the subject of intense research due to their significance in biological and engineering applications. The role of the controlling parameters on vesicle dynamics, particularly, the capillary number χ, has received a significant attention in the recent years. Numerous theoretical studies have been carried out, starting with Seifert [19], in the framework of perturbation analysis of nearly spherical vesicles ($\Delta \ll 1$) in which the shape is represented by a series of spherical harmonics, and the vesicle dynamics is expressed in terms of two coupled ODEs. In the leading-order analysis of Misbah [48] and Vlahovska & Gracia [49], the χ-dependent terms drop out from the expansion, and the parametric space is reduced to two variables, namely, Δ and λ. Danker *et al.* [21], Kaoui *et al.* [22], and Lebedev *et al.* [20, 50] considered the second-order terms in the expansion up to the second harmonics, and thus, retained the χ-dependence. Lebedev *et al.* [20, 50] showed that the parametric space could still be reduced by introducing two new dimensionless variables S and Λ defined as

$$S = \frac{7\pi}{3\sqrt{3}} \frac{\chi}{\Delta}, \tag{3.1}$$

and

$$\Lambda = \frac{23\lambda + 32}{8\sqrt{30\pi}}\sqrt{\Delta}\,. \tag{3.2}$$

Using these two parameters, a self-similar behavior of the vesicle dynamics was obtained; that is, the transition boundaries between different regimes in the S–Λ plane were found to be independent of Δ. Experimental works by Steinberg's group [6], and a recent analysis of their data by Zabusky *et al.* [28] tend to suggest that the data can be presented in the two-parameter phase diagram proposed by Lebedev *et al.* [20, 50], within the margin of uncertainty in the experiments, despite the fact that the experimental observations did not support some key assumptions in the models. In addition to the fact that the models are strictly applicable to nearly spherical vesicles, they are also based on the assumptions that the thermal fluctuations (except Seifert's [19]), and the odd harmonics in the vesicle shape, are neglected.

The notion of self-similarity in vesicle dynamics, however, remains an issue of recent debate. In contrast to the model of Lebedev *et al.* [20, 50], the models of Danker *et al.* [21] and Kaoui *et al.* [22] found that the self-similar solution did not exist, and the dynamics explicitly depended on the three parameters, χ, λ, and Δ. Farutin, Biben & Misbah [23] included the fourth-order harmonics in the expansion, resulting a 14-ODE model, and also found the absence of the self-similarity. Very recently, Biben, Farutin & Misbah [24] used a 3D boundary integral simulation to study vesicle dynamics in shear flow, and concluded that the self-similarity did not exist. Using the self-similarity model, Zabusky *et al.* [28] showed that all experimental tank-treading angle θ for different Δ collapsed to a single line when plotted against Λ (excluding the data points which are presumed to be affected by thermal noise).

Further, the boundary integral simulations of Kraus *et al.* [43] predicted that the tank-treading angle was independent of χ. In contrast, all higher-order theoretical models found an explicit dependence of θ on χ.

The above discussion clearly suggests that further analysis is necessary with regard to the parametric space that controls the vesicle dynamics, without the limitation imposed by the assumption of the quasi-sphericity, in particular. The first objective in this chapter is to provide further insight to the parametric dependence and the self-similar behavior of the vesicle dynamics in the range of $\Delta = O(1)$ using a three-dimensional direct numerical simulation in which vesicle deformation is fully resolved but thermal noise is neglected.

In addition, quantitative data on vesicle deformation is relatively scarce. The vesicle shape changes from its initial shape under the application of the shear, while the volume and surface area remain constants. In their experiments, de Haas *et al.* [25] observed that deformation increased non-linearly with increasing shear rate and tend to saturate at large values. Seifert's theoretical work [19], which included thermal noise, predicted a linear behavior in the limit of vanishingly small shear rate, and a deformation saturation at large shear rates similar to that observed by de Haas *et al.* [25]. Kantsler & Steinberg [15] also observed a similar crossover behavior, and saturation of deformation at large shear rate. Here, we present a quantitative comparison of the theoretical and experimental results with our 3D simulation results.

Another objective is to analyze the shape dynamics for vesicles in the transition regime. As mentioned above, highly convoluted shapes are observed for the trembling vesicles in the experiments. These shapes are drastically different from those

predicted for the vacillating-breathing vesicles by Danker *et al.* [21] in which the vesicle shape remains nearly elliptical during its oscillation. In this chapter, we show that our simulations are able to predict that, in the absence of thermal noise, both the vacillating-breathing mode characterized by relatively smooth elliptical shapes, as well as the trembling mode characterized by complex shapes with concave regions are possible.

We present a comprehensive analysis of the scaling of tank-treading angles, and the deformation, followed by the analysis of vesicle shapes in the transition zone, and the phase diagrams.

3.2 Analysis of Tank-treading Vesicles

First we present the results for the tank-treading vesicles, and address the scaling issues related to the inclination angle. For the range of Δ considered here ($\Delta \leq 2.17$), only a prolate equilibrium shape is possible [26]. First, we verify that by starting with an initially oblate or prolate shapes, our numerical technique leads to the same final shape. This is illustrated in Fig. 3.1(a)-(b) where the shape evolution is shown for a vesicle of an initially oblate shape at $\Delta = 0.88$. The final shape after the initial transience shows that the vesicle has assumed a prolate-like shape. A marker particle on the surface is tracked over time to show the tank-treading motion. Fig. 3.1(c) shows the time evolution of the semi-major axis L, semi-minor axis B, the half of the end-to-end length in the vorticity direction, Z, and the major-axis inclination angle θ for initially oblate and prolate shapes, but at the same value of Δ. It is clear that both shapes reach the same final steady-state as L, B, Z, and θ approach the same values.

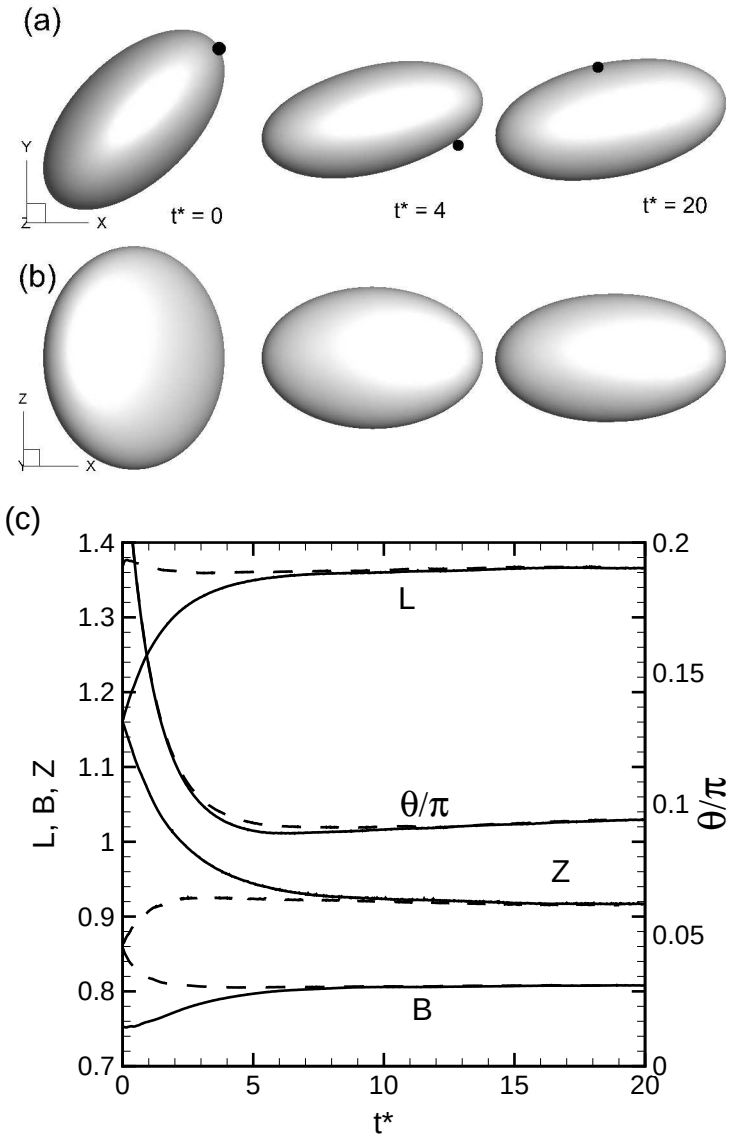

Figure 3.1: Sample results on a tank-treading vesicle and oblate-to-prolate transition. (a) and (b) shows the time-lapse shapes viewed along the vorticity direction and velocity gradient direction, respectively, for $\Delta = 0.88, \chi = 50, \lambda = 5$. A marker point (black dot) is shown in (a) to illustrate the membrane tank-tread. (c) Time evolution of semi-major axis L, semi-minor axis B, the half of the end-to-end length Z in the vorticity direction, and the tank-treading angle θ for initially oblate (——) and prolate (- - -) vesicles for $\Delta = 0.44, \chi = 50, \lambda = 5$. Both initial shapes lead to the same final results. All lengths are scaled by a_o.

3.2.1 Dependence of θ versus Δ

The dependence of the tank-treading inclination angle θ (angle between the major axis and the flow direction x) on the excess area Δ is shown in Fig. 3.2. The simulation data is presented for a fixed value of the capillary number $\chi = 10$ in the figure, but different values of the viscosity ratio λ. The present front-tracking simulation results are compared with the boundary integral simulation results of Kraus *et al.* [43] (who considered $\lambda = 1$ only), the recent spectral boundary integral simulations by Zhao & Shaqfeh [29] ($\lambda = 1$ and 2.7 from their simulations), and the experimental results of Steinberg and co-workers. The data points for the experimental results and the associated error bars are extracted from Fig. 4 in Zabusky *et al.* [28]. In general, the present results agree well with the experimental results and the earlier boundary integral simulations; however, certain subtle points must be mentioned. As noted in [6, 16, 28], each experimental data point represents an ensemble-averaged value over some bins of Δ obtained from more than 500 individual measurements. In the early measurements of Kantsler & Steinberg [15, 16], the uncertainty of a_o, Δ, and λ was up to 20%. In the newer measurements of Deschamps *et al.* [6], the uncertainty of a_o and Δ was 3.5% and 16%, leading to the maximum errors of 25% and 8% in S and Λ, respectively, though the inclination angle uncertainty was not reported. Given the error bars of the experimental data, we can conclude that there are very good agreements between the present results and the experimental data.

The qualitative trend of θ versus Δ suggests a power-law dependence at smaller values of Δ, but much slower decay at higher values. According to Zabusky *et al.* [28], thermal fluctuations become significant at higher values of Δ (and, lower θ) causing the slower decay similar to what was observed in [30] in MPC simulations

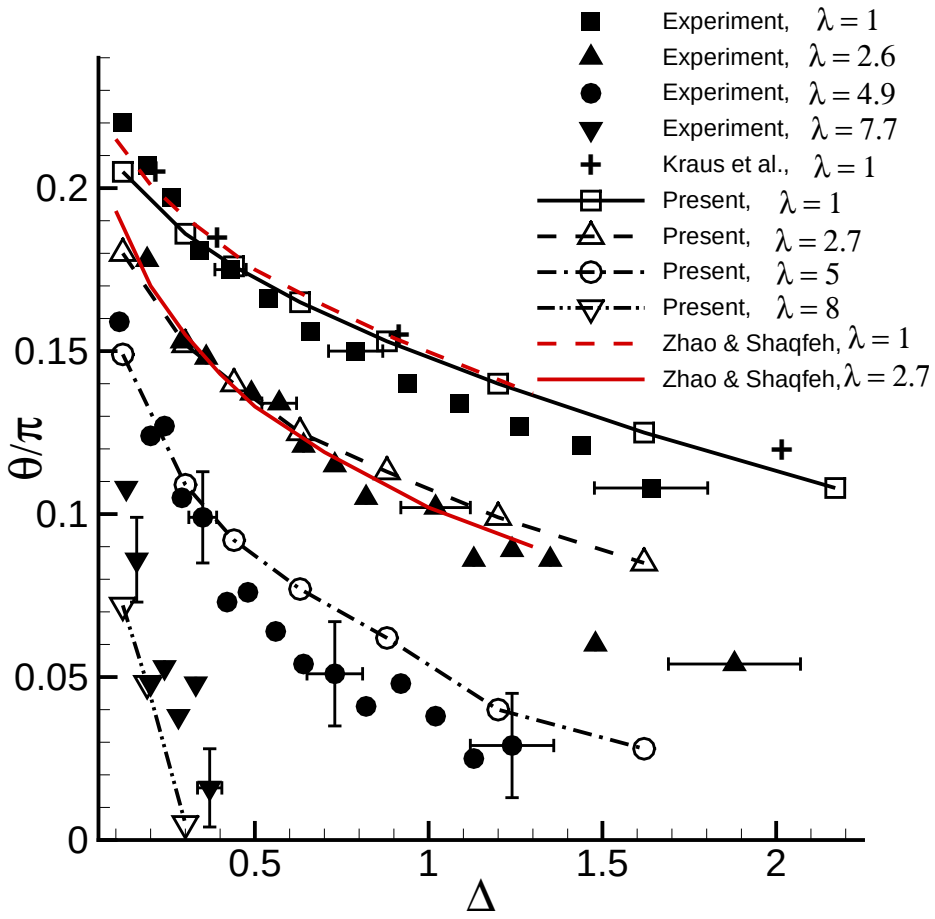

Figure 3.2: Effect of the excess area Δ on the inclination angle for tank-treading vesicles at different values of the viscosity ratio λ. Numerical results are shown by open symbols and lines, and for a fixed capillary number $\chi = 10$. Comparison is done with the experimental results (filled symbols) from Steinberg and coworkers, boundary integral simulations by Kraus *et al.* [43] (+), and spectral boundary integral simulations by Zhao & Shaqfeh [29]. The experimental data and the error bars are taken from Fig. 4 of Zabusky *et al.* [28].

that implicitly included thermal noise. However, the present results which do not include thermal noise tend to suggest that the thermal noise is not the only factor that is responsible for the slower decay of θ. As a matter of fact, it can be said from Fig. 3.2 that the decay rate observed in our results is slower than that observed in the experiments, despite an increasingly large scatter in the experimental data at higher Δ.

We now study the effect of capillary number χ on the numerical results. For this, we consider three values of $\chi = 1$, 10, and 50. The θ versus Δ curves are plotted in Fig. 3.3 for $\lambda = 1$, 2.7, 5, and 8, each for $\chi = 1$, 10, and 50. Two important observations are made here. First, for $\lambda = 1$ and 2.7, the inclination angle is nearly independent of χ; only a weak dependence on χ is observed for low values of Δ. This result is in agreement with that of Kraus *et al.* [43] who observed almost no χ-dependence for $\lambda = 1$. On the contrary, a χ-dependence can be clearly seen for $\lambda = 5$ and, in particular, for $\lambda = 8$. Thus, the χ-dependence appears in the numerical results as λ increases. The same trend can be observed in the work by Zhao & Shaqfeh [29] where the χ-dependence of inclination angle becomes more significant upon increasing λ. We have included two data points from their work for comparable parameters: $\lambda = 1$, $\Delta = 0.44$, $\chi = 1$ and 10, which match very well with ours. The second observation is regarding the saturation of θ at large χ. As evident from the figure, the inclination angle first decreases as χ increases from 1 to 10; beyond $\chi \approx 10$, the inclination angle shows no significant change. Thus, the results for $\chi = 10$ and 50 in the figure are found to coincide. This saturation of θ at large shear rates is related to vesicle deformation. As will be shown later, the vesicle elongates more with increasing χ for up to $\chi \approx 10$. Hence, the inclination angle increases as a more elongated shape

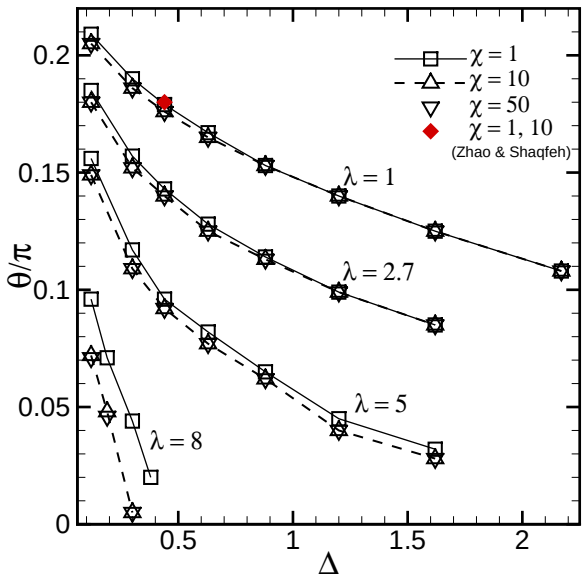

Figure 3.3: Simulations results showing the effect of χ on the θ versus Δ plot. For each value of λ, from 1 to 8, three values of χ are considered. The numerical results show a χ-dependence at $\lambda = 5$ and 8. The red diamonds are data from Zhao & Shaqfeh [29] for $\lambda = 1$, $\Delta = 0.44$, and $\chi = 1$ and 10.

seeks to align with the flow direction. We find that the vesicle deformation saturates beyond $\chi \approx 10$, and so does the angle.

As mentioned before, all theoretical models except Misbah's [48] predict an explicit dependence of the inclination angle on the capillary number χ. Therefore, we now compare the numerical results with the theoretical models as done in Fig. 3.4(a). We consider the higher-order models of Danker *et al.* [21] (hereafter, referred to as DBPVM), Kaoui, Farutin & Misbah [22] (hereafter, referred to as KFM), Lebedev, Turitsyn & Vergeles [20, 50] (hereafter, referred to as LTV), and the leading order model of Misbah [48]. In the DBPVM model, the vesicle dynamics is expressed in terms of the inclination angle θ and a variable Θ associated with the vesicle shape

defined as $\mathcal{R} = \sqrt{\Delta}\cos\Theta/2$ where $\mathcal{R}$ is the amplitude of deformation. Then,

$$\tau\frac{\partial\theta}{\partial t} = \frac{S}{2}\left[\frac{\cos 2\theta}{\cos\Theta}\left(1+\sqrt{\Delta}\Lambda_2\sin\Theta\right)-\Lambda\right], \tag{3.3}$$

$$\tau\frac{\partial\Theta}{\partial t} = -S\sin\Theta\,\sin 2\theta+\cos 3\Theta+\sqrt{\Delta}\Lambda_1 S\left(\cos 4\Theta+\cos 2\Theta\right)\sin 2\theta + \sqrt{\Delta}\Lambda_2 S\cos 2\Theta\,\sin 2\theta\,, \tag{3.4}$$

where

$$\tau = \frac{7\sqrt{\pi}(23\lambda+32)}{72\sqrt{10}}\frac{\chi}{\dot{\gamma}}, \tag{3.5}$$

$$\Lambda_1 = \frac{\sqrt{10}}{28\sqrt{\pi}}\left(\frac{49\lambda+136}{23\lambda+32}\right), \tag{3.6}$$

and

$$\Lambda_2 = \frac{10\sqrt{10}}{7\sqrt{\pi}}\left(\frac{\lambda-2}{23\lambda+32}\right). \tag{3.7}$$

The terms involving Λ_1 and Λ_2 are the higher-order terms. From the DBPVM model, one can obtain the KFM model by setting $\Lambda_2 = 0$, the LTV model by setting $\Lambda_1 = \Lambda_2 = 0$, and Misbah's [48] model by setting $\Lambda_1 = \Lambda_2 = 0$, and omitting the $\cos 3\Theta$ term. We solve the above system of ODEs for a tank-treading vesicle for which the inclination angle and the shape are fixed so that the left hand sides of (3.3) and (3.4) are zero. A close form solution exists for Misbah's [48] model as $\theta = (1/2)\cos^{-1}\left[(23\lambda+32)\sqrt{15\Delta}/120\sqrt{2\pi}\right]$. These theoretical results and the linearized form of Misbah's [48] model, $\theta = \pi/4-(23\lambda+32)\sqrt{15\Delta}/240\sqrt{2\pi}$, are shown in Fig. 3.4(a) and compared with the present front-tracking simulations. To avoid cluttering of the data, we consider $\chi = 1$ and $\lambda = 1$ and 5. The figure shows that the difference

between the DBPVM, LTV and KFM model is not significant but they differ from Misbah's model.

When we compare our numerical results with the above theoretical models (Fig. 3.4(a)), we find an agreement at small Δ but not at higher Δ, as expected, since these models are applicable to vesicles of nearly spherical initial shapes ($\Delta << 1$). Interestingly, Misbah's [48] leading-order model predicts better the numerical results than the other three models. The differences between the simulation results and the theoretical results are found to increase quite significantly with increasing λ. Further, the numerical results predict a much slower decay of θ than the theoretical models, particularly for $\lambda \geq 5$. Hence, the theoretical models deviate from the numerical results not only at large values of Δ, but also at large values of λ. Therefore, while we find that that the inclination angle (weakly) depends on the shear rate as in the theoretical models, the exact nature of the dependence differs.

Fig. 3.4(b) compares the χ-dependency in theoretical models and simulations. We consider only the DBPVM model and plot the results from this model for $\chi = 1$, 10, and 50, and compare with the numerical results. There are some subtle but important differences between the two results. For $\lambda = 1$, the theoretical curves for different χ nearly collapse at lower Δ but diverge at higher Δ. In contrast, the numerical results predict the opposite trend. This discrepancy might be in part due to the fact that the theoretical models are valid for small Δ. Second, for higher λ, the theoretical curves for different χ are indistinguishable but the numerical results show a strong dependence on χ.

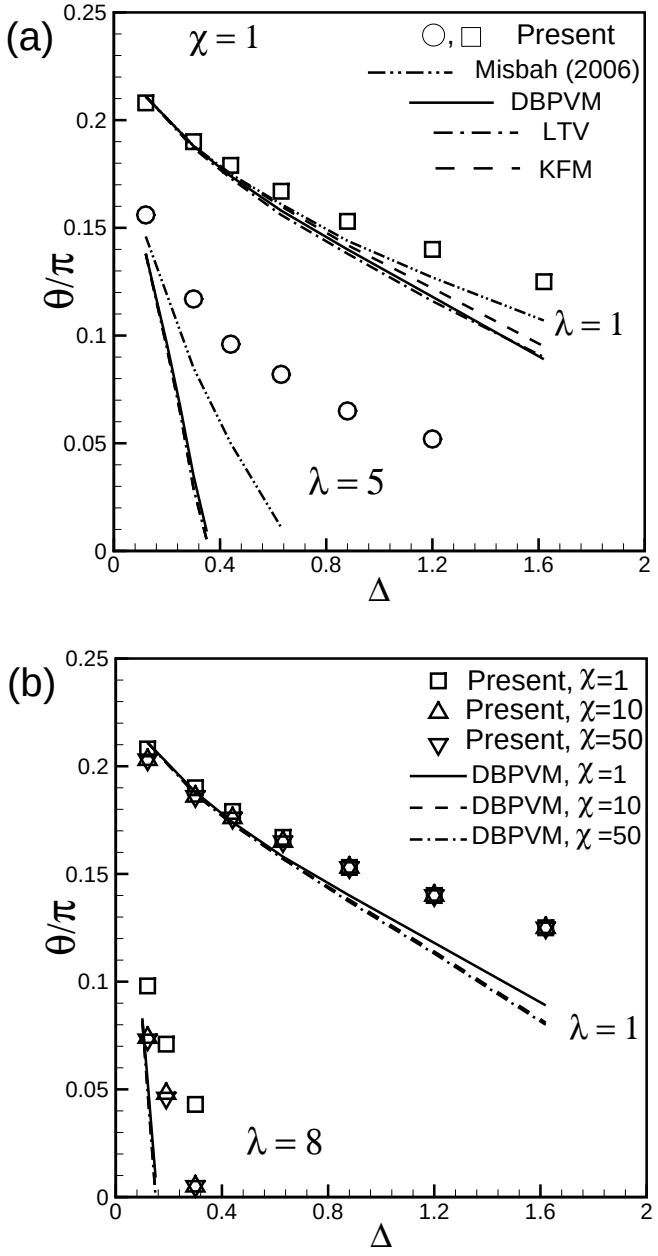

Figure 3.4: (a) Comparison of the present numerical results (θ versus Δ plots) with the theoretical models for a constant $\chi = 1$, but two values of $\lambda = 1$ and 5. Theoretical models of Misbah [48], Danker *et al.* [21] DBPVM, Lebedev *et al.* [20, 50] LTV, and Kaoui *et al.* [22] KFM are considered. (b) Comparison by varying χ as 1, 10, and 50, for two values of $\lambda = 1$ and 8. Here only the DBPVM model is compared to avoid cluttering of the data.

3.2.2 Dependence of θ on Λ

Zabusky *et al.* [28] found that the experimental TT angles θ for different Δ collapsed when they were plotted against Λ despite the scatter in the data due to thermal fluctuations. This finding has motivated us to present our numerical results for TT angles w.r.t Λ as well. Figure 3.5 shows the present numerical results for two different values of $\Delta = 0.12$ and 0.44 (Figs. 3.5(a) and (b), respectively), and the experimental data points for the closest Δ values obtained from Fig. 6 of Zabusky *et al.* [28]. Also, in the same figure, we show the DBPVM theoretical solution, and the solution given in [48], namely, $\theta = (1/2)\cos^{-1}\Lambda$. Note that the numerical results and the theoretical results by DBPVM both are presented for three values of $\chi = 1$, 10, and 50. It is clear from the figure that both the numerical and the experimental results agree well with each other within the error bars of the experiments (despite the lack of thermal noise; see error bars here and in Fig. 3.2). On the contrary, They both disagree with the theories not only for large values of Δ (e.g., for $\Delta = 0.44$ in Fig. 3.5(b)), but also for large values of Λ.

Further, the theoretical curves for different values of χ are almost identical for small Λ and start to branch out as Λ increases, where the difference between $\chi = 1$ and $\chi = 10$ is more prominent. A similar trend can also be identified for the numerical results. The numerical results for $\chi = 10$ and $\chi = 50$ are almost the same for all range of Λ, but differ from those at $\chi = 1$. Thus, a collapse of data for all χ values is found in our numerical results only for small values of Λ. For higher values of Λ, a collapse may occur for $\chi \gtrsim 10$ when vesicle deformation saturates.

Now we present θ for all the numerical data points w.r.t Λ for all Δ and χ in Fig. 3.6. The figure shows that the data collapse very well for approximately $\Lambda < 1$, where

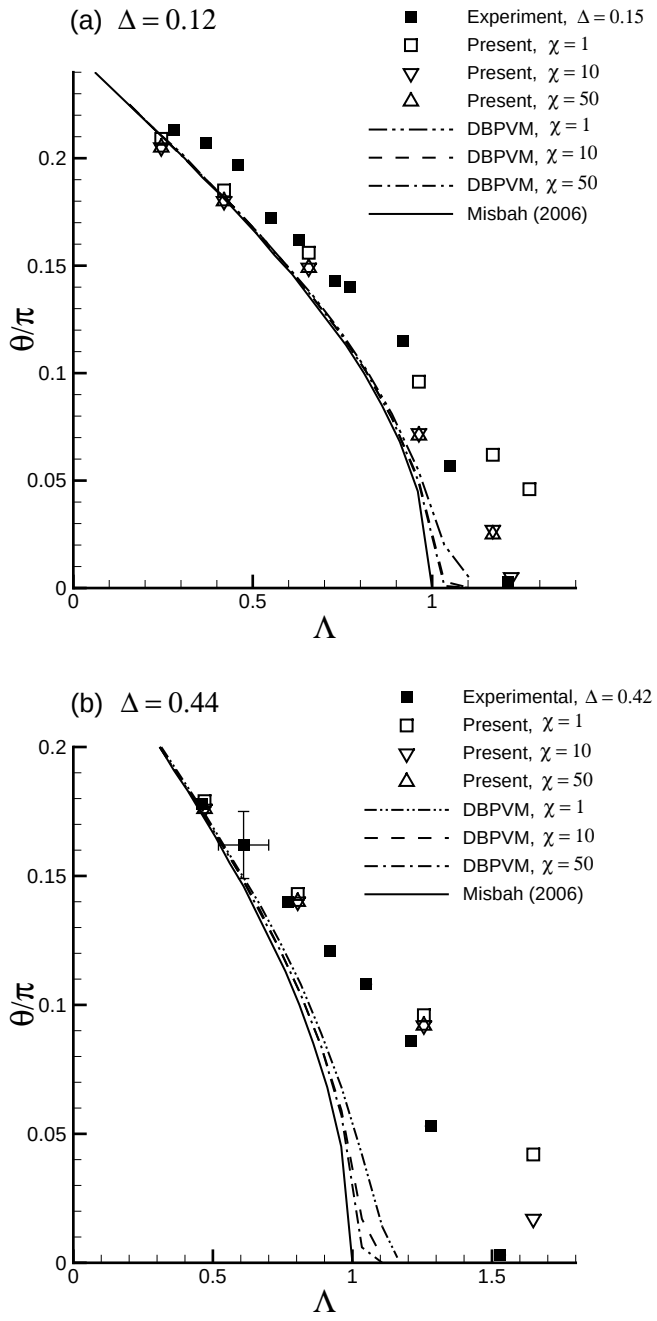

Figure 3.5: Tank-treading inclination angle as a function of Λ. The numerical (open symbols), and theoretical (lines without symbols) data are plotted for different values of χ; the experimental (filled symbols) data are taken from Fig. 6 of Zabusky *et al.* [28]. (a) $\Delta = 0.12$; (b) $\Delta = 0.44$.

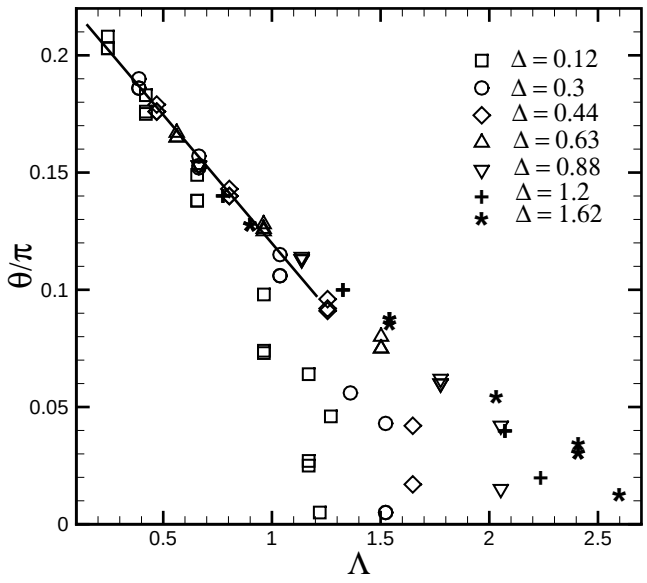

Figure 3.6: Simulation results of tank-treading inclination angles θ vs. Λ plotted for all values of Δ and χ considered in the simulation. For each Δ, values of χ chosen are 1, 10, and 50. A collapse is possible for approximately $\Lambda < 1$, but not for higher values.

they can all be fitted by a straight line. The rest of data for $\Lambda > 1$, however, show a more scattered behavior and strongly vary with Δ. Zabusky *et al.* noted that the quality of the experimental data did not allow one to distinguish between different sets of Δ, and hence, a two-parameter scaling was sufficient within the error bars. Based on our simulation results, it is very clear that the scaling of the TT angles θ using a single variable Λ is *only valid for small values of* Λ. The breakdown of the scaling at higher Λ occurs even in the absence of thermal noise.

3.2.3 Critical viscosity ratio

If the data in the linear regime ($\Lambda < 1$) in Fig. 3.6 is fitted by a straight line, the intercept of this line with $\theta = 0$ can be taken as the critical Λ_c for the onset of the

unsteady dynamics. Λ_c, thus obtained, is a constant and independent of Δ. It is informative to compare the value of Λ_c obtained from our simulations with the theoretical and experimental values. The linear approximation of the theoretical expression of θ obtained by Misbah [48] and LTV gives $\Lambda_c = 1.57$ and 1.81, respectively. Using all Δ values (excluding the ones affected by thermal noise), Zabusky *et al.* [28] obtained $\Lambda_c = 1.74 \pm 0.2$ for the experimental data. Our simulation results yield $\Lambda_c = 1.78$ which is very close to the value found by Zabusky *et al.* and by LTV.

If one assumes that Λ_c is a constant, then the critical viscosity ratio λ_c varies as $\Delta^{-1/2}$. In reality, however, this scaling is not possible due to the slow (non-linear) decay of θ as well as the breakdown of the scaling at higher Λ, as the transition is approached (see Fig. 3.6). Indeed, Kantsler & Steinberg [16] found that $\lambda_c \sim \Delta^{-0.24\pm0.02}$ based on their experiments. We have examined the dependence of λ_c on Δ based on the numerical results and plotted them in Fig. 3.7. In order to estimate the exponent, without extrapolating the linear fit up to $\theta = 0$, we conducted simulations to clearly find when the TT angle falls to zero. The critical viscosity ratio thus obtained are presented in Fig. 3.7 for $\chi = 1$ and 10. We have verified that the transition threshold for $\chi = 50$ is the same as that of $\chi = 10$; hence, the $\chi = 50$ results are not shown. For each value of Δ, simulations are performed in small increments of λ, until the vesicle is observed to align at $\theta = 0$ while undergoing a steady tank-treading. The corresponding value of λ is considered as the lower bound of λ_c. If λ is further increased, the vesicle shows an oscillatory dynamics with periodic shape deformation. The onset of the oscillatory motion is taken to be the upper bound. These two bounds are plotted in the figure for $\chi = 1$ and 10. Remarkably, for approximately $\Delta > 0.5$, the results for two different χ values coincide with each other.

Next, we find the curve fits through the data for $\chi = 1$ and 10. The fits obey the $\lambda_c \sim \Delta^\beta$ relationship as found by Kantsler & Steinberg [16]. We find the exponent β to be -0.3 for $\chi = 1$, and -0.253 for $\chi = 10$. Hence, the exponent obtained for $\chi = 10$ is in excellent agreement with the experimentally derived exponent of -0.24 ± 0.02 by Kantsler & Steinberg [16]. This agreement is remarkable despite the absence of thermal noise in our simulations. The exponent for $\chi = 1$ data found here is slightly lower than the experimental value, since the experiments were performed mostly for $\chi > 1$. It should be mentioned that the method used to find λ_c is different than those used in previous studies, e.g., in Zhao & Shaqfeh [29] where λ_c was calculated through linear stability analysis of the steady-state solution. In that analysis a steady-state tank-treading motion with negative inclination angles can be achieved for λ values close but less than λ_c, which are not observed here. Further, most theoretical studies, e.g., Farutin *et al.* [23], and analysis of Zhao & Shaqfeh [29] show that λ_c increases with χ. Since here we find λ_c by considering actual simulations in finite steps of increasing λ, it is difficult to conclude from the figure how λ_c depends on χ.

3.2.4 Deformation

The deformation of the tank-treading vesicles is quantified by the Taylor deformation parameter D. Figure 3.8(a) shows D versus χ for different values of Δ, but for a fixed $\lambda = 1$. The results show that deformation first increases with increasing χ, suggesting a nonlinear behavior in the range $1 \lesssim \chi \lesssim 10$. Upon further increase in χ, deformation is found to saturate. This result is qualitatively similar to the experimental findings of Kantsler & Steinberg [15], and the theoretical prediction of Seifert [19], that D is independent of χ for large values.

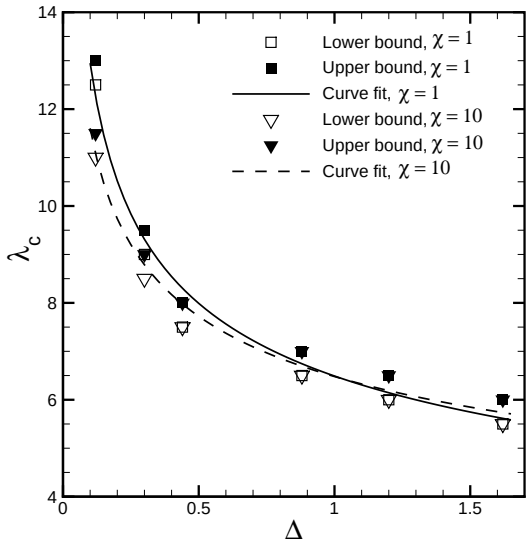

Figure 3.7: Critical viscosity ratio λ_c vs. Δ obtained from the simulations. Open symbols (lower bound) correspond to the λ values for which steady tank-treading at $\theta = 0$ is observed. The filled symbols (upper bound) correspond to the λ for which the major axis starts oscillating. Solid and dashed lines are the curve fits to the data for $\chi = 1$ and 10, respectively. The fits obey the $\lambda_c \sim \Delta^\beta$ relationship, where β is -0.3 for $\chi = 1$, and -0.253 for $\chi = 10$.

It may be noted that thermal effect is usually dominant at small χ as it is the case in Seifert's [19] model and in Kantsler & Steinberg's [15] experiments. Seifert [19] predicted that D increases linearly with χ for vanishingly small values of χ, and shows nonlinear behavior at the cross-over followed by a saturation for sufficiently large values of χ. Kantsler & Steinberg [15] also observed a non-linear behavior of D for small values of χ. It is quite remarkable that a nonlinear behavior of D is possible in the range $\chi \lesssim 10$, even in the absence of thermal noise, as found in our simulations.

Quantitative comparison with Seifert's [19] prediction, Kantsler & Steinberg's [15], and Kantsler *et al.* [27] experimental results is given in Fig. 3.8(b) by plotting D versus $\sqrt{\Delta}$. In this figure, we show all of our data points over the range of λ considered in the simulations, and for $\chi = 1$ and 10. For clarity, $\chi = 50$ data are not shown as they

coincide with those of $\chi = 10$. In the limit of large χ, Seifert predicted

$$D = \sqrt{15\Delta/32\pi}\,. \tag{3.8}$$

In addition to the nearly-spherical limit, Seifert's analysis is also limited to 'weak' external flow. Despite these limitations, the theoretical line seems to match surprisingly well with the simulation results in the approximate range of $\Delta < 1$. For $\Delta > 1$, the theory overpredicts the simulation results.

The experimental data points shown in Fig. 3.8(b) are taken from two sources: from Fig. 5 of Kantsler & Steinberg [15] for the highest values of $\chi E_b/k_B T$ given therein, where k_B is the Boltzmann constant and T is the room temperature, and from Fig. 1 of Kantsler *et al.* [27] by averaging D after it reached a steady state w.r.t. time. Keeping in mind the uncertainty in the experimental data, a good agreement with our simulation results is also evident.

Two interesting observations are worth mentioning. First, the saturation of D occurs at $\chi \approx 10$ which holds for all values of Δ and λ. Second, the trend of D with increasing χ can explain the dependence of θ on χ as noted earlier in Fig. 3.3. For $\chi = 1$ to 10, D increases, and hence, θ decreases as more elongated objects tend to align with the flow direction. Beyond $\chi \approx 10$, deformation saturates, and so does inclination.

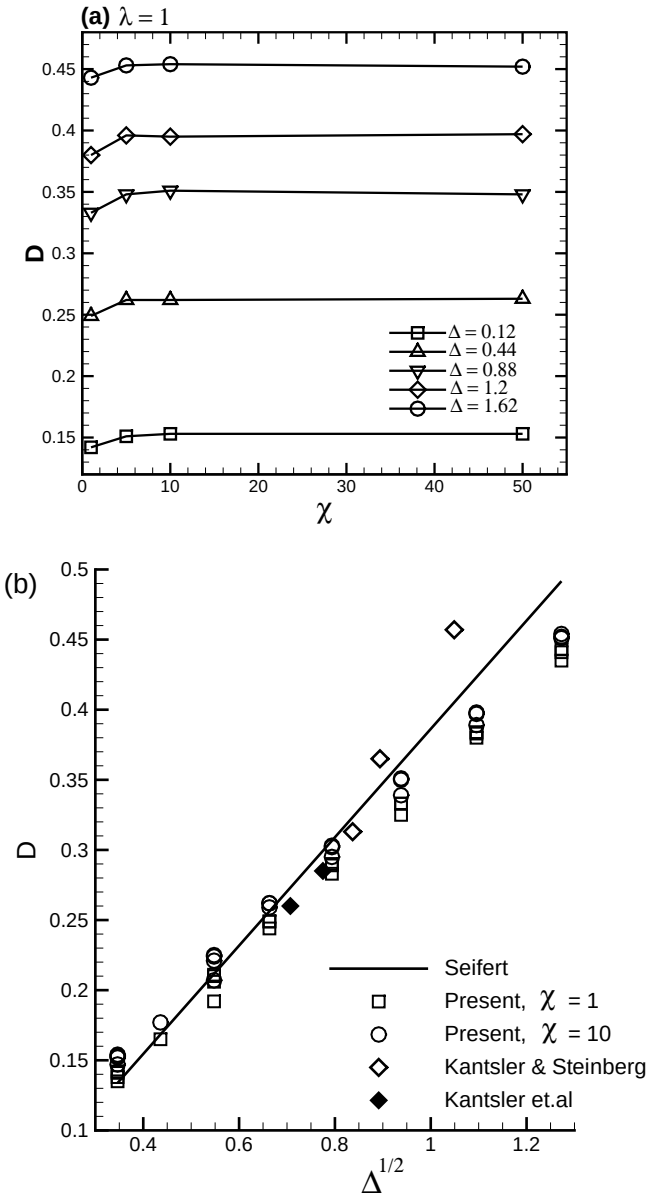

Figure 3.8: (a) Taylor deformation parameter D versus capillary number χ for $\lambda = 1$, and different values of Δ; (b) D vs. $\sqrt{\Delta}$ for all λ considered in the simulations, and for $\chi = 1$ and 10. For clarity, $\chi = 50$ data are not shown as they coincide with those of $\chi = 10$. Also shown in (b) are the theoretical prediction by Seifert [19], and experimental data of Kantsler & Steinberg [15] and Kantsler *et al.* [27]. The experimental data points are taken from Fig. 5 of Kantsler & Steinberg for large χ values (the data points for the highest values of $\chi E_b/k_BT$ given in that paper), and from Fig. 1 of Kantsler *et al.* (averages of D are taken after D reached a steady state w.r.t. time given therein).

3.3 Transition and Tumbling Modes

3.3.1 Analysis of vesicle shapes

We now turn attention to the unsteady regimes of vesicle dynamics. In general, two types of unsteady dynamics are observed. First is the usual tumbling motion resembling a rigid-body flipping. The second dynamics which is more difficult to analyze is the one that occurs on the verge of transition between the TT and TU motion. Depending on the details of the dynamics, this mode has been identified by various names, e.g., the vacillating-breathing (Misbah & co-workers), trembling (Steinberg & co-workers), and swinging (Noguchi & Gompper). Specifically, the vacillating-breathing mode predicted in the theoretical work is characterized by smooth elliptical contours undergoing time-dependent shape oscillation and angular oscillation about $\theta = 0$. In contrast, the trembling mode observed in the experiments is characterized by highly convoluted vesicle shapes. In the present work, both modes are grouped as the 'transition' mode. As will be shown below, our simulations predict that both the vacillating-breathing-like motion, and the trembling-like motion are possible in the transition zone.

Fig. 3.9 shows two sample results for the *vacillating-breathing*-like motion. As evident, the vesicle shape remains nearly elliptical with time while it undergoes angular oscillation about $\theta \approx 0$. A significant shape oscillation accompanies the angular oscillation resembling a breathing-like dynamics. For $\Delta = 0.44$ shown in Fig. 3.9(a), the shapes look qualitatively similar to the contours given in [21]. Higher-order even harmonics are particularly evident in Fig. 3.9(b) where $\Delta = 1.2$ is considered. The

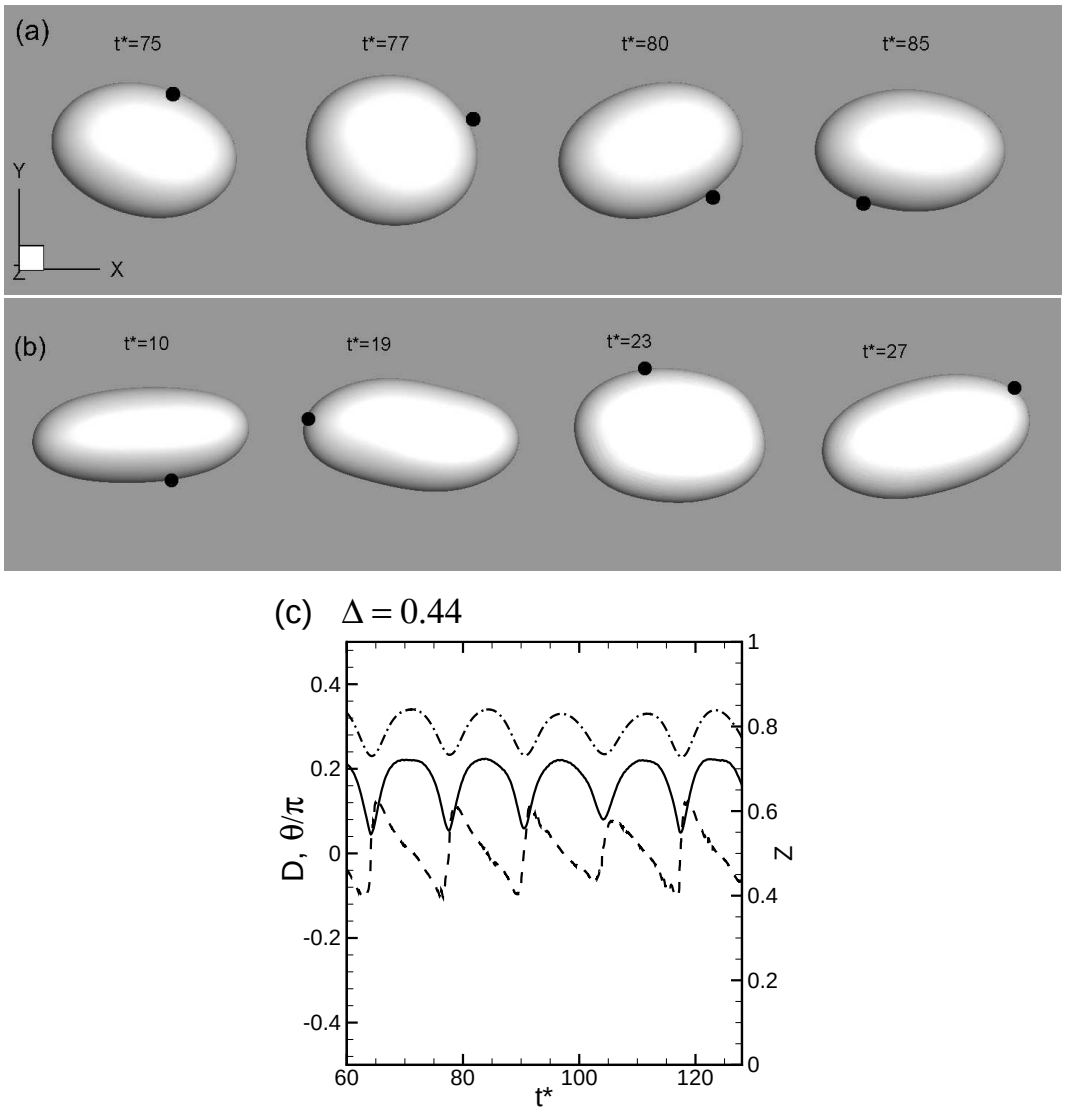

Figure 3.9: Simulation results on the vacillating-breathing like dynamics similar to that predicted by the theories: (a) $\Delta = 0.44$, $\lambda = 10$, $\chi = 5$; (b) $\Delta = 1.2$, $\lambda = 7$, $\chi = 10$. A Lagrangian marker point is tracked in the snapshots which shows that the membrane executes a TT motion. (c) Time-dependent deformation parameter D (left axis, solid line), inclination angle θ (left axis, dashed line), and the half of end-to-end length Z in the vorticity direction (right axis, dash-dotted line) for the case shown in (a).

time-dependent inclination angle θ, deformation parameter D, and the half of the end-to-end length Z in the vorticity direction are plotted in Fig. 3.9(c). Large oscillation in D is observed. Further, Z versus time shows that shape oscillation in the out-of-the-flow-plane direction could be significant as noted by Vlahovska & Gracia [49] in their theoretical work.

The vacillating-breathing-like motion described above occurs in our simulations for low values of χ, and in the vicinity of λ_c which corresponds to the border between the tank-treading and transition zone (See Fig. 3.15 later). For higher values of χ and λ (near the border between the transition zone and tumbling zone), vesicles show convoluted deformed shapes resembling the *trembling*-like behavior. One such result is shown in Fig. 3.10. Remarkably, the vesicle assumes a diamond shape in the x-z plane (view along the velocity gradient direction) periodically when its long axis drops below $\theta = 0$ ($t^* = 19$ and 39 in the figure). The smooth elliptical shape is recovered when the vesicle is aligned above $\theta = 0$. We have performed Fourier transform of the contours of the vesicle in x-y and x-z planes (see later for more details), and found that the fourth harmonics is comparable to the second for the x-z contour when the vesicle is in the compressional quadrant of the flow. In contrast, for the x-y contour, the higher-order harmonics are much weaker compared to the second harmonics. Clearly, the vesicle exhibits more deformation and more harmonics along the vorticity direction than on the shear plane. This result underscores the importance of three-dimensional effects for the vesicles in the transition region.

Another sample result for the *trembling*-like dynamics is shown in Fig. 3.11 corresponding to $\Delta = 1.2$, $\lambda = 7.5$, and $\chi = 50$. The vesicle becomes highly deformed with concavities and lobes when it is aligned in the compressional quadrant ($t^* = 21$ in the

figure). The convoluted shape observed here is qualitatively similar to the experimentally observed shapes (Zabusky *et al.* [28]). The shape is highly three-dimensional with more deformation occurring along the vorticity direction. Fig. 3.11(b) shows the contour of the vesicle in the x-z plane to further emphasize the appearance of concave regions on the vesicle surface. The contour also shows an asymmetry along the z direction implying the presence of the *odd* harmonics.

It is worth mentioning that in our simulations the higher modes are observed mostly when the vesicle is in the compressional quadrant. These instabilities are suppressed when the vesicle aligns in the extensional quadrant, and the smooth elliptical shape is recovered. The vesicle spends a longer time in the extensional quadrant so that the bending forces restore the shape. In the next cycle again the higher modes appear in the compressional quadrant. If the thermal noise were present, these modes would have sustained in the extensional quadrant as well, as observed in the experiments (Zabusky *et al.* [28]). Further, no mesh skewing is observed for such complex shapes, the simulations were done with 20480 Lagrangian elements, and the volume correction is not needed. The irregular shapes observed here are only for the vesicles that are near the transition borderline. For the vesicles that are far away from the transition border, such irregularities are not observed.

Fig. 3.12 shows the Fourier spectra of the vesicle contours shown in Fig. 3.11 for three time instants when the vesicle is within and near the compressional quadrant. We consider the radial amplitude of the contour $R(\phi, t), 0 \leq \phi \leq 2\pi$, relative to the centroid of the vesicle [28], which is Fourier decomposed as $R(\phi, t) = \sum_k \tilde{R}_k(t) e^{ik\phi}$. Higher order even modes beyond the fourth harmonics are observed for both x-y and x-z contours. Odd modes appear in the x-z contour at $\theta/\pi = -0.18$, when the vesicle

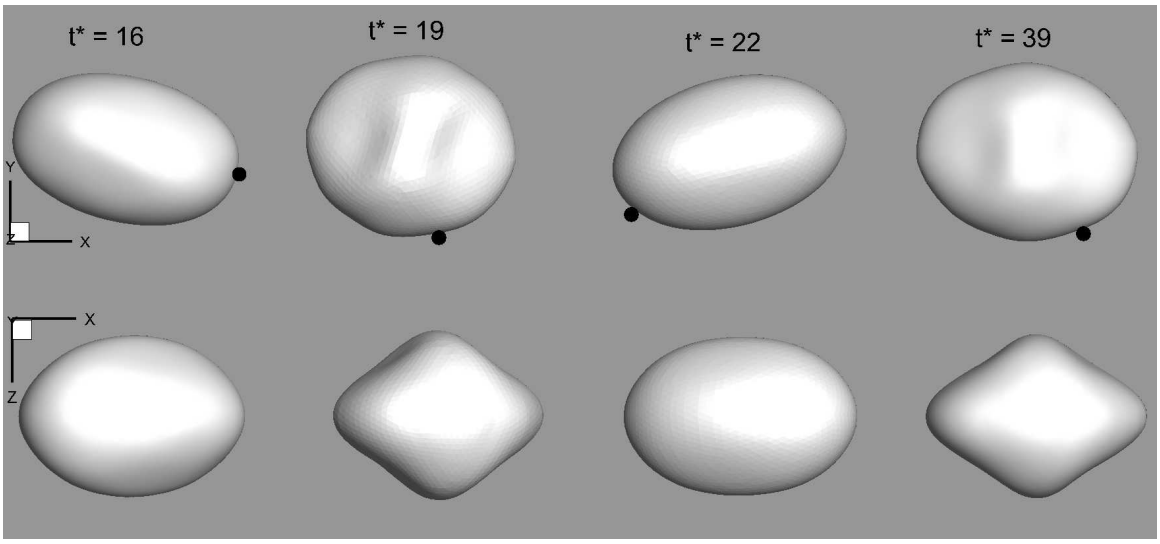

Figure 3.10: Simulation results of a vesicle in the transition region resembling a trembling-like motion. Here $\Delta = 0.44, \lambda = 8, \chi = 50$. Top row shows the view in the shear plane (x-y plane), and the bottom row shows the view along the velocity gradient (x-z plane). Fourth order harmonics are present in x-z contours when the vesicle is aligned in the compressional quadrant ($t^* = 19$ and 39, above). A Lagrangian marker point on the vesicle surface suggests that the membrane makes an oscillatory tank-treading motion.

is near the compressional axis. It should be mentioned that the odd harmonics are generated here by numerical noise.

The convoluted shapes can also appear during the tumbling motion at higher values of χ. One such example is shown in Fig. 3.13(a) for $\Delta = 0.44$, $\lambda = 12$, and $\chi = 50$. Concavity in the vesicle shape is observed here when it is aligned in the compressional quadrant. Of course, the amount of deformation is much less than that observed earlier for the trembling-like motion. The concavities disappear and the smooth elliptical shape is recovered as the vesicle enters the extensional quadrant. Another example is shown in Fig. 3.13(b) at lower values of $\chi = 1$ to illustrate the effect of shear rate on vesicle deformation in the tumbling regime. For this low value of χ the vesicle deformation from its equilibrium is almost negligible, and no membrane concavity is observed.

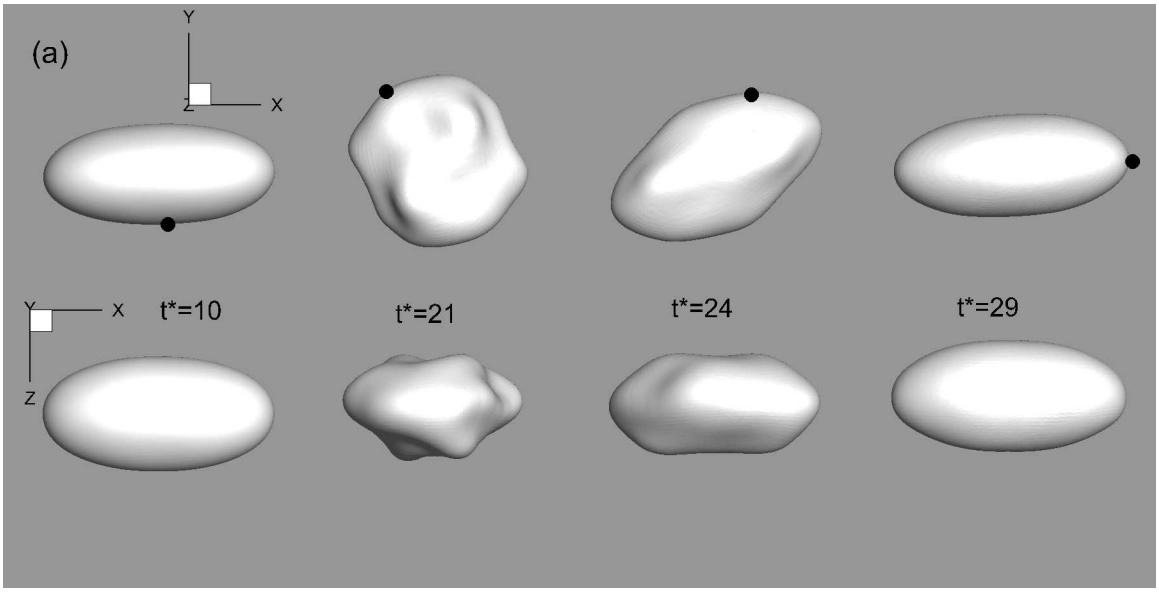

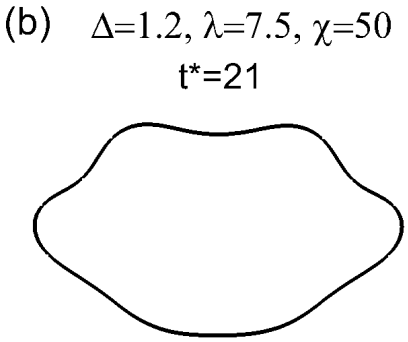

Figure 3.11: (a) Simulation results of a vesicle near the border of transition/tumbling zone resembling a trembling-like motion with highly deformed shape. Here $\Delta = 1.2, \lambda = 7.5, \chi = 50$. Top row shows the view in the shear plane (x-y plane), and the bottom row shows the view along the velocity gradient (x-z plane). A Lagrangian marker point shows that the membrane makes a net tank-treading motion. (b) Vesicle contour is shown in the x-z plane at $t^* = 21$.

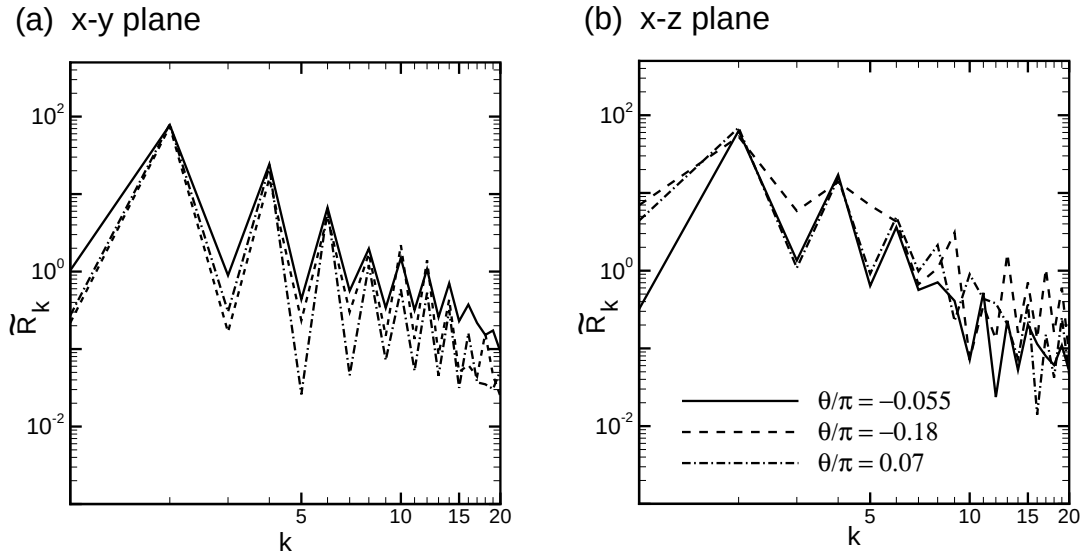

Figure 3.12: Fourier spectra of vesicle contours for $\Delta = 1.2, \lambda = 7.5, \chi = 50$ showing higher modes for three different inclination angles within or near the compressional quadrant. (a) Spectra for x-y contours, and (b) x-z contours. The modes higher than fourth-order, and odd modes in the x-z contours are observed.

3.3.2 Transient dynamics

Within the transition region, we find that the dynamics is often transient in nature; in other words, the vesicle starts with one mode, and then settles to another after a long time. Typically, we find two types of transient dynamics: In the first case, which occurs at the border between the tank-treading and the transition zones, the vesicle starts with a swinging motion and settles to a tank-treading motion; in the second type, it starts with a tumbling motion and gradually relaxes to a swinging motion. The first situation is presented in Fig. 5.13(a) for $\lambda = 8$ and $\chi = 10$. For this case the vesicle initially shows oscillatory deformation and swinging motion, but the amplitudes of oscillation and deformation slowly decrease over time. Eventually the vesicle aligns with the flow direction after about three oscillations. This form of transient dynamics toward tank-treading motion is similar to the relaxation dynamics of a vesicle close to the border between the tank-treading and transition zone observed

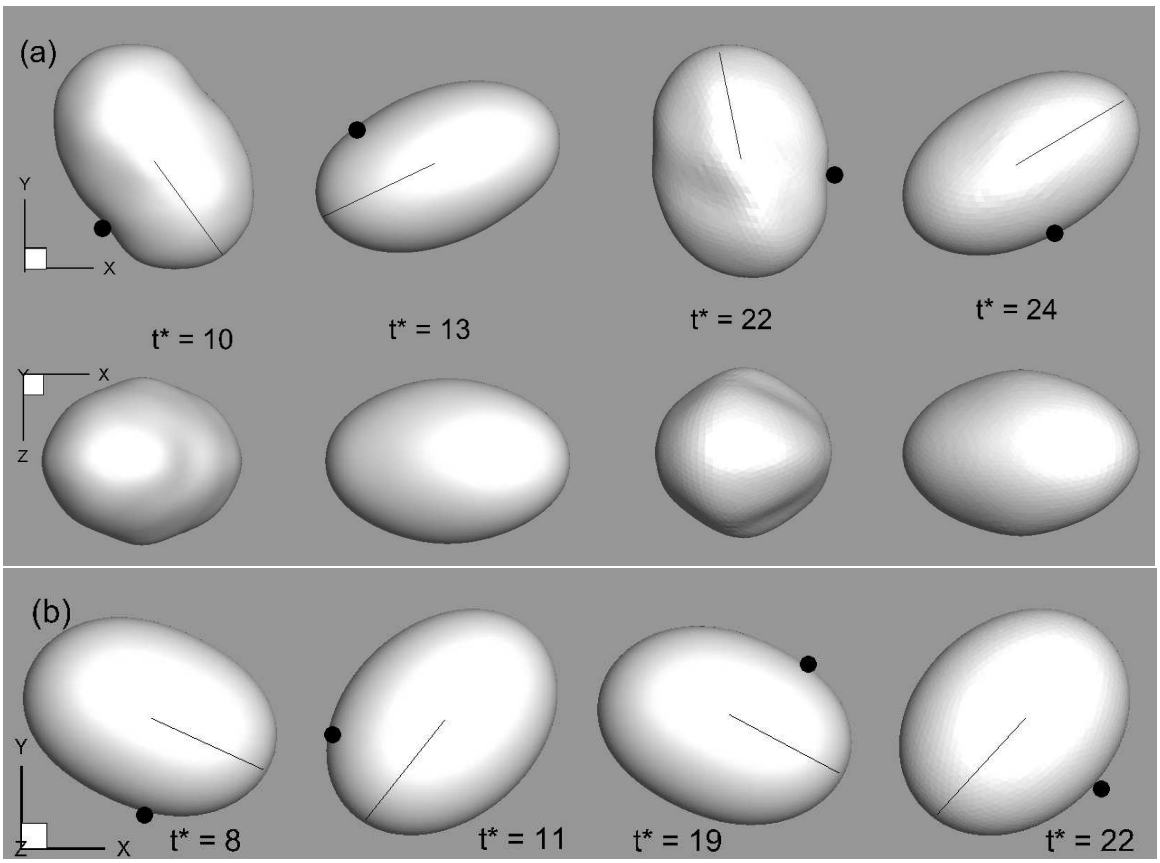

Figure 3.13: Snapshots of tumbling vesicles: (a) $\Delta = 0.44, \lambda = 12, \chi = 50$ which shows that concavity can appear in the tumbling motion at higher χ values. Here both views in the shear plane (x-y) and along the velocity gradient direction (x-z plane) are shown. (b) $\Delta = 0.44, \lambda = 12, \chi = 1$ which shows a smooth elliptical shape at lower χ values. Only the shear plane view is shown here.

by Biben *et al.* [24]. Zhao & Shaqfeh [29] have also shown that the decay of the most unstable mode of the stable tank-treading solution is the source of this behavior. The second type of the transient dynamics occurs upon increasing λ, and is shown in Fig. 5.13(b) for $\lambda = 10$ and $\chi = 5$. Here the vesicle tumbles initially, and then gradually relaxes to the final swinging dynamics at around $t^* \approx 80$. We also studied the effect of the shear rate on the transient dynamics by keeping the same viscosity ratio, and found that higher shear rates will delay the relaxation to the final mode by several more cycles. Note that higher shear rates will reduce the flow time scale, which in turn will prolong the relaxation.

3.3.3 Phase diagram

The phase diagrams from our numerical simulations for two values of $\Delta = 0.44$ and 1.2 in the $(\chi - \lambda)$ plane are presented in Fig. 3.15(a) and (b), respectively. Based on the dynamics described above, three regions are identified in the phase diagrams: (i) Tank-treading, (ii) Transition, and (iii) Tumbling. The general nature of the diagrams is similar to that predicted by the experiments and the theoretical models: For small values of χ, the transition occurs directly as TT $\longrightarrow$ TU with increasing λ, and for $\chi \gtrsim 1$, the vacillating-breathing or the trembling modes appear. We find that the vacillating-breathing mode appears near the lower bound of the transition region, and the trembling-like dynamics occurs near the upper bound. The lower and the upper bounds are independent of χ for large values. The qualitative nature of the phase diagrams is similar for $\Delta = 0.44$ and 1.2, except that the transition boundaries shifted downward for the latter.

Certain differences exist in comparison to the experiments and the theoretical

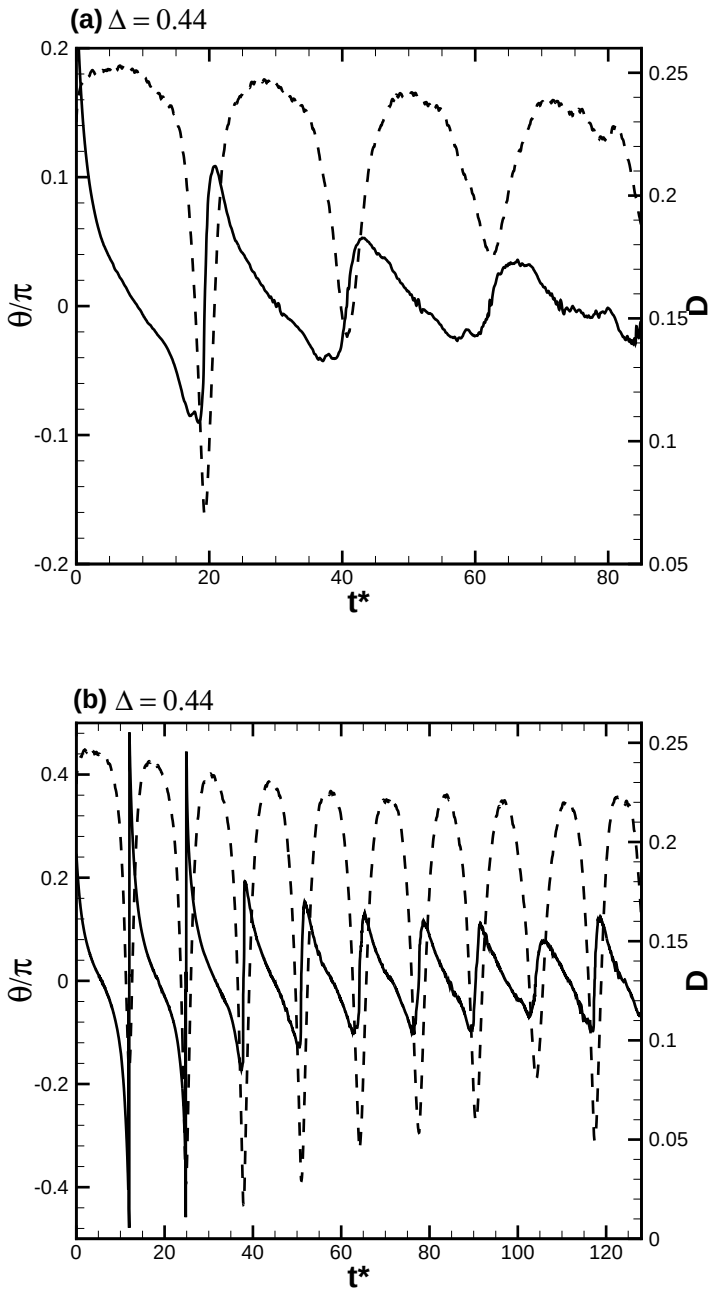

Figure 3.14: Transient dynamics observed for vesicles in the transition zone. Time evolution of θ and D are shown. (a) $\Delta = 0.44$, $\lambda = 8, \chi = 10$. Here the dynamics changes from swinging to tank-treading. (b) $\Delta = 0.44$, $\lambda = 10, \chi = 5$. Here the dynamics changes from tumbling to swinging.

models. First, the width of the transition zone obtained from our simulations is higher than that predicted by the theoretical models of KFM, DBPVM, and LTV. From our phase diagram for $\Delta = 0.44$, the range of λ for the transition zone appears to be 7.5 to 10, corresponding to the lower and upper bounds, respectively. On the contrary, the KFM model predicts 5.92 to 6.7, the DBPVM modes predicts 5.97 to 6.65, and the LTV model predicts 5.87 to 6.33 (see Table 1 in Zabusky *et al.* [28]), giving a much narrower transition band even for such a relatively low value of Δ. It should be noted, as in the figure, the bold lines are for visual guide only, as one would need more simulations to improve the prediction of the transition borders. Moreover, in the transition zone marked as (ii) in the figure, there are two types of the transient dynamics: in one the vesicle relaxes from a swinging to a tank-treading motion, and in another it relaxes from a tumbling to swinging motion. We identify these two types of transient motion in the figure. We also include the neutral curve calculated by Zhao & Shaqfeh [29] for $\Delta = 0.44$. The swinging-to-tank-treading region falls below the stability boundary, and hence, there is an overall agreement between the two works.

Second, the phase diagrams reported in the experiments by Deschamps *et al.* [6], and Zabusky *et al.* [28] are plotted in $(S - \Lambda)$ plane. The range of the trembling band from their phase diagram is $\Lambda \sim 1.5$ to 2.25. Note that these two bounds appear to be independent of Δ values within the margin of uncertainty in the experimental data suggesting a self-similar behavior in the two-parameter space. When we try to scale our data in the two-parameter space, we find that the results are not independent of Δ. In other words, the lower and upper bounds of Λ are functions of Δ. Specifically, we find that the lower and upper bounds are $\Lambda \approx 1.75$ and 2.24 for $\Delta = 0.44$, and 2.4 and

2.88 for $\Delta = 1.2$. Thus, the transition band shifts upward with increasing Δ. Hence, we do not find the self-similar behavior in the two-parameter space, unlike found by the LTV model and in the experimental analysis of Zabusky *et al.* [28]. However, the plot by Zabusky *et al.* appears to suggest a transition band width of ~ 0.75 which is higher than our value. This discrepancy could arise due to the presence of the thermal noise in the experiments, as well as the experimental uncertainty.

Third, Farutin *et al.* [23] in their recent analytical work, and Biben *et al.* [24] in their recent boundary integral simulations have shown that the inclusion of the fourth-order harmonics in vesicle shape widens the transition band upon increasing χ. Their analytical and numerical predictions for the transition band are close to our results. On the contrary, the transition band found in our simulations does not show such widening effect for the range of χ up to 50 considered. Further, similar to the KFM model, we observe that the transition band in the $(\chi - \lambda)$ plane becomes narrower as Δ increases.

3.4 Conclusion

In this chapter, the main objectives were to elucidate the parametric dependence and the self-similarity of the vesicle dynamics, quantification of vesicle deformation, and the analysis of shape dynamics in the trembling mode. In general we find an agreement with the notion set forth in Zabusky *et al.* [28] that the applicability of the perturbative results is limited despite some general agreement with the direct numerical simulations, and experiments. Here we find that many of the deviations between the perturbative results and the simulation results occur even in the absence of thermal noise.

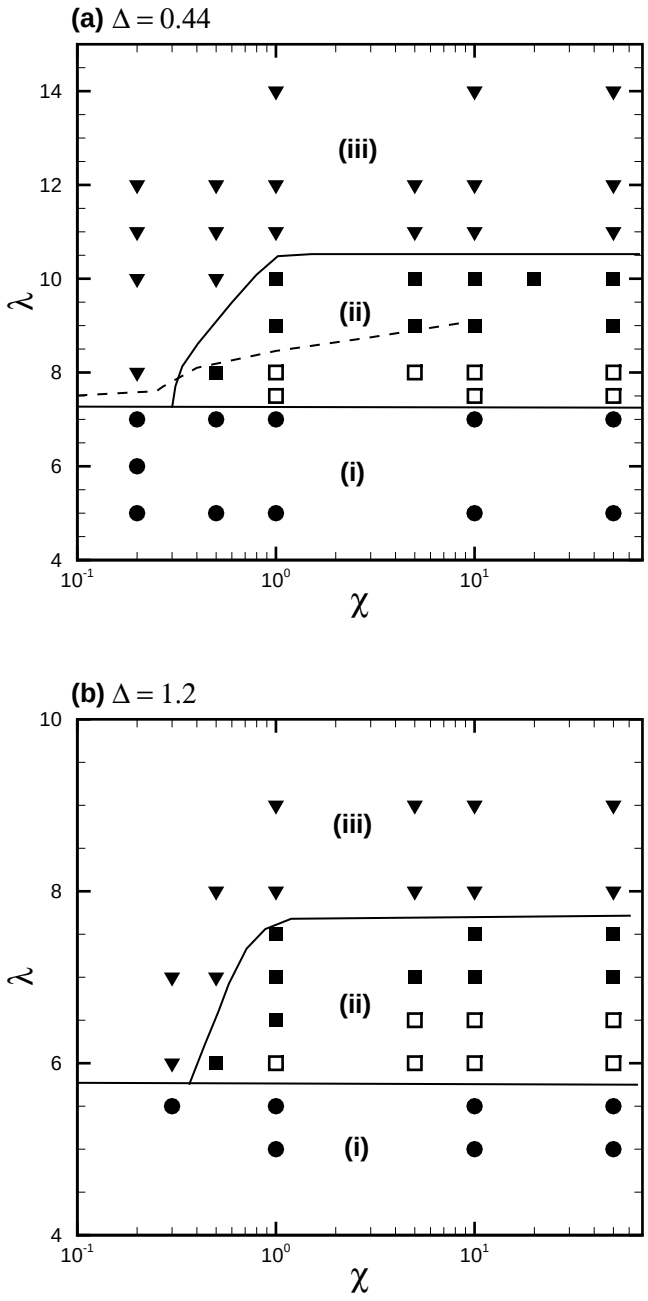

Figure 3.15: Phase diagram for the vesicle dynamics in linear shear flow for: (a) $\Delta = 0.44$; (b) $\Delta = 1.2$. (i) Tank-treading zone •; (ii) Transition zone ■: initially tumbling motion relax to swinging dynamics, and □: initially swinging dynamics relax to tank-treading motion along the flow direction; (iii) Tumbling zone ▼. Also shown in (a) the stability boundary between tank-treading and tumbling/transition dynamics evaluated by Zhao & Shaqfeh [29] from the linear stability analysis (- - -). Bold lines are guide for the eyes.

The major findings of this study are as follows:

(i) We do not observe a self-similar behavior of the vesicle dynamics in the two-parameter phase space proposed by the LTV model, and suggested by Zabusky *et al.* [28] in their analysis of the experimental data. Rather, we find that the phase boundaries depend on the excess area even when plotted in the two-parameter space. In other words, the dynamics is governed by three controlling parameters, namely, Δ, λ and χ, as in the models of DBPVM, and KFM.

(ii) The linear scaling of the TT angle using Λ is valid only for $\Lambda < 1$. The breakdown of the scaling at higher Λ occurs even in the absence of thermal noise.

(iii) We show that in the transition regime, both the vacillating-breathing-like motion characterized by a smooth elliptical shape, and the trembling-like motion characterized by highly deformed shape are possible. For the trembling-like motion, the shape is highly three-dimensional with concavities and lobes, and the vesicle deforms more in the vorticity direction than in the shear plane. This result underscores the importance of three-dimensionality in vesicle dynamics. A Fourier spectral analysis of the vesicle shape shows the presence of the odd harmonics and higher-order modes beyond fourth order.

(iv) Our estimation of the critical viscosity ratio λ_c is in excellent agreement with the experimental observation of $\lambda_c \sim \Delta^{0.24\pm0.02}$ by Kantsler & Steinberg [16]. The computed tank-treading angles are also in very good agreement with the experimental measurements within the margin of uncertainty. Similar to the experimental findings, the numerical TT angles deviate significantly from the theoretical results at large values of Δ. Despite the absence of thermal noise in the simulations, the slow decay of the TT angles found here agreed very well with the experimental observation.

(v) Similar to the DBPVM, KFM and LTV models, we find an explicit dependence of the tank-treading angle on χ for small values, but saturation at higher values. However, contrary to the models, χ-dependence is observed to increase with increasing λ.

(vi) In agreement with Seifert's prediction [19], and experimental measurements by Kantsler & Steinberg [15], we find that vesicle deformation saturates with increasing χ. Quantitatively, we find that Seifert's prediction of $D = \sqrt{15\Delta/32\pi}$ for nearly-spherical vesicles as $\chi \to \infty$ agreed very well with the numerical results in the range $\Delta < 1$.

Chapter 4

Dynamics of a Red Blood Cell in Linear Shear Flow

4.1 Introduction

In this chapter, we study the complex fluid/structure interaction problem for a red blood cell as membrane-bound soft matter. It is observed that over a wide range of controlling parameters, the red blood cell dynamics is much more complex than the well-known tank-treading, tumbling and swinging motion, and characterized by extreme variation of the cell shape. For such convoluted shapes, it is often difficult to clearly establish whether the cell is swinging or tumbling. The effect of such complex shape dynamics on the tank-treading-to-tumbling transition is illustrated by phase diagrams, which appear to be richer than those of vesicles.

We choose the red blood cell as our model system due to its highly non-spherical resting shape and large surface area-to-volume ratio. There are several differences between the real physiological blood flow and the flow conditions considered here. First, the computational geometry considered here replicates a linear shear flow bounded between two parallel plates which is very different from an *in vivo* system. Second, we are considering isolated red blood cells in dilute suspension, while the real blood is a highly dense suspension. Third, the parametric range considered in the present study

is much wider than that typically encountered in physiological flows. The computational geometry and the range of parameters chosen here are consistent with those in previous *in vitro* experiments, where individual red blood cell dynamics was studied in dilute suspension in linear shear flow, and over a similar range of viscosity ratio that was well below the physiological value [10, 12, 95]. The viscosity ratio considered is $\approx 0.21 - 0.45$ in Abkarian *et al.* [12], $0.09 - 0.78$ in Fischer [10], and about 0.05 in Watanabe *et al.* [95] (assuming the cell interior viscosity 10 cP at room temperature). Previous computational studies also considered red blood cell motion in dilute suspension and at viscosity ratio of 1, which is also below the physiological value (e.g., Sui *et al.* [41]).

The capillary number Ca is varied from 0.01 to 1, and the viscosity ratio λ is varied from 0.01 to 5. Three values of $E_b^* = 0.002, 0.01$, and 0.05 are considered to study the effect of bending stiffness. The range of experimental shear rates considered is often two orders of magnitude. The physiological value of the viscosity ratio is close to 5; however, it varies over two orders of magnitude in experiments.

The tank-treading frequency ν as it appears in equation (1.2), depends on the cell shape, shear rate, and viscosity ratio. An accurate measurement of tank-treading frequency is of paramount importance as it can be used to refine the mathematical models for the erythrocyte membrane [8,12]. It can also serve as an indicator for many pathological disorders, such as, sickle cell disease, malignant malaria, and diabetes mellitus in which the erythrocytes lose their deformability due to altered internal fluid viscosity and membrane properties. Several experimental studies in the past have been devoted to measuring the tank-treading frequency. There exists, however, a significant discrepancy among the experimental data regarding the dependence of

tank-treading frequency on the shear rate and viscosity ratio. Fischer *et al.* [9] and Tran-Son-Tay *et al.* [8] found a linear dependence of ν on $\dot{\gamma}$. In contrast, Fischer [10] recently found a weak power-law dependence on $\dot{\gamma}$ with an exponent ranging between 0.85 and 0.95. With regard to the dependence on λ, Fischer *et al.* [9] found that $\nu/\dot{\gamma}$ was independent of the suspending medium viscosity (μ_o), whereas Tran-Son-Tay *et al.* [8] found that $\nu/\dot{\gamma}$ increased with increasing μ_o. Fischer [10] found that $\nu/\dot{\gamma}$ increased with increasing μ_o, but with a reduced slope that was less than half of that reported by Tran-Son-Tay *et al.* [8]. In addition to the dynamics and phase diagrams, a comprehensive analysis of RBC's tank-treading frequency will be presented in this chapter. The effect of membrane viscosity on the tank-treading frequency will also be discussed briefly.

4.2 Dynamics

Red blood cell dynamics is always characterized by simultaneous shape and angular oscillations. When the shape oscillation is large, it is often difficult to clearly establish whether the cell is swinging or tumbling. Hence, first we present the results for which a large variation in cell shape is not observed over an oscillation period, so that a clear tank-treading, swinging or tumbling can be identified. Fig. 4.1(a) shows a tank-treading motion that is observed at a high capillary number. A significant departure from the biconcave resting shape is observed: The biconcave dimples are completely absent; rather the cell assumes a *biconvex* shape. A periodic shape and angular oscillation is present, although the variation of the cell shape over one oscillation cycle is not significant. The biconvex shape is observed throughout the oscillation cycle.

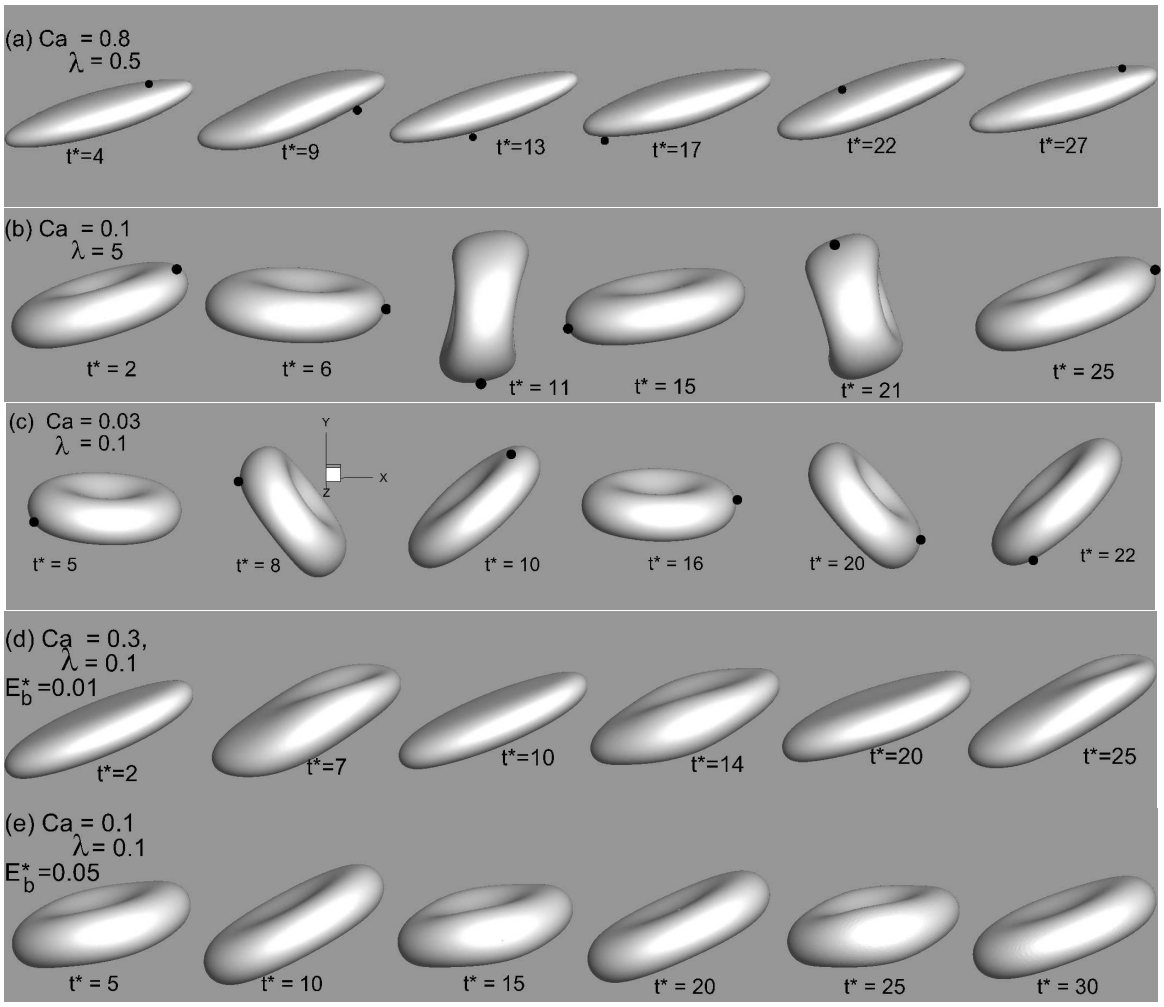

Figure 4.1: Dynamics of red blood cells with small variation of cell shape over one oscillation cycle: (a) Tank-treading with *biconvex* shape (TT/BX) ($Ca = 0.8$, $\lambda = 0.5$, $E_b^* = 0.01$), (b) tumbling (TU) at high viscosity ratio ($Ca = 0.1$, $\lambda = 5$, $E_b^* = 0.01$); (c) tumbling (TU) at low shear rate ($Ca = 0.03$, $\lambda = 0.1$, $E_b^* = 0.01$); (d) swinging (SW/TT) ($Ca = 0.3$, $\lambda = 0.1$, $E_b^* = 0.01$); (e) swinging (SW/TT) ($Ca = 0.1$, $\lambda = 0.1$, $E_b^* = 0.05$). Increasing bending rigidity causes increased angular oscillation as evident in (d)–(e). Membrane tank-tread is shown by tracking a marker point on the cell surface. For all figures, the initial location of the marker point is the same.

A tumbling motion at a high viscosity ratio is shown in Fig. 4.1(b). The marker point on the cell surface shows no significant relative displacement from its initial position. Departure from the initial biconcave shape is found to be small, and the variation of cell shape over one tumbling cycle is also small. A tumbling motion is also observed if the capillary number is reduced as shown in Fig. 4.1(c). It is noteworthy that in the simulations of red blood cells and capsules without bending resistance, the membrane wrinkling that is indicative of buckling has been reported earlier for low capillary numbers [47, 80]. In the present simulation, the membrane wrinkling is absent due to the inclusion of bending resistance during the length of the simulations.

The swinging motion is considered in Figs. 4.1(d)–(e) where the effect of the bending rigidity is also illustrated. The major axis of the cell oscillates about a mean angle while it is constrained within the extensional quadrant of the flow. For moderate values of E_b^* (e.g., 0.01), the swinging motion is accompanied with a relatively small amount of shape variation. In this case, weak biconcave dimples repeatedly emerge and disappear. The concavity is most prominent when the major axis of the cell is closest to the extensional axis of the flow, and completely absent when the major axis is closest to the flow direction. When E_b^* is reduced to 0.002, the amplitude of angular oscillation decreases further (not shown). In contrast, when E_b^* is increased to 0.05 (Fig. 4.1(e)), the amplitude of angular oscillation increases significantly, and the departure from the initial biconcave shape is small. The membrane tank-treading co-exists with the swinging. We identify such dynamics as swinging/tank-treading (SW/TT). A qualitative similarity can be noted between the experimental snapshots of swinging cells as observed by Abkarian *et al.* [12], and our results in Fig. 4.1(e), which is for higher bending rigidity.

Simulations have been conducted over a wide range of viscosity ratio typically considered in experiments. It appears that over this range, the dynamics of the cell is much more complex than the well-known tank-treading, tumbling and swinging motions. In particular, the results presented in Fig. 4.1 show only a small shape variation over the oscillation period. However, over a wide range of parameters, the simulations reveal complex shape dynamics of the red blood cells that are described below.

First we illustrate the breathing dynamics observed for $E_b^* = 0.01$ and 0.002 in Fig. 4.2. The sequence reveals one type of breathing motion in which the RBC nearly aligns with the flow direction so that the average inclination angle is zero, while it performs a periodic shape deformation. The shape deformation is characterized by the membrane folding towards the interior of the cell and forming two concave cusp-like dimples at the two ends. The foldings repeatedly emerge (e.g., at $t^* = 20$ and 40 in Fig. 4.2(a)) and disappear (e.g., at $t^* = 10$ and 25 in Fig. 4.2(a)). Note that this dynamics cannot simply be called a swinging dynamics: As the snapshots suggest, no significant angular oscillation is observed in these cases. Instead, a large variation in the cell shape occurs within an oscillation cycle in the form of repeated folding and recovery. To the best of our knowledge, this type of cell deformation (inward cusps at two ends) and dynamics has not been reported in the past. Following the vesicle literature, we call this dynamics as *breathing* at zero inclination (BR). Evolution of a marker point attached to the membrane is shown in the figure. It cannot be concluded if the marker point makes a continuous tank-tread for such dynamics. Most likely, the marker point oscillates with very little net displacement. The phase angle of a marker point relative to the major axis inclination angle is often used in the literature

to identify swinging or tumbling dynamics. However, due to the complex shape of the cell, the phase angle cannot be accurately evaluated for this dynamics.

A second type of breathing dynamics is illustrated in Fig. 4.3 which co-exists with a large swinging motion. In this case, the breathing motion is characterized by the periodic emergence and absence of crater-like biconcave dimples that are significantly deeper than those of a resting cell, and become most severe when the cell is aligned with the flow direction. Note that on time-average, the cell remains aligned in the extensional quadrant, unlike the BR cases in Figs. 4.2 Such a folded shape co-existing with the swinging motion has not been reported in the past. Here we identify such dynamics as *breathing with swinging* (BR/SW). For this dynamics, evolution of the marker point as shown in the figure suggests a continuous membrane tank-tread.

Fig. 4.4 shows the third type of breathing motion co-existing with a weak tumbling motion (identified as BR/TU); in this case the RBC undergoes a significant amount of shape oscillation which, as above, is characterized by the periodic emergence and absence of large crater-like biconcave dimples. The evolution of the marker point suggests that membrane tank-treading is absent. However, due to the formation of the complex cell shape, a clear tumbling motion cannot be established.

Another novel breathing dynamics is observed at reduced bending rigidity ($E_b^* = 0.002$) and is shown in Fig. 4.5. This is characterized by the repeated emergence and absence of *four* crater-like concave dimples. Such a quad-concave shape has not been reported in the past. At $E_b^* = 0.002$, the quad-concave shape is observed in all BR and BR/SW cases simulated, but not during tank-treading (TT/BX, SW/TT) or tumbling (TU) dynamics.

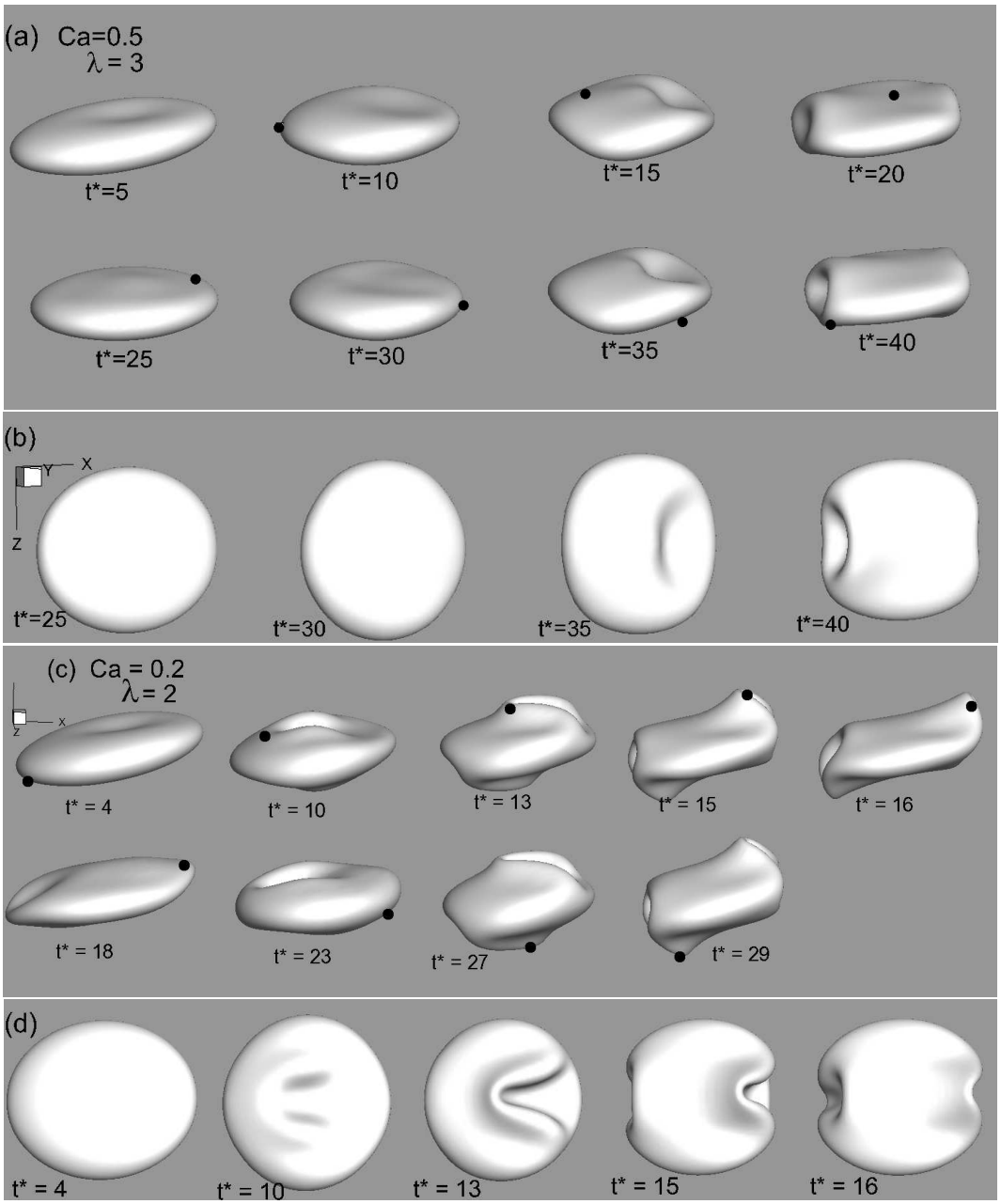

Figure 4.2: Breathing dynamics (BR) of RBC at zero inclination. (a) $Ca = 0.5$, $\lambda = 3$, $E_b^* = 0.01$. (b) shows the plan view. (c) $Ca = 0.2$, $\lambda = 2$, $E_b^* = 0.002$. (d) shows the plan view. RBC undergoes large shape variation over one oscillation cycle characterized by repeated emergence of inward membrane folding at the two ends (at $t^* = 20$ and 40). Very small amount of swinging is observed, and the cell remains nearly aligned with the flow direction.

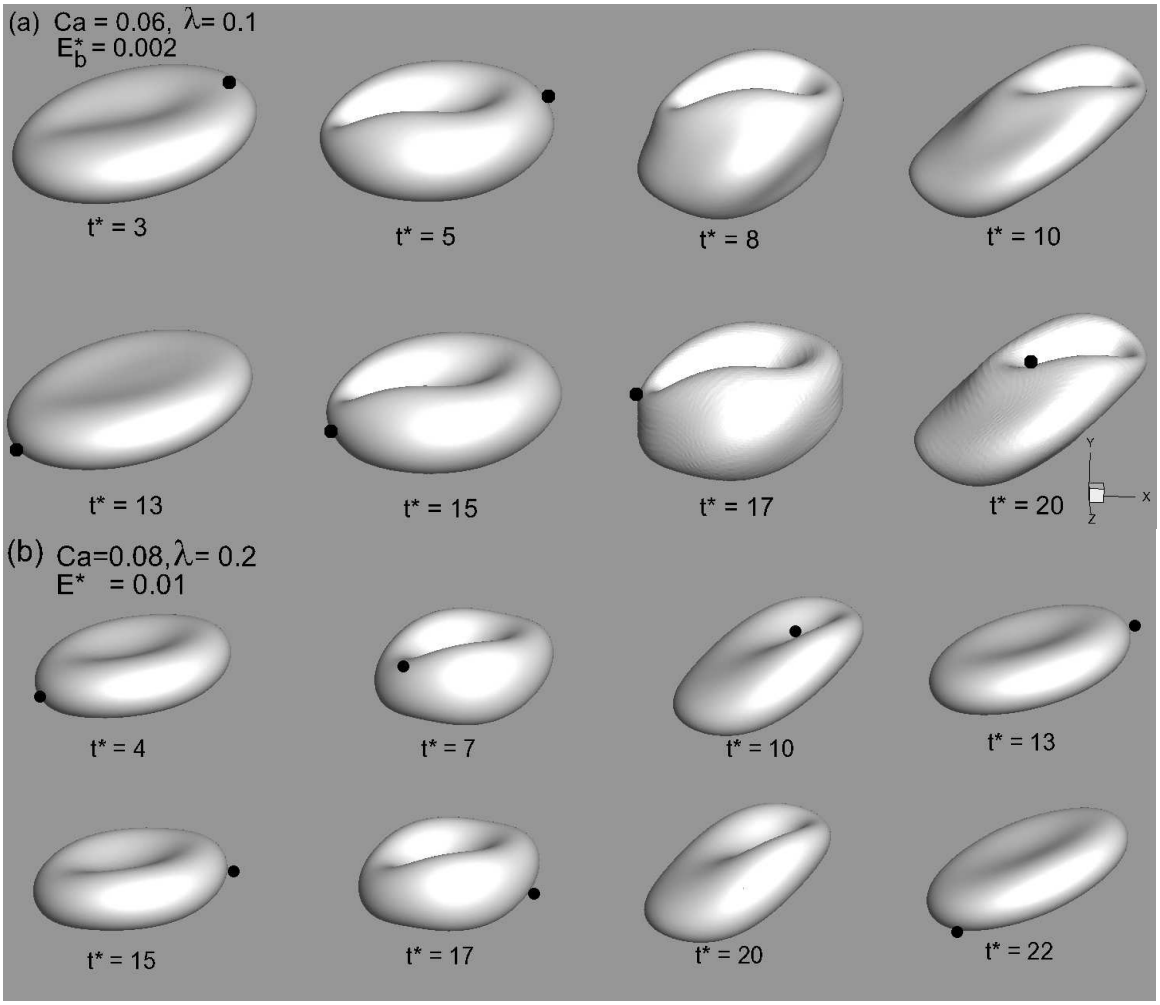

Figure 4.3: Breathing with swinging (BR/SW): (a) $Ca = 0.06$, $\lambda = 0.1$, $E_b^* = 0.002$; (b) $Ca = 0.08$, $\lambda = 0.2$, $E_b^* = 0.01$. The dynamics is characterized by RBC swinging coupled with complex shape deformation during which deep crater-like dimples periodically emerge (e.g, at $t^* = 8$ and 17 in (a), and at $t^* = 7$ and 17 in (b)) and disappear (e.g., at $t^* = 3$ and 13 in (a), and at $t^* = 13$ and 22 in (b)).

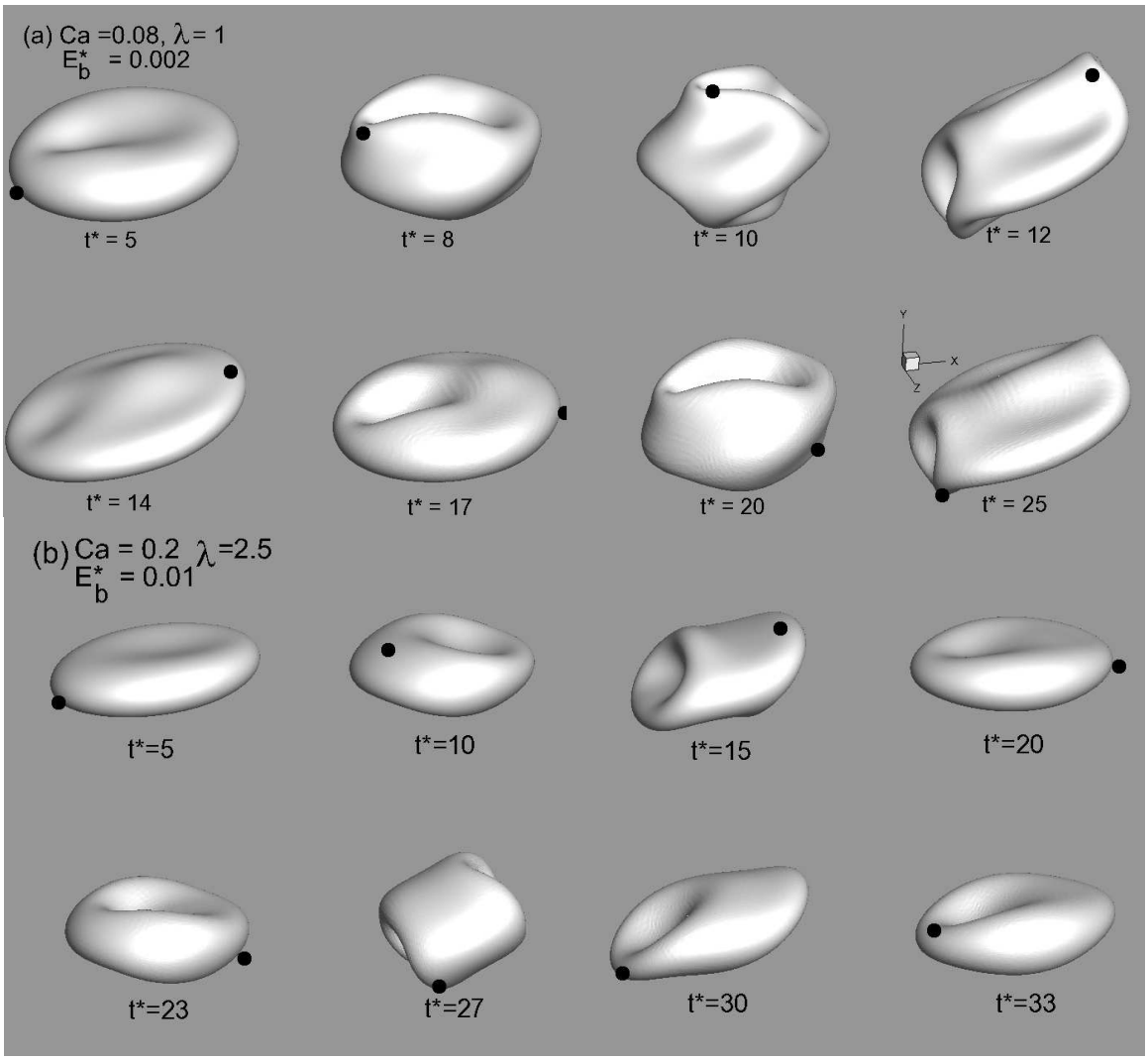

Figure 4.4: Breathing with tumbling (BR/TU): (a) $Ca = 0.08$, $\lambda = 1$, $E_b^* = 0.002$; (b) $Ca = 0.2$, $\lambda = 2.5$, $E_b^* = 0.01$. The dynamics is characterized by complex shape deformation that masks a clear tumbling motion.

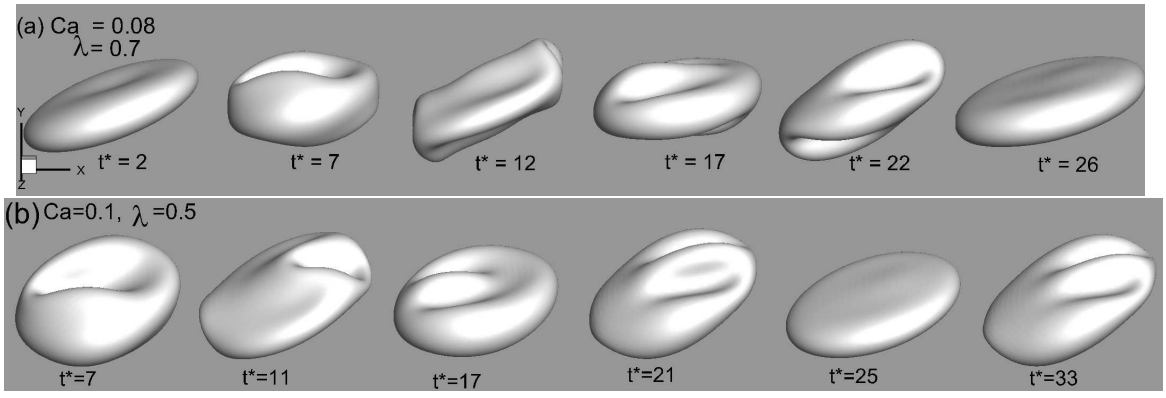

Figure 4.5: Breathing motion with quad-concave dimples occurring at reduced bending rigidity (a) $Ca = 0.08$, $\lambda = 0.7$, $E_b^* = 0.002$; (b) $Ca = 0.1$, $\lambda = 0.5$, $E_b^* = 0.002$.

4.3 Phase Diagram

Fig. 4.6 shows the phase diagram for RBC dynamics in $Ca-\lambda$ plane for $E_b^* = 0.01$. A stationary tank-treading motion is never observed even though a wide range of Ca and λ is considered. Instead, the cell dynamics is always characterized by simultaneous shape and angular oscillations. After carefully analyzing each case, we identify six distinct regimes: (i) breathing at zero inclination (BR), which occurs over a relatively small region $2 \leq \lambda \leq 3$, and $0.3 < Ca < 0.5$, and at the border between SW/TT and BR/TU; (ii) breathing with swinging (BR/SW), which occurs below $\lambda \approx 2$, and when Ca is in the range 0.06 to 0.3; (iii) breathing with tumbling (BR/TU), which occurs above $\lambda \approx 1$ and $Ca \approx 0.06$; (iv) swinging with tank-treading (SW/TT), which occurs for $0.3 < Ca < 0.6$, and below $\lambda \approx 2$; (v) tank-treading *biconvex* (TT/BX), which occurs at high capillary numbers only (above $Ca \approx 0.7$), and below $\lambda \approx 4$; (vi) tumbling (TU), which occurs either at very low shear rates, or at high viscosity ratio.

The phase diagram in Fig. 4.6 shows two pathways to transition from tank-treading to tumbling, namely, by increasing λ, or by decreasing Ca. Several new features of transition are found in the phase plots. Most notably, for $\lambda < 1$ approximately, the transition process is completely independent of λ; it depends on Ca only. This is a remarkable departure from the KS theory for non-deformable cells, which predicts that the transition is dependent on λ only for any shear rate. In this regime, the transition occurs progressively as TT/BX $\longrightarrow$ SW/TT $\longrightarrow$ BR/SW $\longrightarrow$ TU with decreasing Ca. We identify three critical capillary numbers as $Ca_c^{\mathrm{TT/BX \rightarrow SW/TT}} \approx 0.61$, $Ca_c^{\mathrm{SW/TT \rightarrow BR/SW}} \approx 0.26$, and $Ca_c^{\mathrm{BR/SW \rightarrow TU}} \approx 0.055$, which are independent of λ in the range $\lambda < 1$. For $\lambda > 1$, the transition process depends on both λ and Ca, and, the critical Ca rapidly increases with increasing λ. Above $\lambda \approx 4$, the TT/BX,

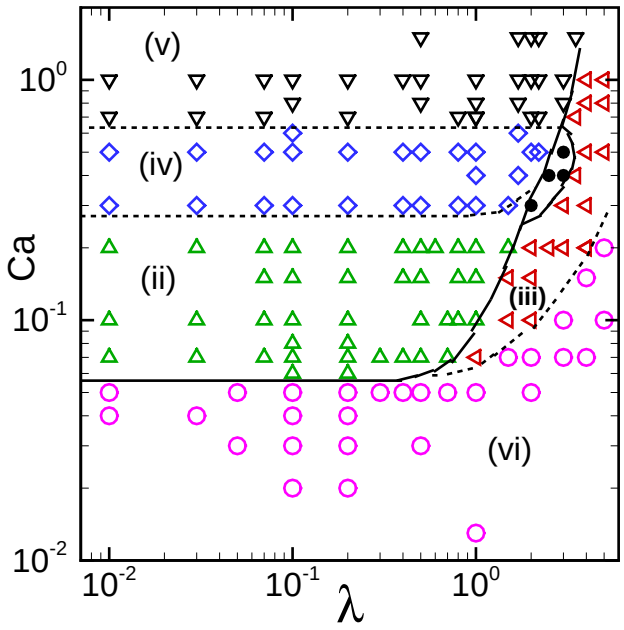

Figure 4.6: Phase diagram for RBC dynamics at $E_b^* = 0.01$. (i) Breathing at zero inclination (BR), •; (ii) breathing with swinging (BR/SW), △; (iii) breathing with tumbling (BR/TU), ◁; (iv) swinging with tank-treading (SW/TT), ◇; (v) tank-treading biconvex (TT/BX), ▽; (vi) tumbling (TU), ◯.

SW/TT and BR/SW motions are not observed even at high shear rates, and the transition occurs as BR/TU $\longrightarrow$ TU with decreasing Ca. The breathing motion occurs in the vicinity of the critical capillary number and viscosity ratio.

The effect of the bending rigidity on the phase diagram is considered in Fig. 4.7. As evident here, at a reduced bending rigidity ($E_b^* = 0.002$), the breathing motion at zero inclination (BR) occurs over a wider range of λ and Ca in comparison to that at $E_b^* = 0.01$. Also, the BR/SW mode occurs over a wider range of Ca, and the BR/TU mode can appear at lower values of λ. In contrast, the SW/TT mode occurs over a much narrower range of Ca. Below $\lambda \approx 0.2$, the transition process is independent of λ; rather it depends on Ca only, and occurs at a capillary number less than that obtained for $E_b^* = 0.01$. The critical capillary numbers for $E_b^* = 0.002$ are: $Ca_c^{\mathrm{TT/BX \rightarrow SW/TT}} \approx 0.35$, $Ca_c^{\mathrm{SW/TT \rightarrow BR/SW}} \approx 0.21$, and $Ca_c^{\mathrm{BR/SW \rightarrow TU}} \approx 0.035$. At

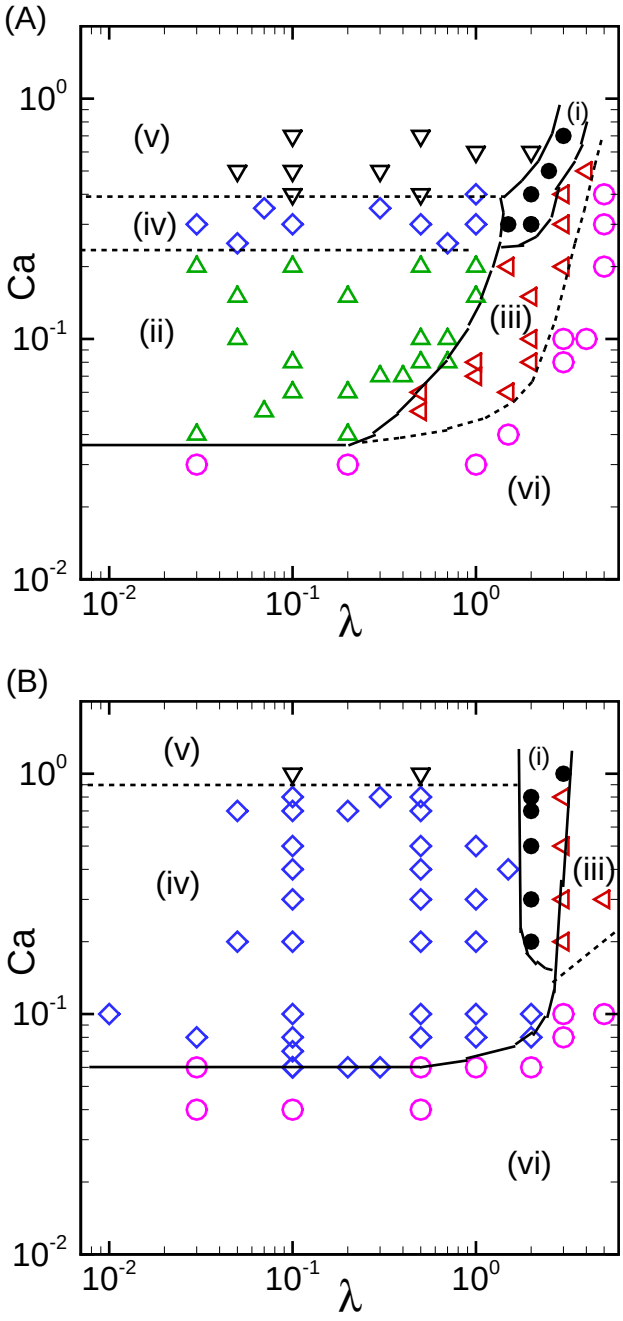

Figure 4.7: Phase diagram for RBC dynamics at $E_b^* = 0.002$ (A), and 0.05 (B). (i) Breathing at zero inclination (BR), •; (ii) breathing with swinging (BR/SW), △; (iii) breathing with tumbling (BR/TU), ◁; (iv) swinging with tank-treading (SW/TT), ◇; (v) tank-treading biconvex (TT/BX), ▽; (vi) tumbling (TU), ◯.

higher bending rigidity ($E_b^* = 0.05$), the BR/SW dynamics is absent, and SW/TT dynamics occurs over a wider range of Ca. The BR/TU dynamics occurs at higher values of λ. For $\lambda < 1$, the transition is dependent on Ca only, and it occurs as TT/BX $\longrightarrow$ SW/TT $\longrightarrow$ TU. Hence, only two critical capillary number are noted for $E_b^* = 0.05$: $Ca_c^{\mathrm{TT/BX \rightarrow SW/TT}} \approx 0.9$, and $Ca_c^{\mathrm{SW/TT \rightarrow TU}} \approx 0.06$.

4.4 Shape and Curvature Oscillation

The breathing motion can be identified quantitatively by a sudden increase in RBC shape oscillation during tank-treading-to-tumbling transition. This is shown in Fig. 4.8 by plotting the amplitudes of longitudinal and transverse shape oscillations $\Delta L = (L_{\max} - L_{\min})/2$ and $\Delta Z = (Z_{\max} - Z_{\min})/2$, respectively, as functions of Ca for different values of λ, where L is the end-to-end RBC length in the shear plane passing through the cell centroid, and Z is the end-to-end length along the z-axis. Note that due to the highly deformed and dynamically changing shape of the cells, it is often difficult to label the major and minor axes specifically in the BR, BR/SW and BR/TU regions. Hence, only a subset of the data is presented for which ΔL and ΔZ can be clearly estimated. The scatter in the figure appears also for the same reason. As Fig. 4.8 shows, ΔL and ΔZ are maximum in the TT/BX regime, and they decrease with decreasing Ca from TT/BX to SW/TT regimes reaching a minimum at the end of the SW/TT regime. With further decrease in Ca, BR/SW regime starts, and ΔL and ΔZ reverse their trends and increase with decreasing Ca due to large shape deformation and repeated emergence and absence of the dimples in the breathing motion. With further decrease in Ca, TU regime starts, and ΔL and ΔZ again reverse their trends, and decrease with decreasing Ca due to reduced deformation in the TU mode.

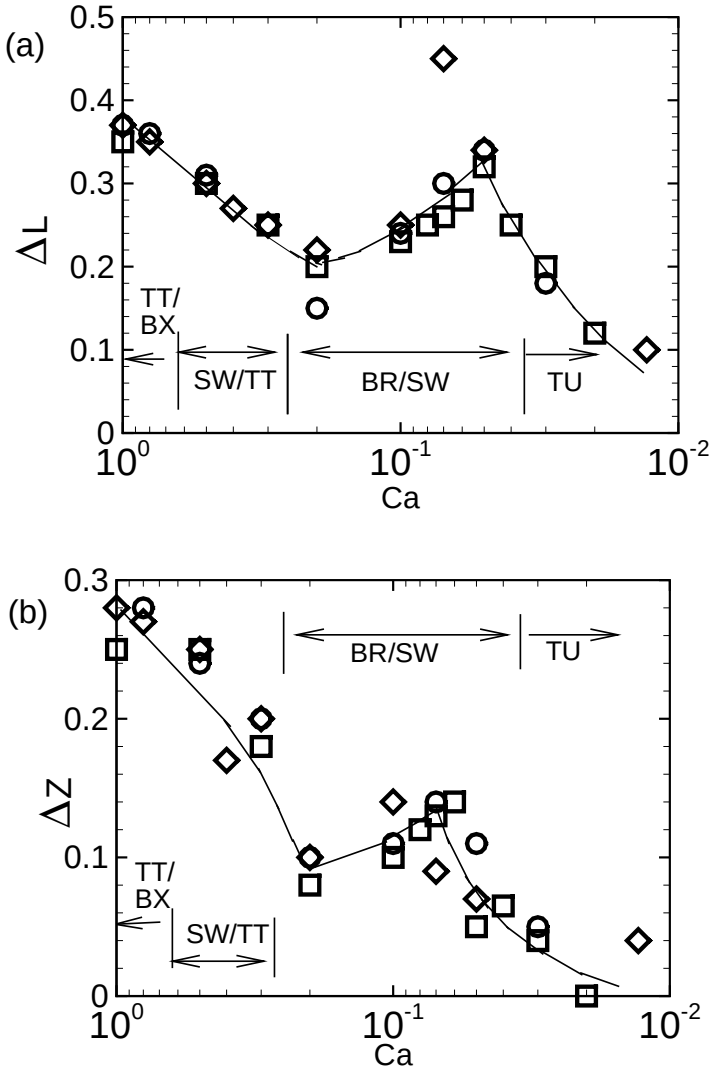

Figure 4.8: Amplitudes of longitudinal and transverse shape oscillations (a) ΔL and (b) ΔZ as functions of Ca for various values of λ (0.2, $\square$; 0.5, $\bigcirc$; 1, $\diamond$). On the horizontal axis, Ca decreases from left to right. The curve through the data points is drawn for visual assistance ($E_b^* = 0.01$).

Due to the periodic emergence and absence of the dimples in the breathing motion, a further quantification of these modes is done by computing three quantities related to the cell curvature as follows: (i) a *contour* curvature $\overline{\kappa}(t) = \int_C [\kappa(\mathbf{x}, t) - \kappa_0(\mathbf{x})]\, \mathrm{d}l/C$, defined as the time-dependent but spatially-averaged mean curvature κ less the resting curvature κ_0 of the RBC contour C in the shear plane passing through the centroid, (ii) the curvature amplitude $\Delta\overline{\kappa} = \overline{\kappa}_{\max} - \overline{\kappa}_{\min}$, and, (iii) a time-averaged curvature $\overline{\overline{\kappa}} = \int_T \overline{\kappa}(t)\mathrm{d}t/T$, where T is the period of swinging or tumbling. Fig. 4.9(a) shows $\overline{\kappa}(t)$ obtained for different RBC dynamics. In the TT/BX regime, the mean curvature $\kappa(\mathbf{x}, t)$ remains mostly positive due to the absence of the dimples; hence, $\overline{\kappa}(t) > 0$. In the TT/SW regime, $\overline{\kappa}(t)$ becomes periodically positive and negative with small amplitude due to the repeated emergence and absence of weakly biconcave dimples. In the breathing with swinging motion (BR/SW), $\overline{\kappa}(t)$ shows very large oscillations, and importantly, remains negative due to the emergence of the crater-like concave dimples. In the TU mode, $\overline{\kappa}(t)$ shows much less oscillation. Figs. 4.9(b) and (c) show the time-averaged curvature $\overline{\overline{\kappa}}$ and amplitude $\Delta\overline{\kappa}$, respectively. Clearly, the transition from TT/BX to SW/TT mode is characterized by $\overline{\overline{\kappa}}$ changing from positive to negative values, and higher slope of $\Delta\overline{\kappa}$. In the breathing mode, both $\overline{\overline{\kappa}}$ and $\Delta\overline{\kappa}$ reach their maximums. With further decrease in Ca, the trends reverse, and $\overline{\overline{\kappa}}$ and $\Delta\overline{\kappa}$ rapidly approach zero as the transition to TU motion occurs.

It is also noteworthy that we do not observe any intermittent motion of the cells (swinging interrupted by tumbling, and vice versa) over the entire parametric range, unlike that reported in experiments [12] and predicted by the reduced-order models [11].

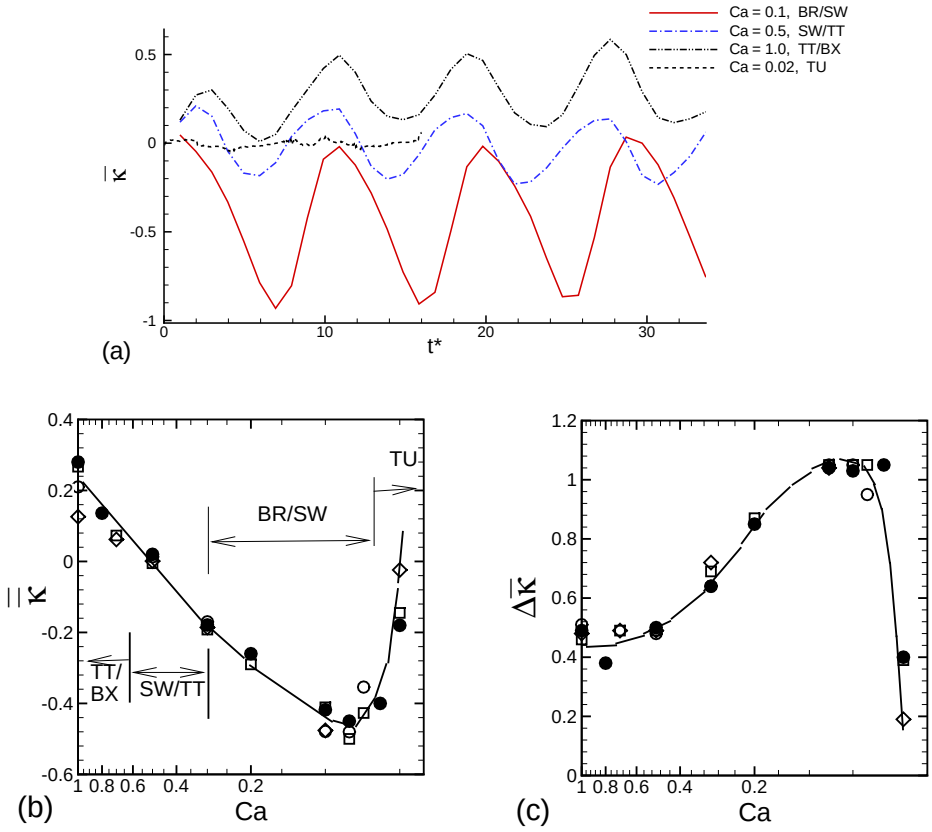

Figure 4.9: (a) Contour-averaged curvature $\overline{\kappa}(t)$ for various RBC dynamics at $\lambda = 0.1$; (b) time-averaged curvature $\overline{\overline{\kappa}}$; and (c) curvature amplitude $\Delta\overline{\kappa}$ as functions of Ca for different values of λ (0.1, •; 0.2, □; 0.5, ◯; 1, ◇). Here $E_b^* = 0.01$.

4.5 Analysis of Tank-treading Frequency

The effect of the viscosity ratio λ on the tank-treading frequency ν^* of the red blood cell is shown in Fig. 4.10. Here, ν^* is defined as $\nu^* = 4\pi/\dot{\gamma}T_{tt}$, where T_{tt} is the tank-treading period of a membrane point extracted from our simulations. Note that ν^* is the frequency $(\dot{\gamma}T_{tt})^{-1}$ normalized by the frequency of rotation for a rigid sphere $(4\pi)^{-1}$. The frequency is strongly dependent on λ and it decreases with increasing viscosity ratio. The numerical results are in qualitative agreement with the experimental results of Abkarian *et al.* [12], Fischer [10] and Tran-Son-Tay *et al.* [8], who found a decreasing trend of ν^* with increasing λ, but not with the experimental results of Fischer *et al.* [9] who found no significant λ-dependence. A wide range of Ca values are considered in Fig. 4.10, and the numerical data nearly collapse for all Ca. Thus the frequency is strongly dependent on λ, but weakly dependent on Ca.

In Fig. 4.10, the numerical data are compared with the experimental results of Abkarian *et al.* [12], Fischer [10] and Tran-Son-Tay *et al.* [8]. The numerical results are in the same range as that of Abkarian *et al.* [12] experimental data, but are significantly higher than those reported by Fischer [10] and Tran-Son-Tay *et al.* [8]. Comparison of the numerical results with different theoretical models for shape-preserving capsules is also presented in Fig. 4.10. First, we consider the Keller & Skalak (KS) model [7] for which the tank-treading frequency (ν^*_{ks}) is obtained by solving the system of equations (1.1-1.2) for an oblate spheroid having the same volume ($94.1\mu\text{m}^3$) and surface area ($134.1\mu\text{m}^2$) of the red blood cell. As evident from Fig. 4.10, the KS model shows the similar trend as of the numerical results over the entire range of λ. Second, we consider the Skotheim & Secomb [11] model, hereafter referred to as the SS model. The SS model was developed within the framework of the KS model [7]

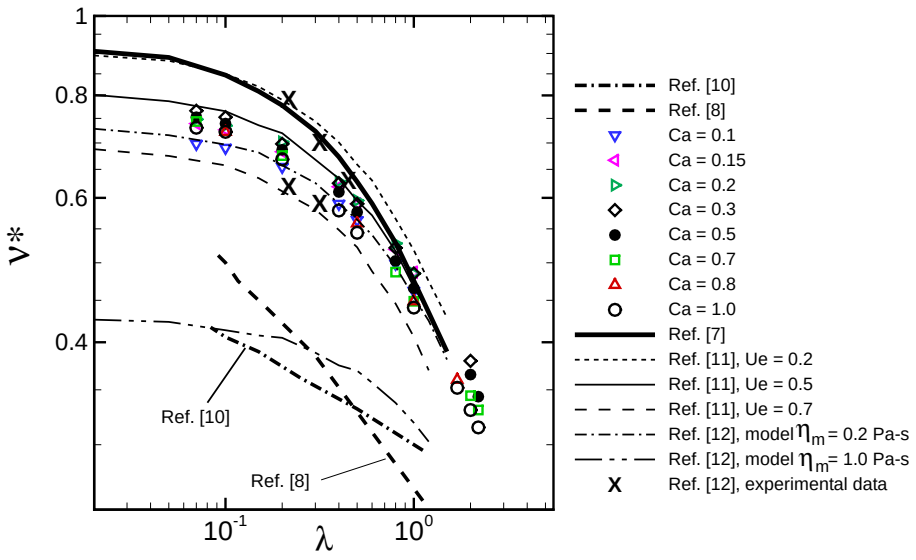

Figure 4.10: Tank-treading frequencies of red blood cells as a function of viscosity ratio. Numerical data are shown for different values of Ca, and compared with the experimental results [8,10,12], and theoretical models [7,11,12]. The lines representing the experimental results of [10] and [8] are linear regressions given in [10] (Fig. 5 in [10]). Some selected data from [12] are shown.

with an additional term $\dot{\gamma}U_e[f_3/(f_2 - \lambda f_1)]\sin 2\phi$ on the right hand side of equation (1.2) to model the time-dependency of the membrane elastic energy. Here, U_e is proportional to Ca^{-1}, and ϕ is the phase angle of a membrane point. The tank-treading frequency (ν^*_{ss}) obtained from the SS model as a function of λ for three different values of U_e is plotted in Fig. 4.10. We note that the tank-treading frequency is an inverse linear function of λ in both KS and SS models. We observe that the numerical results agree very well with the theories in the entire range of viscosity ratios. This agreement is worth noting because unlike the simulations, the theoretical models do not consider cell deformation. This agreement is due to the reduced area dilatation considered in the red blood cell simulations.

Next we consider Abkarian *et al.* [12] model, hereafter referred to as the AB model. This model retained all elements of the SS model, and included the effect of

the membrane viscosity by modifying equation (1.2) based on the consideration of the energy dissipation in the membrane. The results from the AB model are shown by considering two values of the membrane viscosity, $\eta_m = 0.2$ and 1.0 (Pa-s). As evident from Fig. 4.10, the AB model shows the similar trend as that of the numerical results, and quantitatively agrees well with the numerical data as well as Abkarian *et al.* [12] experimental data for a low value of the membrane viscosity $\eta_m = 0.2$ (Pa-s). However, for the higher membrane viscosity $\eta_m = 1$ (Pa-s), the AB model prediction drops significantly, and lies in the range of Fischer [10] and Tran-Son-Tay *et al.* [8] experimental results.

The above analysis suggests that differences in experimental conditions might have caused a difference in the erythrocyte membrane viscosity in the three experimental works [8, 10, 12].

It may be noted, as observed in Abkarian *et al.* [12], that in order to obtain a tank-treading solution from the AB model, the value of the membrane shear elasticity E_s needs to be one to three orders of magnitude lower than the typical measured values (e.g., 6×10^{-6} (N/m) as used here). Thus the comparison with the AB model should be taken with caution. Further, Abkarian *et al.* [12] considered a range $\dot{\gamma} < 10$ s^{-1}, while Fischer [10] considered a wider range of $\dot{\gamma} < 300$ s^{-1}. Additionally, the experimental results were presented as functions of the suspending medium viscosity μ_o. To plot these data as functions of λ as in Fig. 4.10, we assume a constant internal medium viscosity $\lambda\mu_o = 10$ (mPa-s).

The effect of the capillary number on the red blood cell tank-treading frequency is shown in Fig. 4.11. Experiments by Fischer [10] and Tran-Soy-Tay *et al.* [8] suggested that the dimensional frequency ν is a linear (or, nearly linear) function of the shear

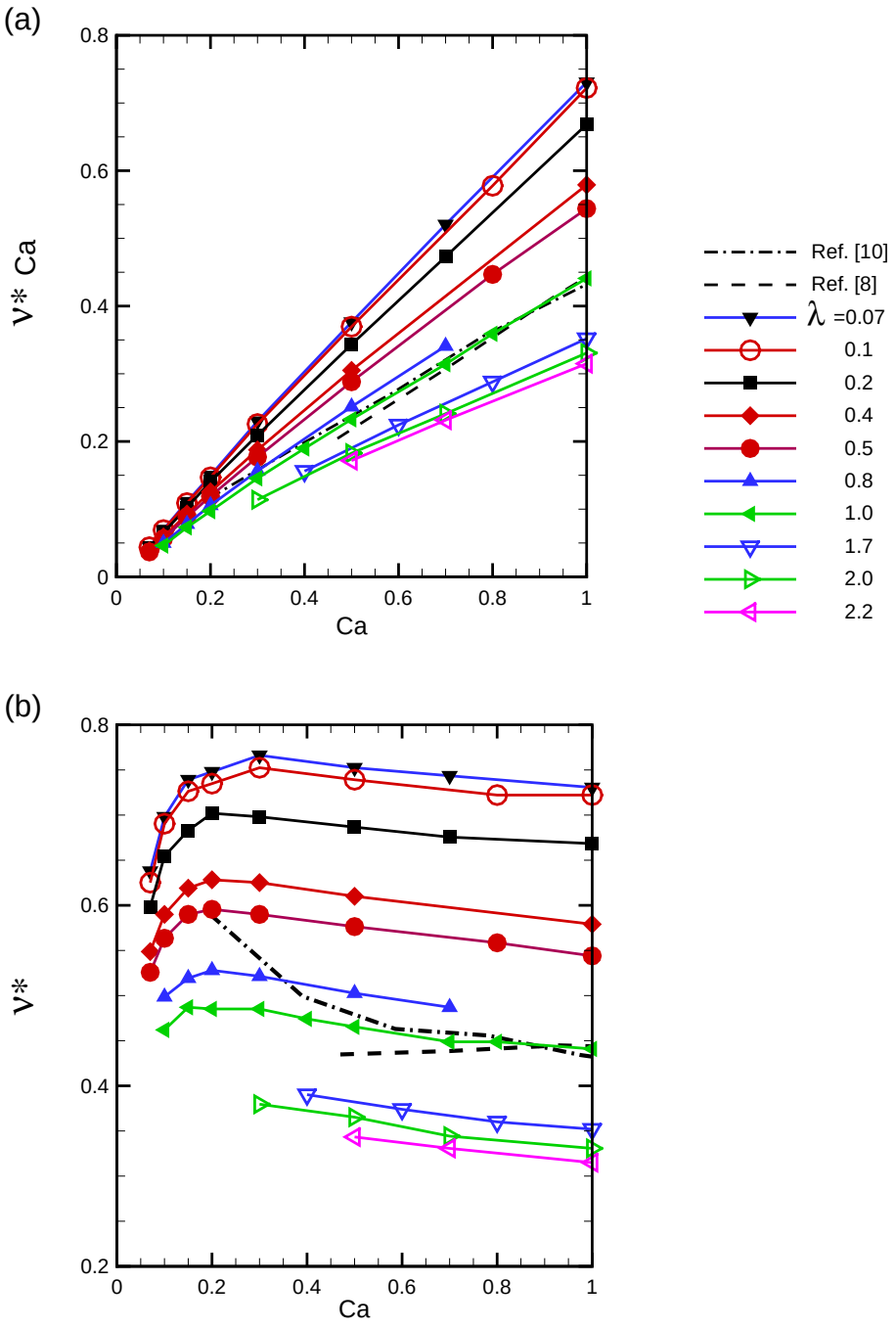

Figure 4.11: Tank-treading frequencies of red blood cells as a function of capillary number. Numerical data are shown for different values of λ from 0.07 to 2.2 using symbols and solid lines, and compared with the experimental results of [10] (–·–·– for $\lambda = 0.2$), and [8] (– – – for $\lambda = 0.17$). (a) Shows the product $\nu^* Ca$, whereas (b) shows ν^*.

rate. Hence, in Fig. 4.11(a), we plot the product $\nu^* Ca$ as a function of Ca. A linear dependence is evident here, in agreement with the experimental findings. The range of $\nu^* Ca$ obtained in the simulations also matches well with the experimental data as shown.

Some interesting behavior is found when the same data is replotted in Fig. 4.11(b) as ν^* versus Ca. For any value of λ, ν^* is almost independent of Ca in the range $Ca > 0.3$. This is due to nearly-inextensible surface of the cell considered in the simulations. Note that in this range, the red blood cell assumes a nearly-convex disk shape as discussed in the context of Fig. 4.1. When $Ca < 0.3$ is considered in Fig. 4.11(b), the tank-treading motion is possible only for low values of λ. In this range, ν^* sharply decreases with decreasing Ca. This anomalous behavior of ν^* has not been reported earlier. We have verified that this trend is not a result of any numerical artifact. This trend is due to the emergence of the breathing dynamics of red blood cells at low values of λ and Ca as described in Fig. 4.3. A significant compression of the cell occurs during such breathing motion preventing it from tumbling, and increasing the time period of swinging.

4.5.1 Effect of membrane viscosity

We present the results regarding the effect of membrane viscosity on the RBC tank-treading frequency in Fig. 4.12. The numerical method used here is based on the Kelvin–Voigt viscoelastic membrane model described in Section 2.3. Several interesting observations can be made here. First, the numerical results show that for a purely elastic membrane the tank-treading frequency varies approximately linearly with Ca. However, we observe that as the membrane viscosity η^* increases from 1 to

10, the power-law dependence of $Ca\nu^*$ on Ca becomes much more pronounced. This power-law trend is in agreement with the experimental results by Fischer [10] shown in Fig. 4.12. Second, we note a significant decrease in tank-treading frequency as η^* increases due to the presence of membrane dissipation. Further, the results show that as λ increases, closer agreement with experimental data for different donors can be achieved at higher η^*. More specifically, for $\lambda = 0.1$ in Fig. 4.12(a), $\eta^* \approx 2$ predicts the experimental data well, whereas for $\lambda = 0.75$ in Fig. 4.12(b), $\eta^* = 5 \sim 10$ gives a better prediction.

As mentioned before, there is a wide range of experimentally measured values of the membrane viscosity. The present numerical results may be used to estimate the value of the membrane viscosity μ_s. Using the definition of $\eta^* = \mu_s/\mu_o a_o$ with $a_o \sim 3\mu$m, and $\mu_o = 109.3$ and 12.9 (mPa-s) [10] for $\lambda \sim 0.1$ and 0.78, respectively, the value of μ_s will be in the range $2 - 6 \times 10^{-7}$ (N.s/m). This value is several factors higher than that estimated by Tran-Soy-Tay *et al.* [8] for the membrane viscosity, and agrees well with the values reported by Chien *et al.* [89] and Hochmuth *et al.* [90].

4.6 Conclusion

In this chapter, we presented three-dimensional numerical simulations of the red blood cell dynamics in shear flow. Numerically stable solutions are obtained over a wide range of parameters for which the cell attains an extremely deformed shape in the form of membrane convolution. It is shown that over a wide range of parameters, the shape dynamics is more complex than the well-known swinging or tumbling dynamics. We term such dynamics as the breathing dynamics due to the extreme variation of the cell shape over one oscillation cycle.

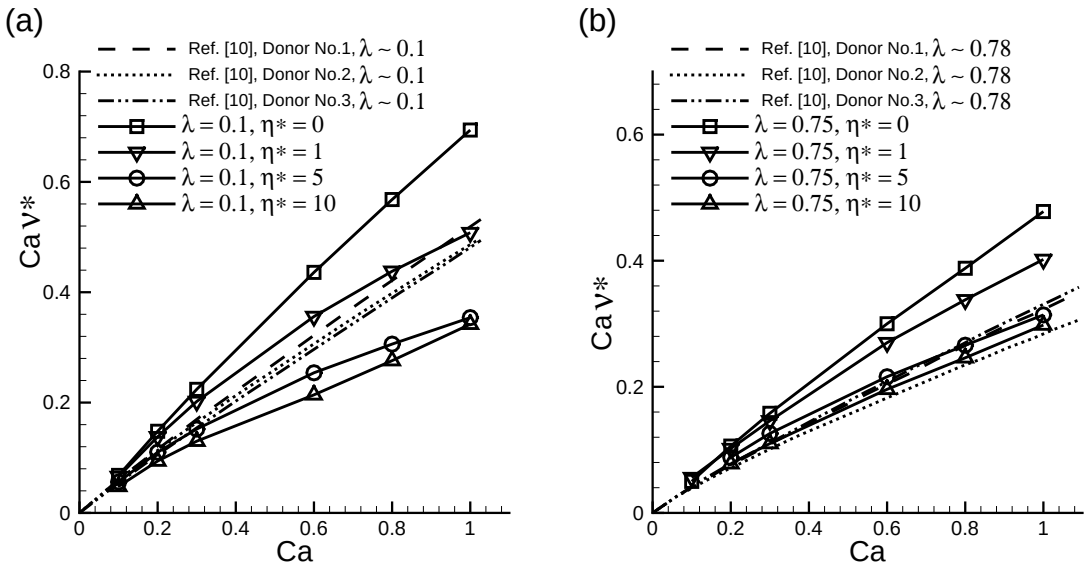

Figure 4.12: Effect of membrane viscosity on the tank-treading frequencies of red blood cells for two values of viscosity ratios: (a) $\lambda = 0.1$, and (b) $\lambda = 0.75$. Numerical data are shown for different values of η^* from 0 to 10 using symbols and solid lines, and compared with the experimental results of [10] for Donor No. 1 ($- - -$); Donor No. 2 ($\cdots$); and Donor No. 3 ($- \cdot\cdot -$).

We identify three types of the breathing motion which were not reported previously. In the first type, the RBC completely aligns with the flow direction with almost no swinging motion, but undergoing large shape variation that is characterized by inward membrane folding and cusp-like biconcave dimples periodically emerging and disappearing at the two ends of the cell. The second type is found to co-exist with a large swinging motion in which deep crater-like biconcave dimples periodically emerge and disappear, and may resemble a wave-like motion traveling along the cell surface. The third type is found to co-exist with a possible tumbling motion and is also characterized by emergence and absence of deep crater-like dimples. In this case, the shape oscillation is so dominant that a clear tumbling motion is not observed. At reduced bending rigidity, a quad-concave shape is found. The breathing dynamics

occurs near the threshold of transition between tank-treading and tumbling, and delays the transition to higher viscosity ratio and lower shear rates. Quantitatively, it is identified by four quantities: the amplitudes of longitudinal and transverse shape oscillation, the time-averaged curvature, and the amplitude of curvature oscillation; all of which show a significant increase during the breathing motion.

We observe both shear rate-induced and viscosity-induced transitions and illustrate them using phase diagrams, which appear to be more complex than those of vesicles. We find that there exists a critical λ, the value of which depends on the bending rigidity, and below which the tank-treading-to-tumbling transition is independent of λ; rather the transition depends on Ca only, and occurs as TT/BX $\longrightarrow$ SW/TT $\longrightarrow$ BR/SW $\longrightarrow$ TU with decreasing Ca. This is a remarkable departure from the classical theory of Keller & Skalak [7], which predicts transition depends on λ only irrespective of shear rate. Above the critical λ, the transition process depends on both λ and Ca. In this range, no swinging motion is found even at high shear rates, and the transition occurs as BR/TU $\longrightarrow$ TU with decreasing Ca. At reduced bending rigidity, the breathing motion occurs over a wider range of λ and Ca, and the transition occurs at lower values of Ca. No intermittent motion is observed for the entire range of parameters.

The complex shape dynamics of the red blood cells observed here has not been reported in previous experiments due to, perhaps, lack of sufficient resolution. The phase diagram and the cell dynamics found here are for isolated cells in dilute suspension in linear shear flow *in vitro*, and not *in vivo*. It appears from our results that for the physiological value of the viscosity ratio, a large-amplitude swinging motion

and breathing motion do not occur; rather, the cells perform either a tumbling motion or a tumbling combined with breathing. For the latter, the shape deformation is significant as observed here.

An analysis of the red blood cell tank-treading frequency was also given in the present chapter. This study is motivated in part by the discrepancy that exists in the literature with regard to the dependence of the tank-treading frequency on shear rate and suspending medium viscosity. For the red blood cells with purely elastic membrane, ν^* exhibits an inverse linear dependence on the viscosity ratio, which agrees well with different theoretical models for shape-preserving cells.

Moreover, the tank-treading frequency ν^* exhibits a non-monotonic trend with respect to the capillary number Ca, and hence, the shear rate. With decreasing Ca, ν^* first increases reaching a maximum, and then decreases sharply before the tank-treading motion ceases. This anomalous behavior of ν^* with respect to Ca has not been reported earlier, and as shown here, is a result of a breathing-like dynamics of the cell, which is characterized by the appearance of a folded shape and deep, crater-like dimples.

Once the membrane viscosity is introduced to the model, we observe a significant decrease in the tank-treading frequency due to the presence of membrane dissipation. Further, the tank-treading frequency tends to have a power-law behavior with respect to Ca under the influence of membrane viscosity similar to what observed by the experiments of Fischer [10].

Chapter 5

Influence of Membrane Viscosity on Capsule Dynamics in Shear Flow

5.1 Introduction

As mentioned in Section 1.5, several theoretical and numerical studies of capsules with purely elastic membrane suggested the presence of membrane buckling [59,75,80,82]. They observed that the capsule buckled at low shear rates with wrinkles forming near the equator similar to the experimental observation of Walter *et al.* [73].

These studies assumed that the capsule membrane is elastic, and hence, did not consider the viscosity of the membrane. Clearly, a comprehensive analysis on the influence of the membrane viscosity on the capsule dynamics in a shear flow is lacking, and is the objective of the present study. Of particular interest is the effect of the membrane viscosity on the buckling of initially spherical capsules. Further, it is well established by now that an initially nonspherical capsule may exhibit an unsteady dynamics that is characterized by a swinging motion or a tumbling motion (see e.g., [11,12,14,42,75]). It is also of interest to understand how the dynamics changes from swinging to tumbling under the influence of the membrane viscosity. Towards that end, we presented a numerical method for capsules with a viscoelastic membrane that follows the Kelvin–Voigt model in Section 2.3. In addition to the membrane shear viscosity and elastic modulus, the model also includes the membrane bending

resistance, surface area dilatation, and internal to external fluid viscosity contrast.

Using the numerical tool, we embark to address a sequence of problems related to the capsule deformation, dynamics, and buckling. First, we present an analysis of the membrane buckling for the initially spherical capsules with the viscoelastic membrane. Then we consider the membrane viscosity effect on the deformation, dynamics and tank-treading frequency. This is followed by an analysis of the membrane viscosity effect on the unsteady dynamics of an initially oblate capsule.

5.2 Spherical Capsules

5.2.1 Membrane stability and buckling

Capsules without bending stiffness and $\lambda = 1$

The membrane viscosity introduces several interesting features in the dynamics and deformation of the capsule, one of them is the onset of buckling. We first present our results for capsules with no bending rigidity, that is, $E_b^* = 0$. As mentioned before, for purely elastic capsules without the bending rigidity and represented by Skalak *et al.* constitutive law with $C = 1$, large compressive stress appears for $Ca \lesssim 0.13$ near the capsule equator suggesting the possibility of buckling [59,80]. For $Ca \gtrsim 0.8$, large compressive stress also occurs, but near the tips, leading to unbounded deformation. In the range $0.13 \lesssim Ca \lesssim 0.8$, Lac *et al.* observed that the stress remained tensile everywhere, suggesting no buckling of the purely elastic capsule in this range. It is of interest to see how the membrane viscosity affects the stability in this range. Note that $E_s = 3G_s$ for $C = 1$; hence, Ca defined in Lac *et al.* [59], which is based on G_s, is 3 times bigger than the one defined in the present work. Figure 5.1(a)-(d)

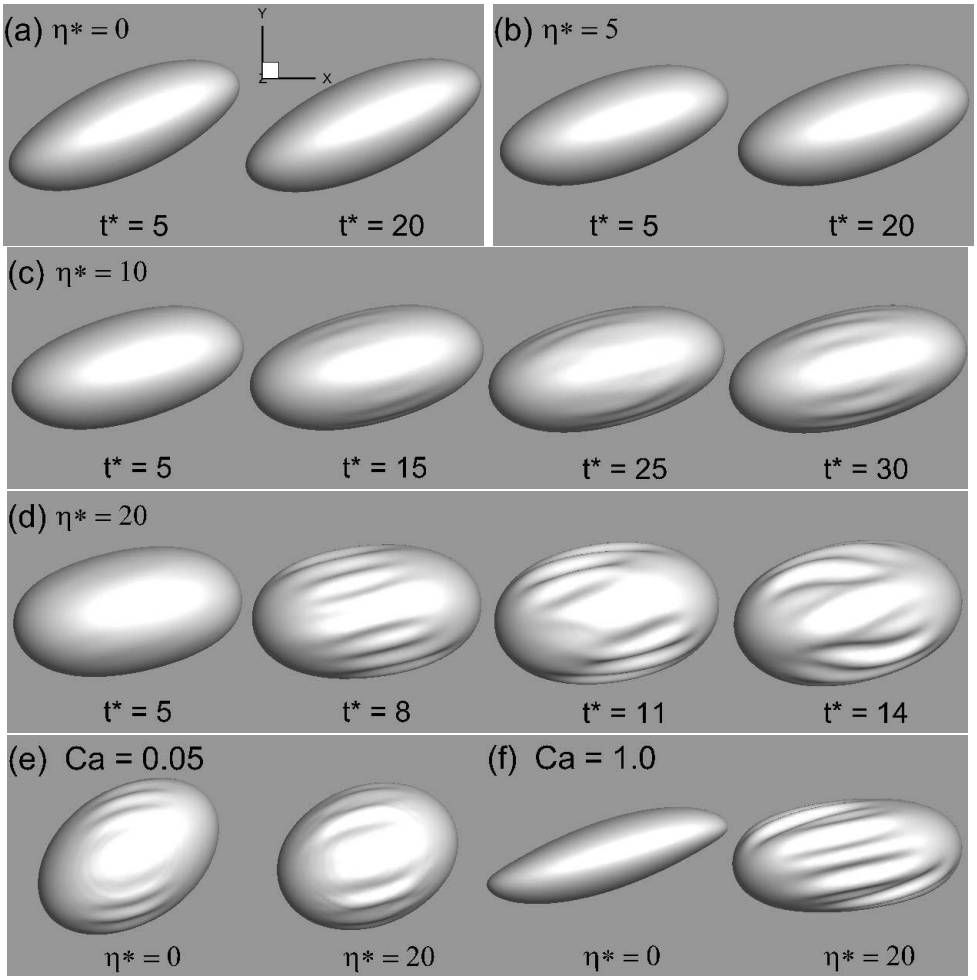

Figure 5.1: Effect of membrane viscosity on the buckling of an initially spherical capsule without bending stiffness. (a) to (d) $Ca = 0.3$, and η^* varies as 0, 5, 10, and 20, respectively. (e) $Ca = 0.05$, and $\eta^* = 0$ and 20. (f) $Ca = 1.0$, and $\eta^* = 0$ and 20. Here $\lambda = 1$ for all.

presents sample results for $Ca = 0.3$ and $\lambda = 1$. Here η^* is varied as 0, 5, 10, and 20 in (a) to (d), respectively. For the purely elastic case, (Fig. 5.1(a), $\eta^* = 0$), there is no sign of wrinkles on the interface, and the shape remains stable. For $\eta^* = 5$ (Fig. 5.1(b)), wrinkles are not visible either, and the capsule shape remains stable, though it will be shown later that compressive stress appears at this value of η^*. When η^* is increased to 10 in Fig. 5.1(c), wrinkles are observed near the capsule equator. We find that these wrinkles exhibit a symmetrical pattern, which is due to the symmetry of the external shear flow. Animations from the simulations show that wrinkles first form near the equatorial rim, and then propagates toward the shear plane in a wave-like motion. Figure 5.1(d) shows that when η^* increases further to 20, wrinkles are more prominent as the number and the depth of the folds increase. We observe that the folds appear near the equator of the capsule surface are similar to the buckling patterns observed in the experiments of Walter *et al.* [73]. However, the folds in our simulations commonly have longer amplitudes and wavelengths than the short-wavelength wrinkles observed in the experimental work by Walter *et al.* [73] and analytical theory by Finken & Seifert [82]. These results show that in the absence of bending rigidity, the membrane viscosity causes buckling in the range of Ca in which capsules with a purely elastic membrane would not show any buckling.

Consider now the range $Ca \lesssim 0.13$ and $Ca \gtrsim 0.8$. Figures 5.1(e) and (f) show the buckling pattern for $Ca = 0.05$ and 1.0, respectively. Here λ is held constant at 1. For each case, we consider two values of $\eta^* = 0$ and 20. As evident, at $Ca = 0.05$, buckling is observed for the pure elastic membrane as well as the viscoelastic membrane with the similar patterns of wrinkles occurring in both cases. At $Ca = 1.0$, the purely elastic case does not show any buckling and the shape remains stable in our

simulations, though pointed tips are formed at the two ends of the capsule. When membrane viscosity is introduced, deep wrinkles develop soon after the simulation starts which eventually lead to a catastrophic shape distortion. These results suggest that at low values of Ca, the buckling occurs primarily due to the elastic instability, and the membrane viscosity has relatively less impact. On the contrary, at higher values of Ca, buckling can occur due to the membrane viscosity.

Membrane buckling has its origin in the evolution of compressive stresses as illustrated by Lac *et al.* [59] and Li & Sarkar [80]. It is of interest to understand how membrane viscosity affects the distribution and magnitude of the compressive stresses. We plot in Fig. 5.2 the contours of the principal viscoelastic stress τ_2 evaluated from the stress tensor in equation (2.42), keeping in mind that the principal stresses τ_1 and τ_2 are scaled by E_s. We have verified that the principal stress τ_1 is always positive and tensile, whereas τ_2 can become negative and hence compressive. First, we will consider $E_b^* = 0$ and $\lambda = 1$. Figs. 5.2(a)-(b) show the stress contours at $Ca = 0.05$, for $\eta^* = 0$ and 20, respectively. For both $\eta^* = 0$ and 20, τ_2 is observed to be negative over the equatorial region where wrinkles appear. Further, the negative maximums of τ_2 for the two cases are found to be close to each other. Hence, the membrane viscosity has relatively less impact at lower range of Ca where buckling is primarily due to the elastic instability. Figs. 5.2(c) and (d) show the stress contours at $Ca = 0.6$ for $\eta^* = 0$ and 5, respectively. For the pure elastic case, τ_2 is positive almost everywhere on the capsule surface except at the tips where it is negative. No buckling, however, occurs despite this compressive stress. When η^* is increased to 5, the region with negative τ_2 is no longer observed at the tips; rather it has moved toward the equatorial rim. Also, the negative maximum of τ_2 has increased as η^* is

increased from 0 to 5. However, no buckling is observed in this case as well. Figs. 5.2(e) and (f) show the time evolution of τ_2 contours for $Ca = 0.6$ and $\eta^* = 10$. First, a continuous band of high compressive stress is observed to span from the equatorial rim towards the tips. The negative maximum of τ_2 has further increased by nearly a factor of three compared to that of the elastic membrane. Over time, the maximum compressive stress moves from the equatorial rim to about 20 degrees away from the tips, where the wrinkles are first formed and then spread toward the equatorial region. Interestingly, for the viscoelastic membrane the stress at the tips remain positive unlike the elastic membrane. Similar τ_2 distribution is observed at higher values of Ca, e.g., $Ca = 1.0$. This analysis suggests that at high values of Ca, introduction of a small amount of membrane viscosity first redistributes the compressive stress from the tips to the equatorial rim. Upon further increase in the membrane viscosity, the compressive stress spreads back from the rim towards the tips. At the tips, however, τ_2 remains positive, and the maximum negative stress develops at some angle away from the tips.

The above results on the onset of wrinkles at $E_b^* = 0$ and $\lambda = 1$ are provided in a parametric phase space in terms of Ca and η^* in Fig. 5.3. As evident, for $\eta^* \lesssim 1$, the onset of buckling is determined by the capillary number, and it happens between 0.1 and 0.2, as in case of a capsule with pure elastic membrane. For $\eta^* \gtrsim 10$, buckling is observed for the entire range of Ca considered here. Interestingly, the value of $\eta^* \sim 10$ is roughly in the same range of experimentally measured values for artificial capsules and red blood cells. It should be mentioned that the phase plot is obtained based on visible appearance of wrinkles on the capsule surface.

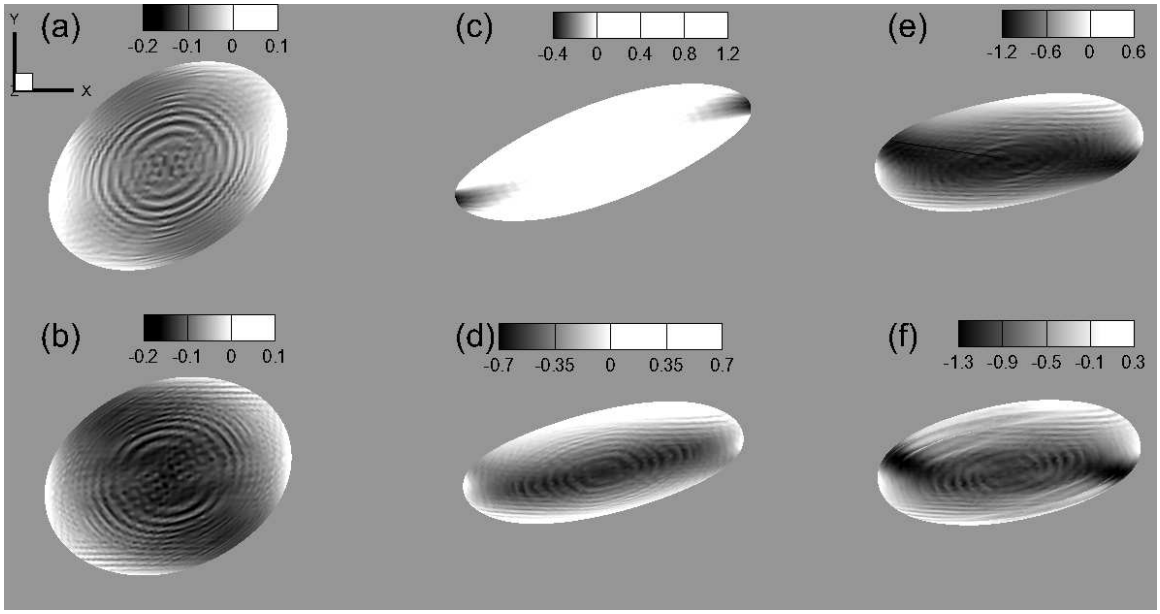

Figure 5.2: Effect of membrane viscosity on the contours of τ_2 for an initially spherical capsule with $E_b^* = 0$ and $\lambda = 1$. In (a) and (b), $Ca = 0.05$ while η^* is varied as 0 and 20. In (c) and (d), $Ca = 0.6$, while η^* is 0 and 5, respectively. In (e) and (f), the time evolution of τ_2 is shown for $Ca = 0.6$ and $\eta^* = 10$ by considering two time instants $t^* = 8$ and 15, respectively.

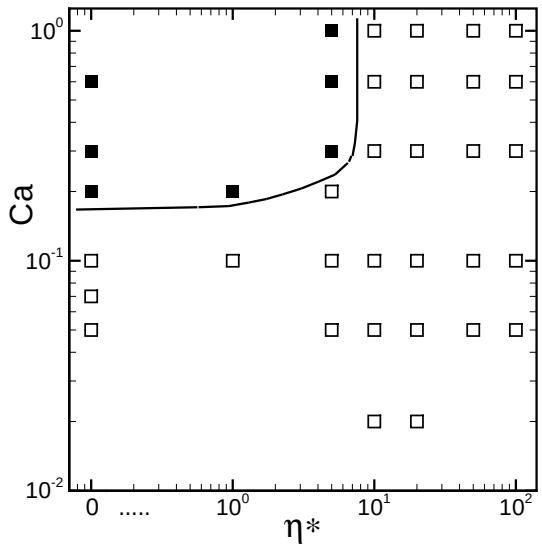

Figure 5.3: Phase space plot showing the onset of wrinkles for capsules with $E_b^* = 0$ and $\lambda = 1$. The filled symbols represent cases where no wrinkles formed, and the open symbols represent those where wrinkles formed.

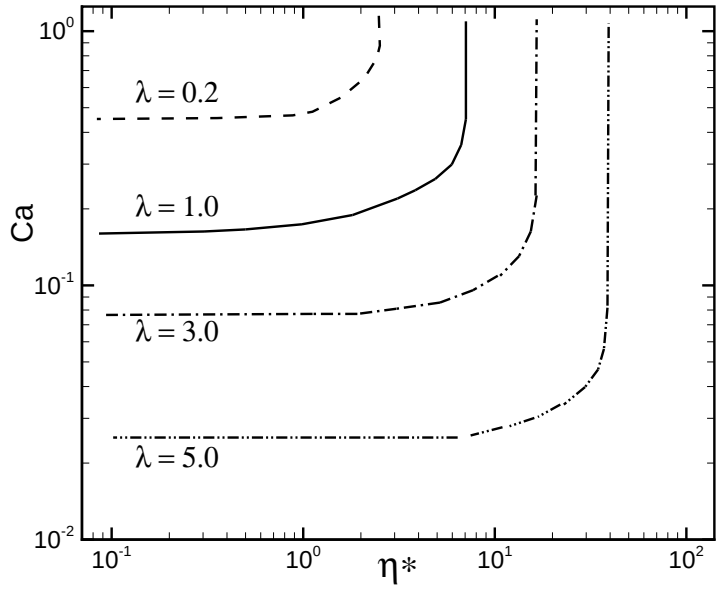

Figure 5.4: Ca vs. η^* phase plot for membrane buckling of the spherical capsules with no membrane bending rigidity ($E_b^* = 0$). The lines separate regions with or without buckling for $\lambda = 0.2$ ($- - -$); $\lambda = 1$ (——); $\lambda = 3$ ($- \cdot -$); and $\lambda = 5$ ($- \cdot\cdot -$). Top left side of each curve is the region without wrinkles, and the bottom right side is the region with wrinkles.

Effect of λ

We now consider the effect of the internal to external fluid viscosity ratio λ. Fig. 5.4 presents the phase diagram in terms of Ca and η^* showing the regions of buckling for four different values of $\lambda = 0.2$, 1, 3, and 5. Here we do not provide the symbols to avoid cluttering of the data. Top left side of each curve is the region without wrinkles, and the bottom right side is the region with visible wrinkles. The overall nature of the curves remains the same for all λ. However, with increasing λ, the region of buckling is observed to decrease. For instance, for $Ca = 1.0$, the wrinkles appear between $\eta^* = 1$ and 5 for $\lambda = 0.2$, but between 20 and 50 for $\lambda = 5.0$.

The stabilizing effect of the viscosity contrast is further illustrated in Fig. 5.5 where we show sample results on capsule shape and τ_2 distribution by varying λ as 0.2, 1.0, and 5.0 while keeping Ca and η^* fixed at 0.6 and 10, respectively. For $\lambda = 0.2$, high

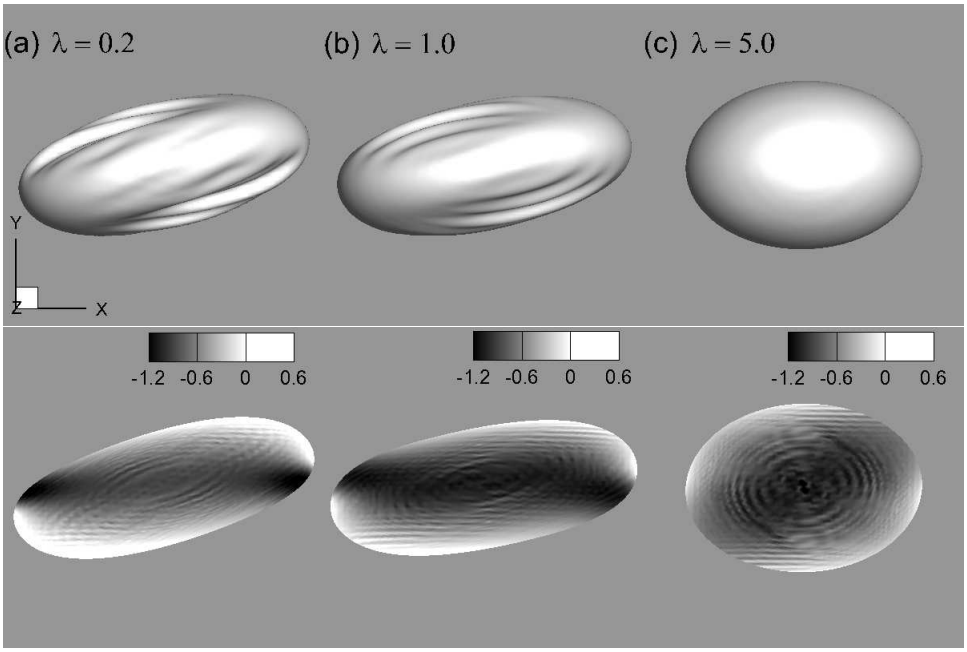

Figure 5.5: Effect of viscosity contrast λ on buckling in the presence of membrane viscosity. Top row shows capsule shapes, and bottom row shows contours of τ_2. Here $Ca = 0.6$ and $\eta^* = 10$ are kept fixed while λ is varied as 0.2, 1.0, and 5.0 in (a), (b) and (c), respectively.

compressive stress is observed at some angle away from the tips spreading towards the rim, which leads to capsule buckling, similar to the case at $\lambda = 1$. The negative maximum of τ_2 for $\lambda = 0.2$ is slightly higher than that for $\lambda = 1$. When λ is increased to 5, the wrinkles on the capsule surface are no longer visible, although the compressive stress of reduced magnitude exists over a large region.

Effect of bending stiffness

Until now we have considered capsules without the bending stiffness of the membrane. Since one of our objectives is to quantify the effect of membrane viscosity on capsule deformation, it is necessary to obtain stable shapes. We consider the membrane bending stiffness to prevent buckling, and thus, obtain stable shapes. Fig. 5.6 shows sample runs to illustrate the effect of bending rigidity on suppressing the buckling

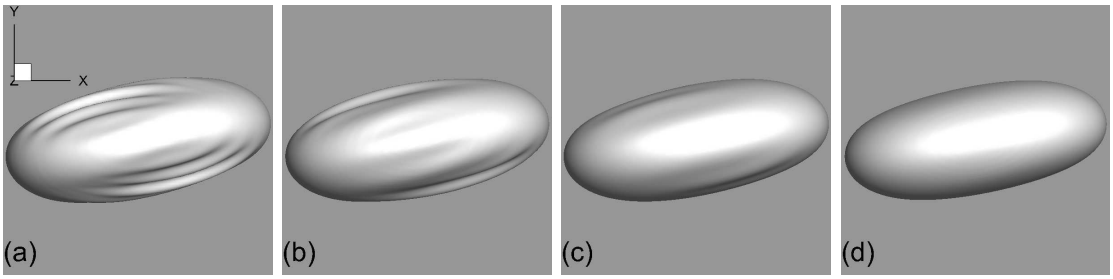

Figure 5.6: Effect of bending stiffness on suppressing buckling. Here $Ca = 0.6, \lambda = 1, \eta^* = 10$, while E_b^* is varied as (a) 0; (b) 0.0005; (c) 0.001; and (d) 0.002.

instability. Here Ca, λ and η^* are kept constant at 0.6, 1, and 10, respectively, while four different runs are considered by varying E_b^* as 0, 0.0005, 0.001, and 0.002. We find that the number of the wrinkles and their amplitudes decrease as E_b^* increases. Eventually, at $E_b^* = 0.002$ no wrinkle is visible. Also interesting to note that while the introduction of the bending stiffness has prevented buckling, the overall deformation and inclination are not significantly changed. For the runs provided in Fig. 5.6, which are at relatively high capillary number, the deformation parameter D, and the major axis inclination angle θ decrease by about 1% and 3.8%, respectively, upon increasing E_b^* from 0 to 0.002.

It appears that the value of E_b^* at which the wrinkles disappear strongly depends on η^*, λ and Ca. In order to have a better understanding of the order of magnitudes of E_b^* needed to maintain a stable capsule shape, we provide a phase space in terms of E_b^* and η^* in Fig. 5.7 for different values of Ca while λ is kept constant at 1. Figure 5.7(a) shows the regions of buckling for $Ca = 0.3$ only, whereas Fig. 5.7(b) is presented for different values of Ca from 0.05 to 1.0. The simulated data points are shown in Fig. 5.7(a), but not in Fig. 5.7(b) to avoid cluttering. Here we observe two different behaviors of the curves separating buckling and stable regimes depending on the capillary number. At low values of Ca (e.g., below 0.1), buckling occurs in the

absence of bending resistance for all values of η^* as noted in the previous sections. Hence, in this range, bending stiffness is needed for all values of η^* to prevent buckling, and the curves tend to be horizontal for low values of Ca and η^*. In contrast, at higher values of Ca (e.g., above 0.3), buckling usually occurs for $\eta^* \gtrsim 10$. Thus, the lines are vertical in this range of higher values of Ca and low values of η^*. We find that in order to prevent buckling at higher values of Ca, E_b^* should be significantly higher than the one considered at lower values of Ca. Similar phase spaces in terms of E_b^* and η^* are also obtained for other values of λ which are not shown. We find that the size of the region showing buckling in the phase space decreases with increasing λ.

We note in Fig. 5.7 that the values of E_b^* needed to prevent buckling are in the range 10^{-4} – 10^{-2}. This range is considerably higher than $E_b^* \approx O(10^{-5})$ predicted by Walter *et al.* [75] for artificial capsules. For red blood cells, the range of bending rigidity is 1–9$\times 10^{-19}$ J [2, 13, 87], which suggests that E_b^* could be as high as ~ 0.01 if we take $E_s \approx$ 2–6 μN/m [86], and $a_o \sim 3$ μm. While the high value of E_b^* needed in our simulations could be purely due to numerical reasons, it also suggests that further experiments are necessary for accurate measurements of the membrane viscosity and the bending stiffness for artificial capsules. In our subsequent simulations we take a relatively high value of $E_b^* = 0.01$ which is observed to stabilize the capsule shape over a broad range of Ca and η^* considered here.

5.2.2 Deformation, inclination and tank-treading frequency

The effect of membrane viscosity on the time-dependent deformation parameter $D(t)$ and inclination angle $\theta(t)$ is shown in Fig. 5.8(a) and (b), respectively. Here we consider $Ca = 0.6$ and $\lambda = 1$, and vary η^* from 0 to 100. We observe that increasing

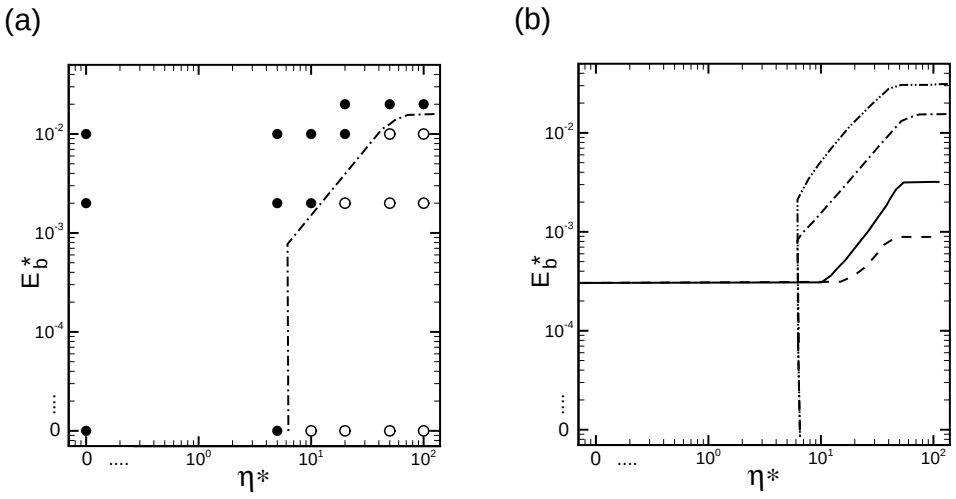

Figure 5.7: E_b^* vs. η^* phase space plot for membrane buckling of the spherical capsules. Here $\lambda = 1$. (a) $Ca = 0.3$; filled symbols represent no buckling, and open symbols represent buckling. (b) The lines are separating regions with or without buckling for $Ca = 0.05$ $(- - -)$; $Ca = 0.1$ (——); $Ca = 0.6$ $(- \cdot -)$; and $Ca = 1.0$ $(- \cdot\cdot -)$.

the membrane viscosity leads to a damped oscillatory behavior of D and θ. Such oscillatory motion is also combined with the tank-treading motion. For lower values of η^*, the oscillation decays rapidly, but it sustains for a longer time as η^* increases. Also noteworthy is the large amplitude of oscillation of θ, particularly for $\eta^* = 100$ in the figure. The oscillation at higher η^* sustains for a long time because the capsule response time μ_s/E_s becomes increasingly longer than the flow time scale $\dot{\gamma}^{-1}$ with increasing η^*. We further observe that the oscillation also increases with increasing Ca and λ if η^* is kept constant at non-zero values (data not shown). Interestingly, the asymptotic analysis of Barthès-Biesel & Sgaier [52] with viscoelastic membrane found an initial transient response in the range $\beta = O(1)$, and a non-decaying time-periodic oscillation in the viscous limit $\beta \to \infty$.

The time-averaged deformation parameter $\overline{D}$ as a function of η^* is presented in Fig. 5.9. Two important observations are made here. First, $\overline{D}$ decreases with increasing η^*. Hence, the membrane viscosity η^* restricts the capsule deformation in a similar

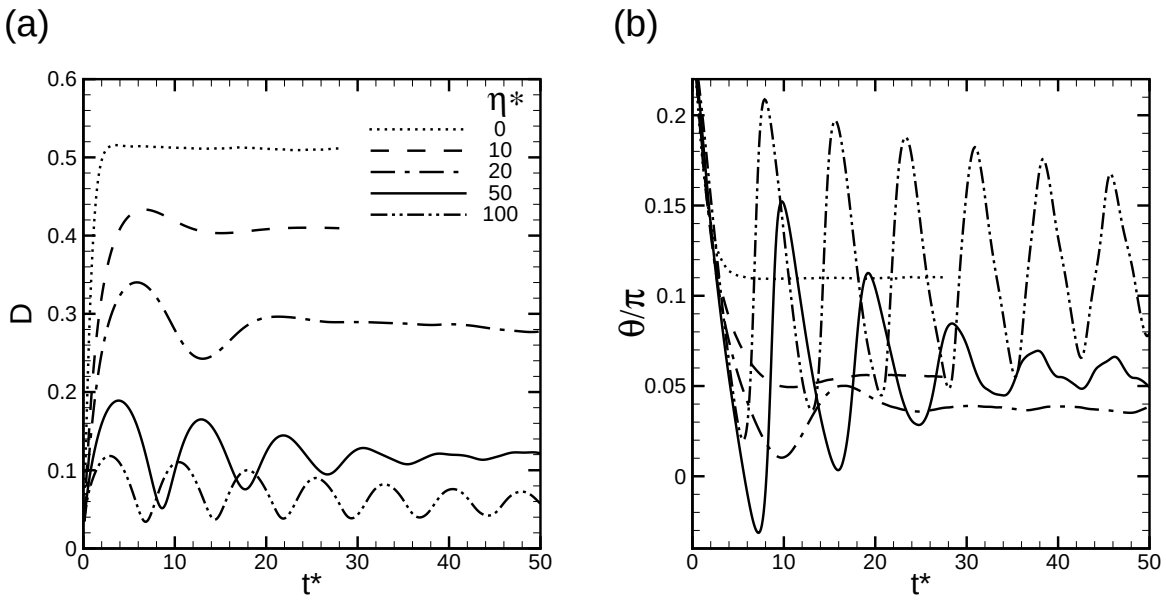

Figure 5.8: Transient response of (a) deformation parameter D, and (b) inclination angle θ at $Ca = 0.6, \lambda = 1$ for increasing values of η^* as $\eta^* = 0$ ($\cdots$); 10 ($- - -$); 20 ($- \cdot -$); 50 (——); and 100 ($- \cdot\cdot -$).

way that the internal to external fluid viscosity ratio λ does. Second, in the limit of very high η^*, the deformation parameter at different values of Ca tends to merge and eventually approaches zero. This numerical trend is in agreement with the analytical finding of Barthès-Biesel & Sgaier [52] that $\overline{D} \sim 1/\eta^*$ as $\beta \to \infty$. We have also obtained similar trend of $\overline{D}$ versus η^* for different values of λ (data not shown), and observed that $\overline{D}$ for different values of λ tends to merge and eventually approaches zero as η^* becomes large. Thus, in the limit of high membrane viscosity, deformation is nearly independent of Ca and λ, and eventually becomes severely restricted.

The average inclination angle $\overline{\theta}$ is presented in Fig. 5.10 as a function of η^* for different values of Ca. We note that the behavior of $\overline{\theta}$ with respect to η^* is rather complex as $\overline{\theta}$ varies nonmonotonically: it first decreases with increasing η^* reaching a minimum, but increases again upon further increase in η^*. The minimum of $\overline{\theta}$ is reached near $\eta^* \approx 20$ for $Ca = 0.6$ and 1.0 when the oscillation in time-dependent

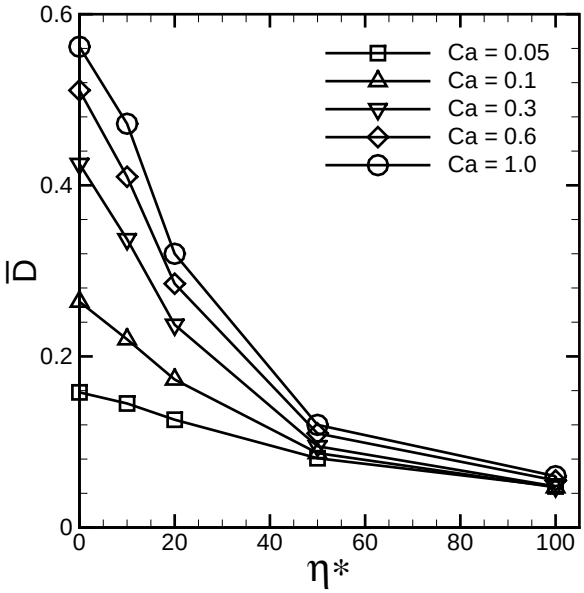

Figure 5.9: Time-averaged deformation parameter $\overline{D}$ as a function of η^* for different values of Ca. Here $\lambda = 1$.

θ becomes strong. This nonmonotonic trend will be explained later. The second interesting feature of $\overline{\theta}$ observable in Fig. 5.10 is its variation with respect to Ca when different values of η^* are considered. At small values of η^* ($\lesssim 10$), $\overline{\theta}$ decreases with increasing Ca, but the trend is reversed at high values of η^* (e.g., at 100). Thus, unlike $\overline{D}$ which is nearly independent of Ca as $\eta^* \to \infty$, $\overline{\theta}$ appears to be strongly dependent on Ca even in this limit.

The effect of membrane viscosity on tank-treading frequency is shown in Fig. 5.11 where we plot the dimensionless frequency $\nu^* = 4\pi/\dot{\gamma}T_{tt}$ where T_{tt} is the tank-treading period. A nonmonotonic behavior of ν^* is observed with an initial decrease to a minimum followed by an increase approaching the rigid sphere limit with increasing η^*. The initial decrease in ν^*, which is more pronounced at large Ca, is due to an increase in dissipation. For larger values of η^*, the subsequent increase in ν^* is due to a decrease in the dissipation as the internal velocity gradient gradually diminishes

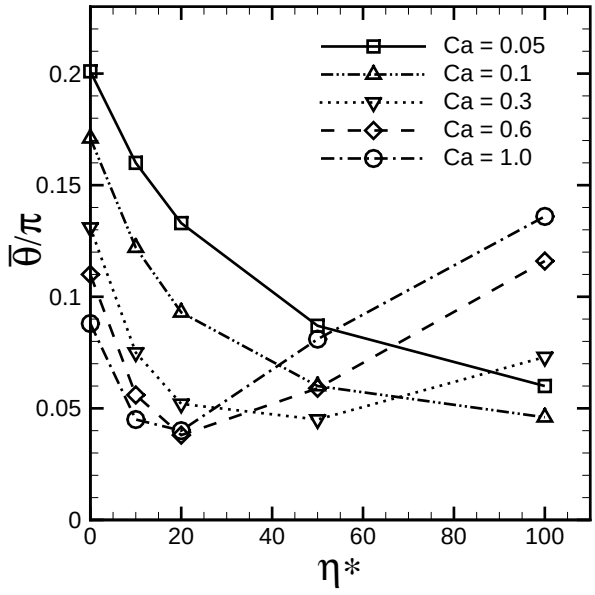

Figure 5.10: Average inclination angle $\overline{\theta}$ as a function of η^* for different values of Ca. Here $\lambda = 1$.

as the rigid particle limit is approached.

Based on the result obtained for ν^*, we can now explain the nonmonotonic trend of $\overline{\theta}$ w.r.t. η^* observed earlier in Fig. 5.10. Following Keller & Skalak [7], the equilibrium of moments on the capsule requires that

$$M_s + M_f + M_t = 0, \tag{5.1}$$

where M_s is the moment due to the external shear acting on a rigid ellipsoid inclined at an angle θ, M_f is the moment due to the unsteady oscillatory motion of the capsule, and M_t is the moment due to the stationary tank-treading motion. For a globally

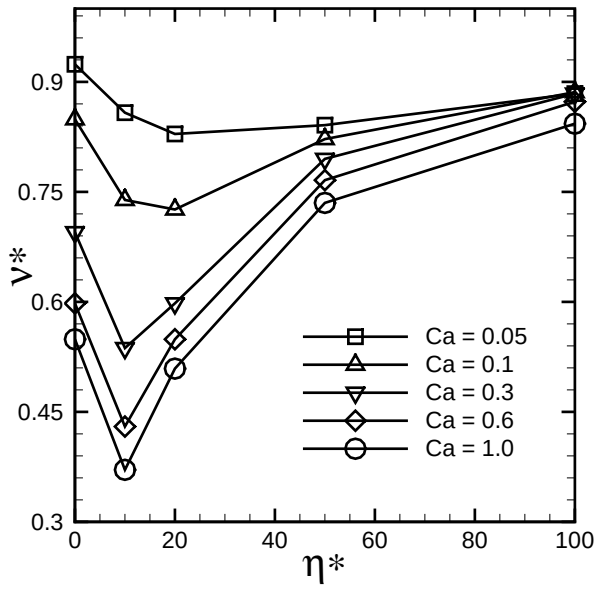

Figure 5.11: Normalized tank-treading frequency $\nu^* = 4\pi/\dot{\gamma}T_{tt}$ of spherical capsules as a function of η^* for different values of Ca. Here $\lambda = 1$.

nondeformable capsule of ellipsoidal shape,

$$M_s \sim \mu_o\dot{\gamma}\left[L^2\sin^2\theta + B^2\cos^2\theta\right] \tag{5.2}$$

$$M_f \sim \mu_o\left(L^2 + B^2\right)d\theta/dt, \quad \text{and} \tag{5.3}$$

$$M_t \sim \nu\left[\mu_s F_1 + \mu_o F_2\right], \tag{5.4}$$

where F_1 and F_2 depend on capsule geometry, and ν is the dimensional tank-treading frequency. For small values of η^*, the oscillations in θ are small, and hence, M_f is negligible. In this range, M_s is balanced by M_t. Further, Fig. 5.11 shows a sharp decrease of ν^* upon increasing η^* at high Ca, which in turn, will cause M_t to decrease. Hence, θ must decrease so as to balance the decreasing M_t as η^* increases. For large values of η^*, however, the angular oscillation is large, and hence, M_f is not negligible. In addition, ν^* also increases in this range, which in turn, causes an increase in M_t.

In order to balance the increasing $M_f + M_t$, θ must increase so as to increase M_s.

5.3 Nonspherical Capsules: Dynamics and Phase Diagrams

As mentioned before, an initially nonspherical capsule may undergo swinging motion combined with the membrane tank-treading at high values of Ca or low values of λ, and the tumbling motion at low values of Ca or high values of λ (see e.g., [11, 12, 41, 42, 75]). Here we study the influence of the membrane viscosity on such motions. We restrict our study to an oblate initial shape with the minor to major axis ratio $\alpha = 0.7$.

We present the snapshots of capsules with different dynamics as well as their time-dependent inclination angle θ and deformation parameter D in Fig. 5.12, where Ca and λ are fixed as η^* is varied. Figs. 5.12(a)-(c) present the time-dependent capsule shape, and (d) and(e) present time-dependent deformation parameter and inclination angle, respectively. For $\eta^* = 10$ in Fig. 5.12(a), we observe a swinging (SW) motion in which the capsule undergoes periodic angular oscillation. The swinging motion is superimposed with the tank-treading motion of the membrane as shown by a marker point. The swinging motion is also accompanied by a periodic shape oscillation as evident from Fig. 5.12(d). We note that during this motion, the major axis remains bounded within the extensional quadrant of the flow ($0 < \theta < \pi/4$). When η^* is increased to 50 as in Fig. 5.12(b), large oscillation in θ and D is noted. Here the capsule enters the compressional quadrant of the flow (i.e., θ becomes negative), but fails to make a complete tumbling. In this case, the capsule shape instantaneously becomes nearly spherical; thus, a major axis cannot be well defined during that instant and the inclination angle computed should be taken with caution. The minimum value

of D occurs when capsule is in the compressional quadrant. Since the tumbling motion is masked by a large shape oscillation, we identify such motion as the *transitional* (TR) dynamics. For very high η^* values e.g., $\eta^* = 100$ in Fig. 5.12(c), a clear tumbling (TU) motion occurs, and θ oscillates between $+\pi/2$ and $-\pi/2$. The capsule can also experience some amount of shape oscillation during the tumbling motion as evident from Fig. 5.12(d).

The dynamics presented above is observed to be periodic, and it occurs for small to moderate values of Ca. For higher values of Ca, a transient behavior is observed in which the capsule starts with one mode of dynamics, and then switches to another mode. The time-dependent deformation parameter and inclination angle are shown in Fig. 5.13 to illustrate such transient motions. In Fig. 5.13(a), which is for $Ca = 0.3$ and $\eta^* = 50$, a TR dynamics is observed at the beginning followed by a SW dynamics, which continues for the rest of the simulation. It can be noted that D drops drastically to approximately zero, and θ becomes negative in the first cycle indicating the TR motion. When η^* is increased to 75 while Ca is held constant at 0.3 as in Fig. 5.13(b), a TU mode is observed at the beginning, which is then followed by a TR mode that continues for the rest of the simulation. Similar transient motion was observed by Kessler *et al.* [42] and Bagchi & Kalluri [14] for capsules with an elastic membrane.

We have performed a number of simulations to observe the swinging to tumbling transition by varying η^* and Ca. Fig. 5.14 presents the phase diagram showing different dynamical regimes. The swinging motion primarily occurs at small values of η^* and large Ca, whereas the tumbling motion is observed for large η^* and small Ca. For small values of Ca, the transition occurs as SW to TR to TU with increasing η^*. It is noteworthy that at small values of η^*, SW to TR to TU transition can also be

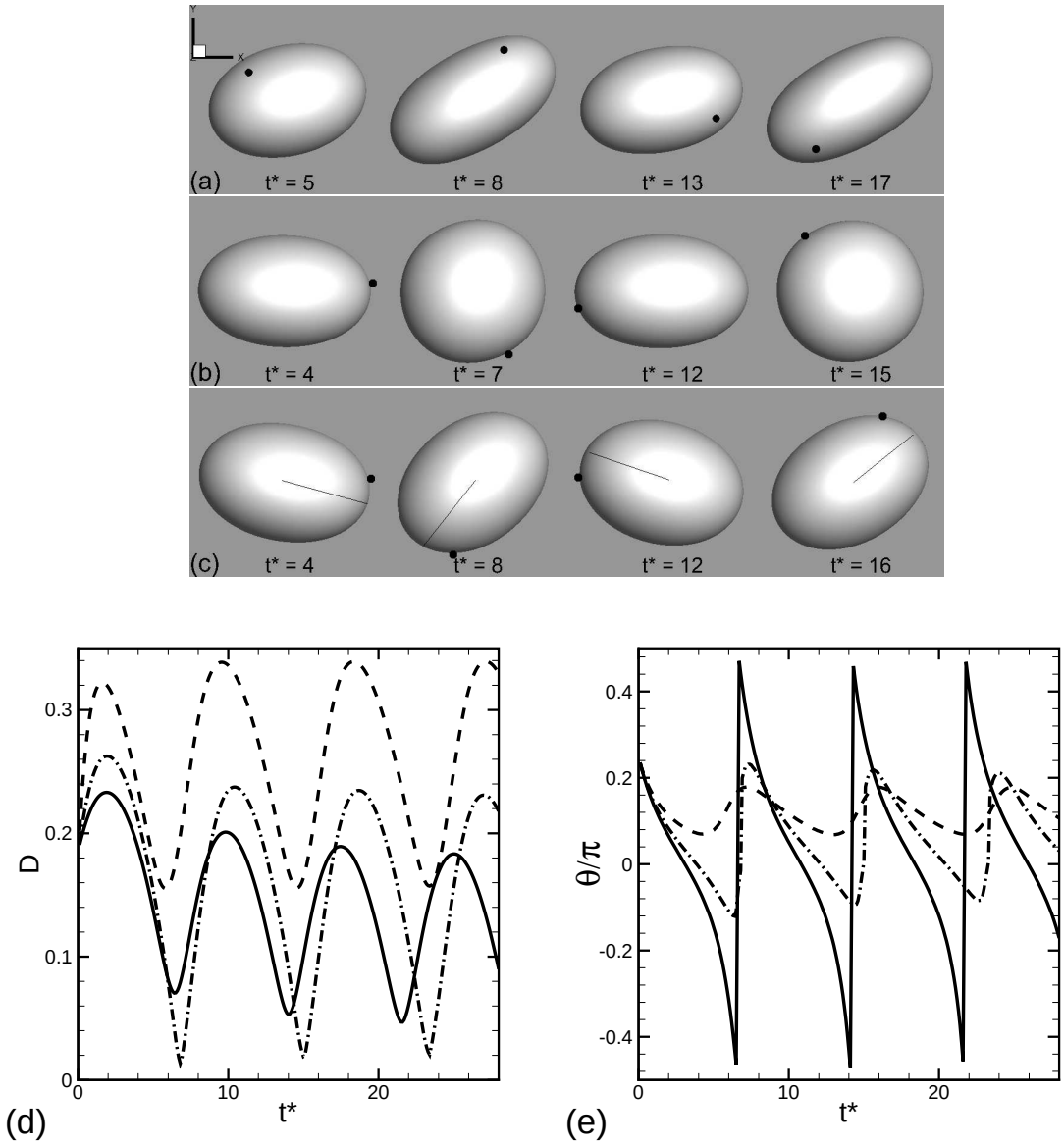

Figure 5.12: The effect of membrane viscosity on transition from swinging to tumbling motion. Here $\alpha = 0.7, Ca = 0.1, \lambda = 1$. Time-dependent shapes are shown in (a) swinging (SW), $\eta^* = 10$; (b) transition (TR), $\eta^* = 50$; and (c) tumbling (TU), $\eta^* = 100$. Also, (d) time-dependent deformation parameter D, and (e) inclination angle θ are given for the above three cases in (a), (b) and (c) using dashed, dash-dotted and solid lines, respectively.

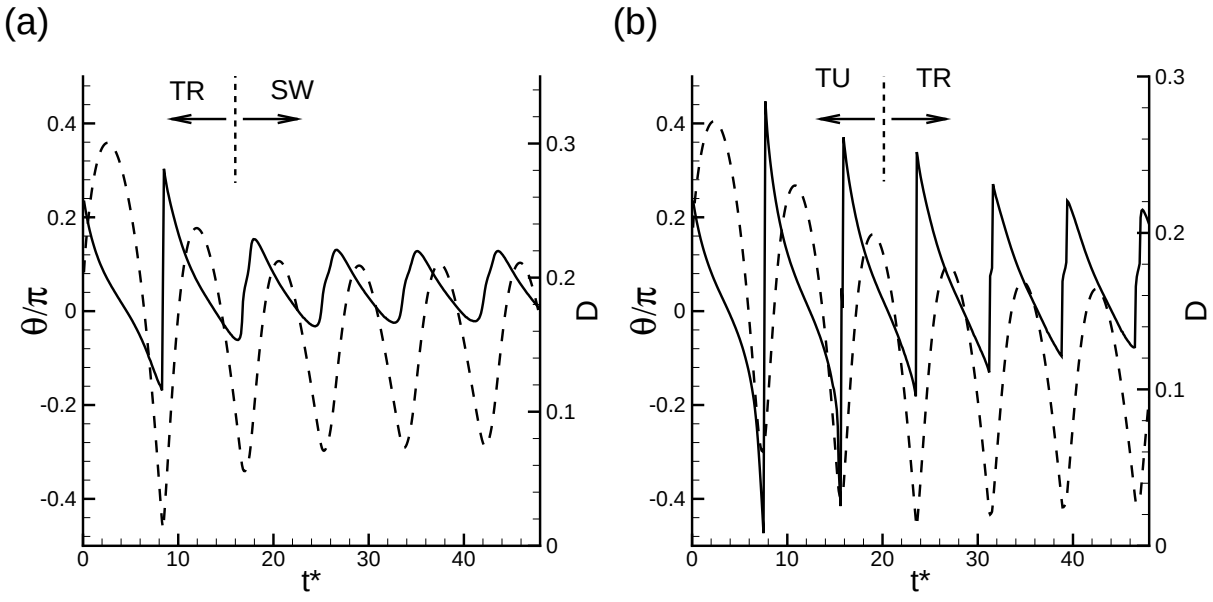

Figure 5.13: Transient motion of nonspherical capsules ($\alpha = 0.7$) at high shear $Ca = 0.3$. (a) $\eta^* = 50$; here a TR dynamics at the beginning is followed by a SW dynamics. (b) $\eta^* = 75$; here a TU dynamics at the beginning is followed by a TR dynamics. Time-dependent inclination angle θ (left axis, ——), and deformation parameter D (right axis, $- - -$) are shown.

achieved by reducing Ca as well. For large Ca, the transient region occurs between the SW and TU regions. In this region, capsules undergo an initial transience and then switch to their final stable dynamics. We identify these regions as TR $\rightarrow$ SW and TU $\rightarrow$ TR dynamics. Nevertheless, the final dynamics observed for these transient regimes is either SW or TR. Therefore, in Fig. 5.14, we separate the three major (SW, TR and TU) zones by solid lines, and the transient zones by dashed lines. We observe that increasing the viscosity contrast λ to 5 in Fig. 5.14(b) will inhibit the SW dynamics significantly when the membrane viscosity is taken into account. Further, as λ increases, the transition from SW to TU occurs earlier upon increasing η^*. The above results suggest that the membrane viscosity has a similar effect on SW to TU transition as the viscosity ratio λ or $1/Ca$ does.

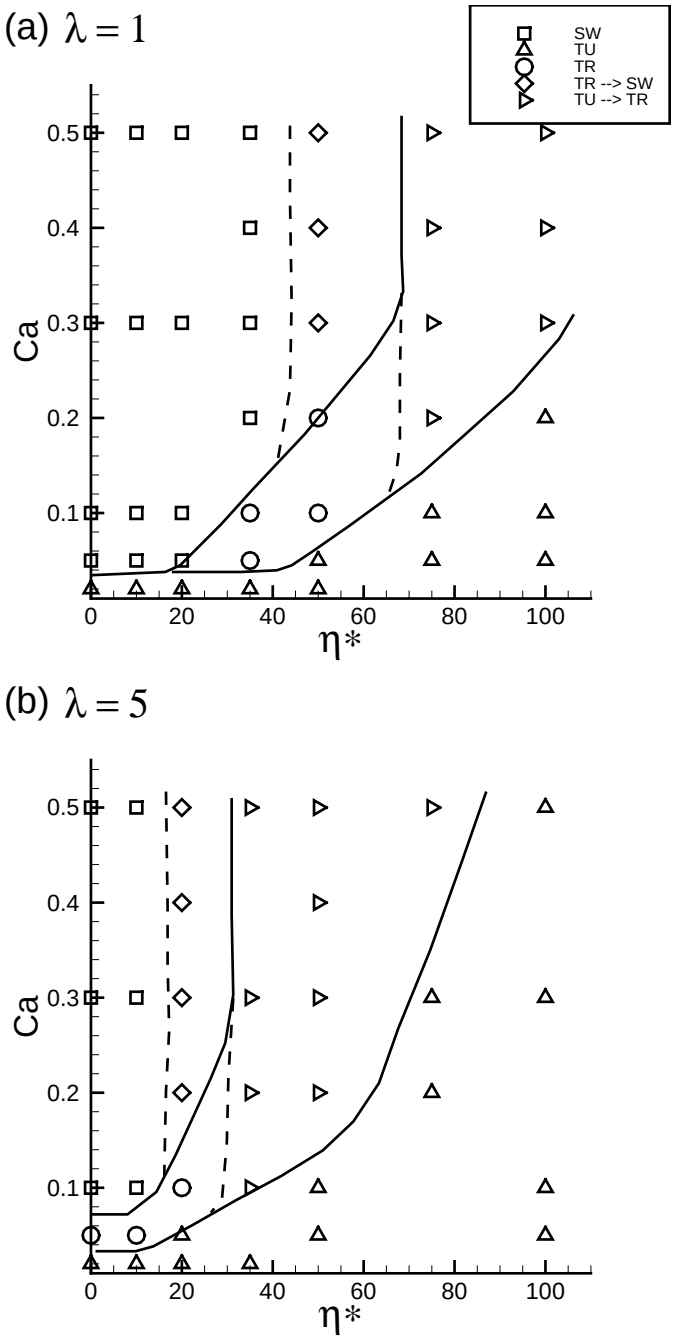

Figure 5.14: Phase diagrams in $(Ca - \eta^*)$ space for non-spherical capsules with aspect ratio $\alpha = 0.7$. (a) $\lambda = 1$; and (b) $\lambda = 5$. □ swinging, △ tumbling, ◯ transition, ◇ TR → SW, ▷ TU → TR.

5.4 Conclusion

In this chapter, we presented a numerical analysis on the influence of membrane viscosity on the dynamics of capsules in linear shear flow. We presented a comprehensive study on the buckling, deformation, and dynamics of capsules over a broad range of capillary number Ca, internal to external fluid viscosity ratio λ, and the dimensionless membrane viscosity η^*.

One of the most important findings of this study is that the membrane viscosity causes buckling in the range of capillary numbers for which no buckling is observed for capsules with purely elastic membrane. Analysis of membrane stress shows that at small capillary numbers, the membrane viscosity has a relatively less impact, and the onset of buckling is determined by the capillary number. At moderate to large capillary numbers, the wrinkles appear at $\eta^* \sim 10$ which is nearly in the same range as the experimentally measured values of the membrane viscosity reported for artificial capsules and red blood cells. At this range of Ca, introduction of a small membrane viscosity first redistributes the compressive stress from the tips of the capsule to the equatorial rim. Upon further increase in the membrane viscosity, the compressive stress spreads back from the rim towards the tips. Further, increasing the viscosity ratio λ shows a stabilizing effect. In order to suppress buckling, we introduce the membrane bending stiffness. It is observed that the range of the bending stiffness required at high capillary number is considerably higher than that estimated for artificial capsules, but in the same range as that reported for red blood cells.

After removing the wrinkles by introducing the bending stiffness, we studied the influence of membrane viscosity on capsule deformation, inclination, tank-treading frequency, and swinging to tumbling transition. The membrane viscosity is observed

to reduce time-averaged capsule deformation, and introduce damped oscillation in time-dependent deformation and inclination. The time-averaged inclination angle shows a nonmonotonic trend with an initial decrease reaching a minimum and a subsequent increase with increasing η^*. A similar nonmonotonic trend is observed in the tank-treading frequency.

We then considered the influence of membrane viscosity on the unsteady dynamics of an initially nonspherical capsule. The dynamics is observed to change from swinging to tumbling with increasing membrane viscosity, when Ca and λ are held constant. Further, in some range of Ca and η^*, transient dynamics is observed in which the capsule starts with a transitional or tumbling dynamics, then settles at a swinging or transitional dynamics. In that respect, membrane viscosity has a similar effect on capsule dynamics as λ or $1/Ca$ does.

Chapter 6

Conclusion and Directions for Future Work

6.1 Conclusion

In this thesis, we presented three-dimensional numerical simulations of dynamics and deformation of microscopic deformable cells with elastic and viscoelastic membranes suspended in simple shear flow using immersed boundary/front-tracking method. The objective was to understand the complex fluid/structure interaction problem for membrane-bound soft matter in dilute suspensions. Our numerical technique is able to simulate the complex dynamics of the cells, i.e., vesicles, capsules, and red blood cells, in the tank-treading, breathing, trembling, and tumbling modes. The front-tracking method presented here is an alternative to the boundary integral method, which has been often used in other numerical studies. The choice of the front-tracking method over the boundary-integral method is due to the straightforward implementation and versatility. The current method can be readily extended to include membrane shear resistance (e.g., [35]), membrane viscosity, and most importantly finite Reynolds number effect, which could be the case for giant vesicles and capsules. Further, the present method is very stable over a large range of the control parameters, such as shear rate, viscosity contrast, bending stiffness etc., and hence, long simulations can be performed without losing numerical stability. In addition, in

case of a structured grid of the cell surface, there is the possibility of mesh entanglement in the poles, which is not the case here. We do not observe local coarsening or entanglement of surface mesh over the length of the simulations; thus, no remeshing is done.

The main results of this thesis can be summarized as follows:

1. **Vesicle dynamics:** A detailed comparison of the numerical results is made with various theoretical models and experiments. It is found that the applicability of the theoretical models is limited despite some general agreement with the simulations and experiments. The deviations between the perturbative results and the simulation results occur even in the absence of thermal noise. Specifically, we find that the vesicle dynamics does not follow a self-similar behavior in a two-parameter phase space. Rather, the dynamics is governed by three controlling parameters, namely, the excess area, viscosity ratio, and the dimensionless shear rate. Additionally, we find that a linear scaling of the tank-treading angle is possible only for quasi-spherical vesicles. The breakdown of the scaling occurs at higher values of the excess area even in the absence of thermal noise. We find that the vesicle deformation saturates at large shear rates, and the asymptotic deformation matches well with a theoretical prediction for quasi-spherical vesicles. The dependence of the critical viscosity ratio associated with the onset of unsteady dynamics on the vesicle excess area is in excellent agreement with the experimental observation. We show that near the transition between the tank-treading and tumbling dynamics, both the vacillating-breathing-like motion characterized by a smooth ellipsoidal shape, and the trembling-like motion characterized by a highly deformed shape are possible. For the trembling-like motion, the shape is highly three-dimensional with concavities and lobes, and the vesicle deforms

more in the vorticity direction than in the shear plane. A Fourier spectral analysis of the vesicle shape shows the presence of the odd harmonics and higher-order modes beyond fourth order.

2. **Red blood cell dynamics:** We present phase diagrams of the single red blood cell dynamics in dilute suspension. The computational geometry replicates an *in vitro* linear shear flow apparatus. We find that during the breathing motion at moderate bending rigidity, the cell either completely aligns with the flow direction and the membrane folds inward forming two cusps, or, it undergoes large swinging motion while deep, crater-like dimples periodically emerge and disappear. At lower bending rigidity, the breathing motion occurs over a wider range of shear rates, and is often characterized by the emergence of a quad-concave shape. The effect of the breathing dynamics on the tank-treading-to-tumbling transition is illustrated by detailed phase diagrams, which appear to be more complex and richer than those of vesicles. In a remarkable departure from the vesicle dynamics, and from the classical theory of non-deformable cells, we find that there exists a critical viscosity ratio below which the transition is independent of the viscosity ratio, and dependent on shear rate only. Further, unlike the reduced-order models, the present simulations do not predict any intermittent dynamics of the red blood cells. The red blood cell tank-treading frequency was shown to be an inverse linear function of the viscosity ratio, which is in agreement with the theoretical models for shape-preserving cells. For a purely elastic RBC, the tank-treading frequency behaves almost linearly with respect to the capillary number, whereas a power-law behavior is observed when the membrane viscosity is taken into account.

3. **Influence of the membrane viscosity:** Most previous numerical studies on

capsule dynamics in shear flow have ignored the role of membrane viscosity. Therefore, we presented a numerical method for large deformation of capsules using a Kelvin–Voigt viscoelastic model for the membrane. We also gave a comprehensive analysis of the influence of the membrane viscosity on buckling, deformation and dynamics. We observe that the membrane viscosity leads to buckling in the range of shear rates in which no buckling is observed for capsules with purely elastic membrane. For moderate to large shear rates, the wrinkles on the capsule surface appear in the same range of the membrane viscosity that was reported earlier for artificial capsules and red blood cells based on experimental measurements. In order to obtain stable shapes, it is necessary to introduce the bending stiffness. It is observed that the range of the bending stiffness required is also in the same range as that reported for the red blood cells, but considerably higher than that estimated for artificial capsules. Using the stable shapes obtained in the presence of bending stiffness, we analyzed the influence of membrane viscosity on deformation, inclination, and tank-treading frequency of initially spherical capsules. Membrane viscosity is observed to reduce the capsule deformation, and introduce a damped oscillation in time-dependent deformation and inclination. The time-averaged inclination angle shows a nonmonotonic trend with an initial decrease reaching a minimum and a subsequent increase with increasing membrane viscosity. A similar nonmonotonic trend is also observed in the tank-treading frequency. We then considered the influence of the membrane viscosity on the unsteady dynamics of an initially oblate capsule. The dynamics is observed to change from a swinging motion to a tumbling motion with increasing membrane viscosity. Further, a transient dynamics is also observed in which a capsule starts with one type of dynamics, but settles with a different dynamics over a long time.

6.2 Future Work

As discussed in Chapter 5, most of the previous numerical studies on cell dynamics in shear flow considered purely elastic membrane. This study shows how the shear viscosity coupled with other membrane properties can produce a rich yet profound effect on capsule dynamics. The viscoelastic model presented here can be easily extended to consider the biconcave resting shape of red blood cells. In Chapter 4 we presented complex shape oscillation of red blood cells with purely elastic membrane. It is of future interest to study the influence of membrane viscosity on such dynamics, and to conduct a detailed study on the tank-treading frequency of red blood cells, which is often measured in experiments and used to extract the mechanical properties of the cell.

In our study of a single RBC in the shear flow we showed the membrane folding and the emergence of quad-concave shapes of the cell for lower values of bending rigidities. This can be further attributed to the cell membrane buckling, which has been observed in the experiments of Fischer *et al.* [93]. The influence of the membrane viscosity and bending stiffness on the buckling can be addressed in more detail.

Moreover, in the present study, we consider a normal biconcave RBC shape, which is initially stress free. Assuming different values of surface area-to-volume ratio (also known as the 'swelling ratio') to change the RBC initial shape, along with the inclusion of pre-stresses in the membrane will vary the dynamics of the cells and the phase diagrams. This will definitely enrich the study of the single cell dynamics in shear flow.

One of the very important and challenging problems remained open in this field to address is the dynamics and rheology of red blood cells in a dense suspension. First,

one can explore the orientation and deformation dynamics of the RBCs for different values of volume fractions, and illustrate the inter-particle interactions leading to what is known as 'shear induced diffusion'. Different values of viscosity ratios and capillary numbers in addition to the physiological values should be considered to make the study complete. Next, the role of volume fraction on the rheology of suspensions should be addressed. One should investigate the cell shear stress and normal stress difference in detail, and explain their trends for different capillary numbers, viscosity ratios and volume fractions.

Last but not least, the role of thermal noise on generating a convoluted vesicle shape and on the transition dynamics has been observed in the experiments (e.g., Kantsler & Steinberg [16]). A Fourier spectral analysis of the vesicle shapes in the shear plane has also showed the presence of higher modes of harmonics (Zabusky *et al.* [28]), which are attributed to the membrane wrinkles. We showed that even in the absence of thermal noise, we are able to observe highly-deformed shapes of the vesicles in the transition zone. We believe that the presence of thermal fluctuations in the numerical simulations can enhance the asymmetries and wrinkles in the shapes. There has been a growing interest in the study of vesicle shape relaxation time in a time-dependent shear flow (Kantsler *et al.* [27]), and a stretched vesicle relaxation time under no flow conditions (Zhou *et al.* [96]), for which cases thermal noise effects are significant. Thus, the inclusion of thermal noise in the numerical simulations will enrich the studies of vesicle dynamics and the relaxation times.

References

[1] Q. Zhu, C. Vera, R. J. Asaro, P. Sche, and L. A. Sung. A hybrid model for erythrocyte membrane: A single unit of protein network coupled with lipid bilayer. *Biophysical Journal*, **93**(2):386, 2007.

[2] N. Mohandas and E. Evans. Mechanical properties of the red cell membrane in relation to molecular structure and genetic defects. *Annual Review of Biophysics & Biomolecular Structure*, **23**:787, 1994.

[3] Y. C. Fung. *Biomechanics: Mechanical properties of living tissues.* Springer-Verlag, 1993.

[4] C. Pozrikidis. *Modeling and simulation of capsules and biological cells.* Chapman & Hall/CRC, 2003.

[5] H. Goldsmith and J. Marlow. Flow behaviour of erythrocytes I. rotation and deformation in dilute suspensions. *Proceedings of the Royal Society B*, **182**:351, 1972.

[6] J. Deschamps, V. Kantsler, and V. Steinberg. Phase diagram of single vesicle dynamical states in shear flow. *Physical Review Letters*, **102**:118105, 2009.

[7] S. R. Keller and R. Skalak. Motion of a tank-treading ellipsoidal particle in a shear flow. *Journal of Fluid Mechanics*, **120**:27, 1982.

[8] R. Tran-Son-Tay, S. P. Sutera, and P. R. Rao. Determination of red blood cell membrane viscosity from rheoscopic observations of tank-treading motion. *Biophysical Journal*, **46**:65, 1984.

[9] T. M. Fischer, M. Stöhr-Liesen, and H. Schmid-Schönbein. The red cell as a fluid droplet: Tank tread-like motion of the human erythrocyte membrane in shear flow. *Science*, **202**:894, 1978.

[10] T. M. Fischer. Tank-tread frequency of the red cell membrane: Dependence on the viscosity of the suspending medium. *Biophysical Journal*, **93**:2553, Oct 2007.

[11] J. M. Skotheim and T. W. Secomb. Red blood cells and other nonspherical capsules in shear flow: Oscillatory dynamics and the tank-treading-to-tumbling transition. *Physical Review Letters*, **98**:078301, 2007.

[12] M. Abkarian, M. Faivre, and A. Viallat. Swinging of red blood cells under shear flow. *Physical Review Letters*, **98**:188302, 2007.

[13] D. H. Boal. *Mechanics of the cell.* Cambridge University Press, 2002.

[14] P. Bagchi and R. Murthy Kalluri. Dynamics of nonspherical capsules in shear flow. *Physical Review E*, **80**:016307, 2009.

[15] V. Kantsler and V. Steinberg. Orientation and dynamics of a vesicle in tank-treading motion in shear flow. *Physical Review Letters*, **95**:258101, 2005.

[16] V. Kantsler and V. Steinberg. Transition to tumbling and two regimes of tumbling motion of a vesicle in shear flow. *Physical Review Letters*, **96**:036001, 2006.

[17] M. A. Mader, V. Vitkova, M. Abkarian, A. Viallat, and T. Podgorski. Dynamics of viscous vesicles in shear flow. *The European Physical Journal E*, **19**(4):389, 2006.

[18] D. Barthès-Biesel and J. M. Rallison. The time-dependent deformation of a capsule freely suspended in a linear shear flow. *Journal of Fluid Mechanics*, **113**:251, 1981.

[19] U. Seifert. Fluid membranes in hydrodynamic flow fields: Formalism and an application to fluctuating quasispherical vesicles in shear flow. *The European Physical Journal B*, **8**:405, 1999.

[20] V. V. Lebedev, K. S. Turitsyn, and S. S. Vergeles. Nearly spherical vesicles in an external flow. *New Journal of Physics*, **10**:043044, 2008.

[21] G. Danker, T. Biben, T. Podgorski, C. Verdier, and C. Misbah. Dynamics and rheology of a dilute suspension of vesicles: Higher-order theory. *Physical Review E*, **76**:041905, 2007.

[22] B. Kaoui, A. Farutin, and C. Misbah. Vesicles under simple shear flow: Elucidating the role of relevant control parameters. *Physical Review E*, **80**:061905, 2009.

[23] A. Farutin, T. Biben, and C. Misbah. Analytical progress in the theory of vesicles under linear flow. *Physical Review E*, **81**:061904, 2010.

[24] T. Biben, A. Farutin, and C. Misbah. Three-dimensional vesicles under shear flow: Numerical study of dynamics and phase diagram. *Physical Review E*, **83**:031921, 2011.

[25] K. H. De Haas, C. Blom, D. V. D. Ende, M. H. G. Duits, and J. Mellema. Deformation of giant lipid bilayer vesicles in shear flow. *Physical Review E*, **56**:7132, 1997.

[26] U. Seifert, K. Berndl, and R. Lipowsky. Shape transformations of vesicles: Phase diagram for spontaneous curvature and bilayer-coupling models. *Physical Review A*, **44**:1182, 1991.

[27] V. Kantsler, E. Segre, and V. Steinberg. Vesicle dynamics in time-dependent elongation flow: Wrinkling instability. *Physical Review Letters*, **99**:178102, 2007.

[28] N. J. Zabusky, E. Segre, J. Deschamps, V. Kantsler, and V. Steinberg. Dynamics of vesicles in shear and rotational flows: Modal dynamics and phase diagram. *Physics of Fluids*, **23**:041905, 2011.

[29] H. Zhao and E. S. G. Shaqfeh. The dynamics of a vesicle in simple shear flow. *Journal of Fluid Mechanics*, **674**:578, 2011.

[30] S. Meßlinger, B. Schmidt, H. Noguchi, and G. Gompper. Dynamical regimes and hydrodynamic lift of viscous vesicles under shear. *Physical Review E*, **80**:011901, 2009.

[31] S. K. Veerapaneni, D. Gueyffier, G. Biros, and D. Zorin. A boundary integral method for simulating the dynamics of inextensible vesicles suspended in a viscous fluid in 2D. *Journal of Computational Physics*, **228**:7233, 2009.

[32] S. K. Veerapaneni, A. Rahimian, G. Biros, and D. Zorin. A fast algorithm for simulating vesicle flows in three dimensions. *Journal of Computational Physics*, **230**:5610, 2011.

[33] W. Helfrich. Elastic properties of lipid bilayers: Theory and possible experiments. *Z. Naturforsch C*, **28**:693, 1973.

[34] O. -Y. Zhong-can and W. Helfrich. Bending energy of vesicle membranes: General expressions for the first, second, and third variation of the shape energy and applications to spheres and cylinders. *Physical Review A*, **39**:5280, 1989.

[35] R. V. Garimella and S. Swartz. Curvature estimation for unstructured triangulations of surfaces. *Technical Report*, LA-UR-03-8240, 2003.

[36] S. Petitjean. A survey of methods for recovering quadrics in triangle meshes. *ACM Computing Surveys*, **34**(2):211, 2002.

[37] M. Reuter, S. Biasotti, D. Giorgi, G. Patane, and M. Spagnuolo. Discrete Laplace–Beltrami operators for shape analysis and segmentation. *Computers & Graphics*, **33**:381, 2009.

[38] G. Xu. Convergence of discrete Laplace–Beltrami operators over surfaces. *Computers and Mathematics with Applications*, **48**:347, 2004.

[39] Z. Peng, R. J. Asaro, and Q. Zhu. Multiscale simulation of erythrocyte membranes. *Physical Review E*, **81**:031904, 2010.

[40] S. Ramanujan and C. Pozrikidis. Deformation of liquid capsules enclosed by elastic membranes in simple shear flow: large deformations and the ect of fluid viscosities. *Journal of Fluid Mechanics*, **361**:117, 1998.

[41] Y. Sui, H. T. Low, Y. T. Chew, and P. Roy. Tank-treading, swinging, and tumbling of liquid-filled elastic capsules in shear flow. *Physical Review E*, **77**:016310, 2008.

[42] S. Kessler, R. Finken, and U. Seifert. Swinging and tumbling of elastic capsules in shear flow. *Journal of Fluid Mechanics*, **605**:207, 2008.

[43] M. Kraus, W. Wintz, U. Seifert, and R. Lipowsky. Fluid vesicles in shear flow. *Physical Review Letters*, **77**(17):3685, 1996.

[44] H. Noguchi and G. Gompper. Fluid vesicles with viscous membranes in shear flow. *Physical Review Letters*, **93**:258102, 2004.

[45] H. Noguchi and G. Gompper. Dynamics of fluid vesicles in shear flow: Effect of membrane viscosity and thermal fluctuations. *Physical Review E*, **72**:011901, 2005.

[46] H. Noguchi and G. Gompper. Swinging and tumbling of fluid vesicles in shear flow. *Physical Review Letters*, **98**:128103, 2007.

[47] Y. Sui, Y. T. Chew, P. Roy, Y. P. Cheng, and H. T. Low. Dynamic motion of red blood cells in simple shear flow. *Physics of Fluids*, **20**:112106, 2008.

[48] C. Misbah. Vacillating breathing and tumbling of vesicles under shear flow. *Physical Review Letters*, **96**:028104, 2006.

[49] P. M. Vlahovska and R. S. Gracia. Dynamics of a viscous vesicle in linear flows. *Physical Review E*, **75**:016313, 2007.

[50] V. V. Lebedev, K. S. Turitsyn, and S. S. Vergeles. Dynamics of nearly spherical vesicles in an external flow. *Physical Review Letters*, **99**:218101, 2007.

[51] T. Biben, K. Kassner, and C. Misbah. Phase-field approach to three-dimensional vesicle dynamics. *Physical Review E*, **72**:041921, 2005.

[52] D. Barthès-Biesel and H. Sgaier. Role of membrane viscosity in the orientation and deformation of a spherical capsule suspended in shear flow. *Journal of Fluid Mechanics*, **160**:119, 1985.

[53] D. Barthès-Biesel. Motion of a spherical microcapsule freely suspended in a linear shear flow. *Journal of Fluid Mechanics*, **100**(04):831, 1980.

[54] K. S. Chang and W. L. Olbricht. Experimental studies of the deformation and breakup of a synthetic capsule in steady and unsteady simple shear flow. *Journal of Fluid Mechanics*, **250**:609, 1993.

[55] C. Pozrikidis. Finite deformation of liquid capsules enclosed by elastic membranes in simple shear flow. *Journal of Fluid Mechanics*, **297**:123, 1995.

[56] C. Pozrikidis. Effect of membrane bending stiffness on the deformation of capsules in simple shear flow. *Journal of Fluid Mechanics*, **440**:269, 2001.

[57] A. Z. K. Yazdani and P. Bagchi. Phase diagram and breathing dynamics of a single red blood cell and a biconcave capsule in dilute shear flow. *Physical Review E*, **84**:026314, 2011.

[58] A. Diaz, D. Barthès-Biesel, and N. Pelekasis. Effect of membrane viscosity on the dynamic response of an axisymmetric capsule. *Physics of Fluids*, **13**:3835, 2001.

[59] E. Lac, D. Barthès-Biesel, N. A. Pelekasis, and J. Tsamopoulos. Spherical capsules in three-dimensional unbounded stokes flows: effect of the membrane constitutive law and onset of buckling. *Journal of Fluid Mechanics*, **516**:303, 2004.

[60] C. D. Eggleton and A. S. Popel. Large deformation of red blood cell ghosts in a simple shear flow. *Physics of Fluids*, **10**(8):1834, 1998.

[61] S. K. Doddi and P. Bagchi. Effect of inertia on the hydrodynamic interaction between two liquid capsules in simple shear flow. *International Journal of Multiphase Flow*, **34**:375, 2008.

[62] S. K. Doddi and P. Bagchi. Lateral migration of a capsule in a plane poiseuille flow in a channel. *International Journal of Multiphase Flow*, **34**:966, 2008.

[63] P. Bagchi and R. Murthy Kalluri. Rheology of a dilute suspension of liquid-filled elastic capsules. *Physical Review E*, **81**:056320, 2010.

[64] R. Skalak, A. Tozeren, P. R. Zarda, and S. Chien. Strain energy function of red blood cell membranes. *Biophysical Journal*, **13**:245, 1973.

[65] C. S. Peskin. Numerical analysis of blood flow in the heart. *Journal of Computational Physics*, **25**:220, 1977.

[66] S. O. Unverdi and G. Tryggvason. A front-tracking method for viscous, incompressible, multi-fluid flows. *Journal of Computational Physics*, **100**:25, 1992.

[67] G. Tryggvason, B. Bunner, A. Esmaeeli, N. Al-Rawahi, W. Tauber, J. Han, S. Nas, and Y. Jan. A front-tracking method for the computations of multiphase flow. *Journal of Computational Physics*, **169**:708, 2001.

[68] J. M. Charrier, S. Shrivastava, and R. Wu. Free and constrained inflation of elastic membranes in relation to thermoforming-non-axisymmetric problems. *The Journal of Strain Analysis*, **24** (2):55, 1989.

[69] S. Shrivastava and J. Tang. Large deformation finite element analysis of non-linear viscoelastic membranes with reference to thermoforming. *The Journal of Strain Analysis*, **28**:31, 1993.

[70] S. K. Doddi. Three-dimensional computational modeling and simulation of biological cells and capsules. *PhD thesis*, 2008. Rutgers University.

[71] G. Ghigliotti, T. Biben, and C. Misbah. Rheology of a dilute two-dimensional suspension of vesicles. *Journal of Fluid Mechanics*, **653**:489, 2010.

[72] A. Walter, H. Rehage, and H. Leonhard. Shear-induced deformations of polyamide microcapsules. *Colloid & Polymer Science*, **278**:169, 2000.

[73] A. Walter, H. Rehage, and H. Leonhard. Shear induced deformation of microcapsules: shape oscillations and membrane folding. *Colloids and Surfaces A: Physicochemical and Engineering Aspects*, **183–185**:123, 2001.

[74] P. M. Vlahovska, Y. -N. Young, G. Danker, and C. Misbah. Dynamics of a non-spherical microcapsule with incompressible interface in shear flow. *Journal of Fluid Mechanics*, **678**:221, 2011.

[75] J. Walter, A. -V. Salsac, and D. Barthès-Biesel. Ellipsoidal capsules in simple shear flow: prolate versus oblate initial shapes. *Journal of Fluid Mechanics*, **676**:318, 2011.

[76] Y. C. Wang and P. Dimitrakopoulos. A three-dimensional spectral boundary element algorithm for interfacial dynamics in Stokes flow. *Physics of Fluids*, **18**:1, 2006.

[77] H. Zhao, A. H. G. Isfahani, L. N. Olson, and J. B. Freund. A spectral boundary integral method for flowing blood cells. *Journal of Computational Physics*, **229**:3726, 2010.

[78] P. Pranay, S. G. Anekal, J. P. Hernandez-Ortiz, and M. D. Graham. Pair collisions of fluid-filled elastic capsules in shear flow: Effects of membrane properties and polymer additives. *Physics of Fluids*, **22**:123103, 2010.

[79] D. V. Le. Effect of bending stiffness on the deformation of liquid capsules enclosed by thin shells in shear flow. *Physical Review E*, **82**:016318, 2010.

[80] X. Li and K. Sarkar. Front tracking simulation of deformation and buckling instability of a liquid capsule enclosed by an elastic membrane. *Journal of Computational Physics*, **227**(10):4998, 2008.

[81] E. Foessel, J. Walter, A. -V. Salsac, and D. Barthès-Biesel. Influence of internal viscosity on the large deformation and buckling of a spherical capsule in a simple shear flow. *Journal of Fluid Mechanics*, **672**:477, 2011.

[82] R. Finken and U. Seifert. Wrinkling of microcapsules in shear flow. *Journal of Physics: Condensed Matter*, **18**:L185, 2006.

[83] E. H. Dill. *The finite element method for mechanics of solids with ANSYS applications.* CRC Press, 2012.

[84] G. A. Holzapfel. *Nonlinear solid mechanics: A continuum approach for engineering.* Wiley, 2000.

[85] *ABAQUS/Standard theory manual (Version 6.3).* Hibbitt, Karlsson & Sorensen, Inc, 2002.

[86] S. Hénon, G. Lenormand, A. Richert, and F. Gallet. A new determination of the shear modulus of the human erythrocyte membrane using optical tweezers. *Biophysical Journal*, **76**:1145, 1999.

[87] L. Scheffer, A. Bitler, E. Ben-Jacob, and R. Korenstein. Atomic force pulling: probing the local elasticity of the cell membrane. *European Biophysical Journal*, **30**:83, 2001.

[88] E. Evans, and R. Hochmuth. Membrane viscoelasticity. *Biophysical Journal*, **16**:1, 1976.

[89] S. Chien, K. -L. P. Sung, R. Skalak, and S. Usami. Theoretical and experimental studies on viscoelastic properties of erythrocyte membrane. *Biophysical Journal*, **24**:463, 1978.

[90] R. M. Hochmuth, P. R. Worthy, and E. A. Evans. Red cell extensional recovery and the determination of membrane viscosity. *Biophysical Journal*, **26**:101, 1979.

[91] T. M. Fischer. On the energy dissipation in a tank-treading red blood cell. *Biophysical Journal*, **32**:863, 1980.

[92] M. Puig-de-Morales-Marinkovic, K. T. Turner, J. P. Butler, J. J. Fredberg, and S. Suresh. Viscoelasticity of the human red blood cell. *American Journal of Physiology - Cell Physiology*, **293**:C597, 2007.

[93] T. M. Fischer, C. W. M. Haest, M. Stöhr-Liesen, H. Schmid-Schönbein, and R. Skalak. The stress-free shape of the red blood cell membrane. *Biophysical Journal*, **34**:409, 1981.

[94] C. Pozrikidis. Resting shape and spontaneous membrane curvature of red blood cell. *Mathematical Medicine and Biology*, **22**:34, 2005.

[95] N. Watanabe, H. Kataoka, T. Yasuda, and S. Takatani. Dynamic deformation and recovery response of red blood cells to a cyclically reversing shear flow: Effects of frequency of cyclically reversing shear flow and shear stress level. *Biophysical Journal*, **91**:1984, 2006.

[96] H. Zhou, B. B. Gabilondo, W. Losert, and W. V. D. Water. Stretching and relaxation of vesicles. *Physical Review E*, **83**:011905, 2011.

[97] Z. Peng, R. J. Asaro, and Q. Zhu. Multiscale modeling of erythrocytes in Stokes flow. *Journal of Fluid Mechanics*, **686**:299, 2011.

Vitae

Alireza Zarif Khalili Yazdani

2000 - 2004 Bachelor of Science, *Department of Mechanical Engineering, K.N Toosi University of Technology, Tehran, Iran.*

2004 - 2007 Master of Science, *Department of Mechanical Engineering, Iran University of Science and Technology, Tehran, Iran.*

2008 - 2012 Doctor of Philosophy, *Department of Mechanical & Aerospace Engineering, Rutgers University, The State University of New Jersey, Piscataway, New Jersey 08854, USA.*

Journal Publications

1. A. Z. K. Yazdani, R. Murthy Kalluri, and P. Bagchi. Tank-treading and tumbling frequencies of capsules and red blood cells, *Physical Review E*, **83**:046305, 2011.

2. A. Z. K. Yazdani and P. Bagchi. Phase diagram and breathing dynamics of a single red blood cell and a biconcave capsule in dilute shear flow. *Physical Review E*, **84**:026314, 2011.

3. A. Yazdani and P. Bagchi. Three-dimensional numerical simulation of vesicle dynamics using a front-tracking method. *Physical Review E*, **85**:056308, 2012.

4. P. Bagchi and A. Yazdani. Analysis of membrane tank-tread of nonspherical capsules and red blood cells. Submitted to *The European Physical Journal E*.

5. A. Yazdani and P. Bagchi. Influence of membrane viscosity on capsule dynamics in shear flow. Submitted to *Journal of Fluid Mechanics*.